Photon-detecting superconducting resonators

Cover: The front shows a superconducting quarterwave resonator (coplanar waveguide geometry) with its typical meandering shape, capacitively coupled to a feedline. The back shows the same shape drawn with the time domain phase signal. This phase signal, measured while keeping the resonator continuously illuminated, reflects both the quasiparticle recombination process as well as the frequency noise, the two central themes of this thesis. Its power spectral density is shown in Fig. 5.2. The background illustrates the physics behind detection: an astronomical object (sun) shines photons, the elementary packets of light, on the superconducting condensate (sea), breaking paired electron states and creating quasiparticle excitations (clouds), the subsequent change in superconducting properties is readout by applying a microwave signal (waves). Relaxation occurs when the quasiparticles recombine, ‘raining’ back to the condensate.

Photon-detecting superconducting resonators

Proefschrift

ter verkrijging van de graad van doctor
aan de Technische Universiteit Delft,
op gezag van de Rector Magnificus prof. dr. ir. J. T. Fokkema,
voorzitter van het College voor Promoties,
in het openbaar te verdedigen op woensdag 17 juni 2009 om 10:00 uur

door

Rami BARENDS

natuurkundig ingenieur
geboren te Delft.

Dit proefschrift is goedgekeurd door de promotor:
Prof. dr. ir. T. M. Klapwijk

Copromotor:
Dr. J. R. Gao

Samenstelling van de promotiecommissie:

Rector Magnificus,	voorzitter
Prof. dr. ir. T. M. Klapwijk	Technische Universiteit Delft, promotor
Dr. J. R. Gao	Technische Universiteit Delft, copromotor
Prof. dr. ir. J. E. Mooij	Technische Universiteit Delft
Prof. dr. P. C. M. Planken	Technische Universiteit Delft
Prof. dr. S. Withington	University of Cambridge, United Kingdom
Dr. ir. J. J. A. Baselmans	SRON Netherlands Institute for Space Research
Dr. A. Neto	Nederlandse organisatie voor toegepast-natuurwetenschappelijk onderzoek (TNO)
Prof. dr. ir. L. M. K. Vandersypen	Technische Universiteit Delft, reservelid

Published by: R. Barends

Printed by: GVO printers & designers | Ponsen & Looijen, Ede, The Netherlands

An electronic version of this thesis is available at:
http://repository.tudelft.nl

Casimir PhD Series, Delft-Leiden, 2009-04

ISBN 978-90-8593-052-5

Contents

Chapter 1

An eye for the sky

1.1 Written in the stars

"It's written in the stars" is a saying frequently used in relation to foretelling. Remarkably, the same is actually even more true for the past. Not only because the photons, the elementary packets of light, have travelled an eternity to arrive; but also as detecting these photons helps us to understand the formation of stars and planets, the origins of galaxies, and the Big Bang. Since the Big Bang about 98 % of the photons released and half of the luminosity of the universe are observable in the far-infrared range [1], in a frequency ranging from 0.1-10 THz. This frequency range allows us to observe star and planetary formation which occurs deep within interstellar gas and dust clouds: while the optical light is scattered and absorbed, the absorbed energy is re-emitted in the far-infrared. The far-infrared also houses the emissions from cold objects such as planets, the light from distant galaxies with a high redshift, as well as a snapshot of the very infant universe.

This snapshot is the cosmic microwave background radiation which formed when the early universe became transparent; it is the lingering echo of the Big Bang which has faded to a background radiation temperature of only 2.7 K above absolute zero. Yet it carries the imprints of tiny fluctuations in the density of matter and energy at the time of its creation. These variations reveal a great deal about the universe; such as the accelerating inflation as well as the large scale structure, revealing the origin of galaxies and pointing towards the presence of dark matter and energy [2, 3]. Additionally, the far-infrared is brimming with many atomic and molecular spectral lines; these 'spectral fingerprints' allow for identifying these substances in interstellar gas clouds and planetary atmospheres. Moreover, the velocity can be extracted from the Doppler-shifted frequencies of the spectral lines; additionally, the width of the lines is controlled by the pressure and temperature via pressure broadening and by the internal dynamics via Doppler broadening. By resolving the spectral lines, organic molecules, the building blocks of life, have been found in the faraway dustclouds around protostars where planets form [4].

The richness of phenomena observable in the far-infrared range, see Fig. 1.1a, drives the development of sensitive detectors for large imaging arrays in space-based observatories as well as earth-based telescopes [5, 6]. Far-infrared imaging arrays measure the intensity, working in the same manner as many optical digital cameras in everyday life. This mode of operation is called direct detection, and comes in two flavours: photometry and spectrophotometry, depending on the frequency selectivity. Feeding the power over a large frequency range directly to the imaging array is referred to as photometry. Alternatively, for spectropho-

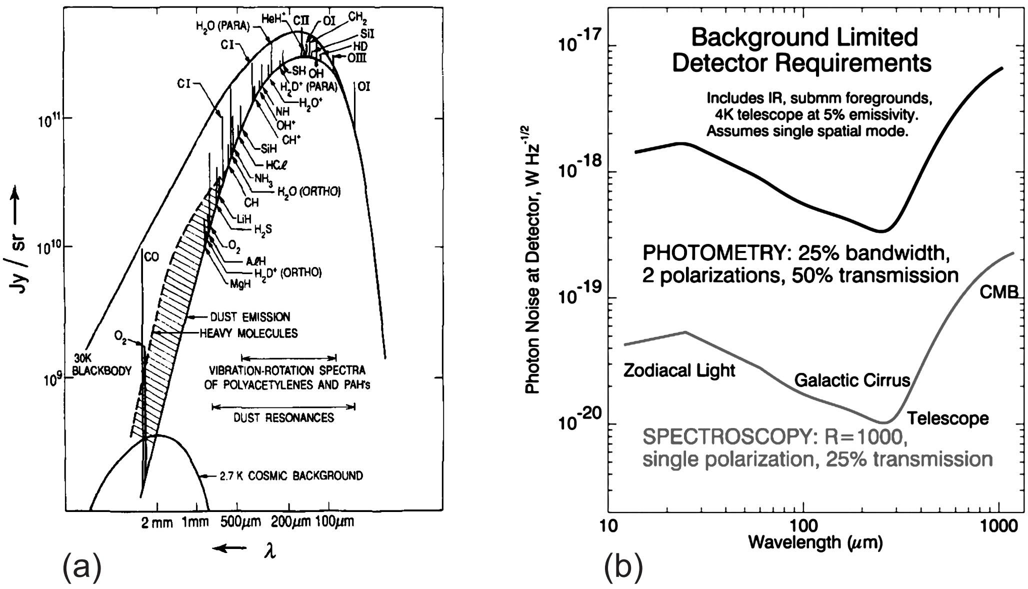

Figure 1.1: (a) The schematic representation of the spectral content in the far-infrared for an interstellar cloud, consisting of many spectral lines, dust emissions as well as the blackbody spectrum of cold objects, all superimposed on top of the cosmic microwave background radiation. Figure from Ref. [7]. (b) The detector requirements for space-based background-limited far-infrared photometry and imaging spectroscopy [8].

tometry the signal is first fed through a tunable narrow bandpass filter, such as a Michelson interferometer. Using this method a frequency resolution of several thousand can be accomplished, allowing for spectral line survey over a wide field of view and broad frequency range. These line surveys are used among others to identify molecular species as well as finding regions of interest for high resolution spectroscopy. High resolution spectroscopic observations in the THz frequency range are made using heterodyne detection. Here, the signal is mixed in a non-linear element with a locally generated tone from a local oscillator at a nearby frequency, similarly to FM radio reception. This technique allows for obtaining phase information and a frequency resolution as high as 10^6, useful for resolving the narrow width of spectral lines; yet only in a narrow frequency range. Additionally, heterodyne receivers generally are single-pixel, or have a very low number of pixels, and have to rely on large imaging arrays for finding places of interest.

Observing the universe in the far-infrared contributes to answering the open questions in cosmology, astrophysics and astrochemistry and increases our understanding of the universe: the discovery of the blackbody form and anisotropy of the cosmic microwave background radiation, based on measurements of the Cosmic Background Explorer (COBE) satellite, was awarded the Nobel prize in physics in 2006. This satellite mission was quickly followed up by the Wilkinson Microwave Anisotropy Probe (WMAP) and ESA's Planck satellite was launched this year alongside the Herschel Space Observatory. The universe is a fascinating place, encouraging us to look!

1.2 A camera for the cool cosmos

1.2.1 Challenges for far-infrared detectors

One of the greatest challenges in astronomy is the development of large imaging arrays (100x100 pixels or more) for observing the universe in the far-infrared with a detector sensitivity so high, that it is limited by the background emanations from the *universe itself*. These emanations arise from the reflection of the sun's light on dust particles in our solar system (zodiacal light), large gas clouds in our galaxy (galactic cirrus) and the cosmic microwave background radiation. To this end, the observatory needs to be placed in space to avoid the absorption by our own atmosphere, the optics need to be cooled down to a temperature of 4 K to decrease the thermal self emission, and most importantly: the input noise of the detector, expressed as a noise equivalent power (NEP), needs to be on the order of 10^{-18} W/$\sqrt{\text{Hz}}$ for imaging and 10^{-20} W/$\sqrt{\text{Hz}}$ for spectrophotometry with a grating spectrometer with a spectral resolution of 10^3 [1, 8], see Fig. 1.1b. To date, no such imaging array exists.

Although we are accustomed to the large and crisp images from the Hubble Space Telescope in the optical range, the amount of pixels for present-day space-based far-infrared imaging is really low. Space-based photon detection below 3 THz has so far been done using stressed gallium-doped germanium photoconductors. The Spitzer Space Telescope, launched in 2003, has only 40 (!) pixels for this range [9]. Moreover, the Photodetector Array Camera and Spectrometer (PACS) instrument of the Herschel Space Observatory, has only a 16x32 array for the 130-210 μm wavelength range [10].

Even more challenging is to achieve background-limited detection. Whereas for ground-based imaging a detector NEP of $10^{-17} - 10^{-16}$ W/$\sqrt{\text{Hz}}$ suffices due to the sky noise and atmospheric transmissivity [11], for space-based observatories a low detector NEP is crucially important. To put the background-limited NEP in perspective, the PACS instrument of the Herschel Space Observatory, for the 60-210 μm wavelength range, has a detector NEP on the order of 10^{-16} W/$\sqrt{\text{Hz}}$, four orders of magnitude above the background noise for spectrophotometry. To fully appreciate this difference we need the radiometer equation, which relates the standard deviation σ_T to the system input noise temperature T_N and observation time τ: $\sigma_T = T_N/\sqrt{B\tau}$, with B the frequency bandwidth [12]. Thus, to get a certain signal-to-noise ratio, τ scales with T_N^2. In other words, with background-limited detectors up to a staggering 10^8 times more observations could be made than with the PACS instrument in the same mission time! Importantly, very faint objects can be observed. Obviously, a background-limited imaging array will revolutionise astronomy.

1.2.2 Superconducting detectors

The development of sensitive far-infrared detectors which can catch these 'cold' photons has proven to be elusive. Clearly, the semiconducting technology has been stretched to its limits with respect to sensitivity and array size. Superconductors however are ideally suited for the task. The hallmark of superconductors is that the electrons are condensed in a macroscopic quantum state, formed by paired electrons - Cooper pairs. This Cooper pair condensate brings about the characteristic properties such as the zero resistance. The energy needed to break a pair is 2Δ, with Δ the binding energy, which is on the order of a meV and is smaller than the energy of a photon in the THz frequency range. Hence these photons are able to break Cooper pairs into quasiparticle excitations, subsequently modifying the superconducting properties. Different classes of photon detectors exist which use different properties. The two main methods are bolometric detection and pair-breaking detection: bolometric detectors monitor the rise of the *temperature* of a small superconducting island whereas pair-breaking detectors effectively count the *nonthermal* increase in the quasiparticle density and the related decrease in the Cooper pair density due to incoming radiation.

Transition edge sensor bolometers make use of the steep resistive transition in a narrow temperature range when the superconducting state collapses at the critical temperature [13, 14]. By optimally choosing the bath temperature and bias, a very weak incoming radiation signal can drive the superconductor further into the superconductor-to-normal transition, bringing about a large change in resistance. Essentially the transition is used as a highly sensitive thermometer; yet only in a small temperature range, putting requirements on the dynamic range in relation to the sensitivity (these requirements are less stringent when using electro-thermal feedback). The sensitivity is proportional to the thermal response time. As pixels need to be fast for readout using time domain multiplexing this limits the sensitivity of large arrays. Additionally, each sensor needs its own superconducting quantum interference detector (SQUID) for readout. Alternatively, readout can be done in the frequency domain, but this requires coupling each sensor to a resonator. This complicates large array development.

An example of a pair-breaking detector is a superconducting tunnel junction, which detects radiation by monitoring the current arising from photo-excited quasiparticles crossing a very thin insulating oxide barrier [15]. If the barrier is thin enough, quantum mechanics allows electrons to tunnel, i.e. to move through the barrier from one electrode to the other. A drawback is that Cooper pairs can also cross the barrier, this Josephson current needs to be tuned out using a magnetic field. Simultaneously suppressing the Josephson current in an array of junctions is difficult as the magnetic field needed may vary among junctions, due to variations in the barrier area or properties. This makes tunnel junctions less favorable to place in large arrays.

So far, the readout of many pixels has proven to be a formidable obstacle for the development of large arrays as individual pixels require their own amplifiers and cabling, resulting in complex readout schemes as well as the transfer of heat through the cabling. Most importantly however, the sensitivity of large arrays is at present not high enough for space-based background-limited detection.

1.2.3 Catching cold photons with superconducting resonators

A promising new approach to the detection of photons is by using superconducting resonators [16]. The steady stream of incoming photons (with photon energy larger than 2Δ) breaks up Cooper pairs into unpaired excitations, changing their respective densities, affecting the high frequency response of the superconductor.

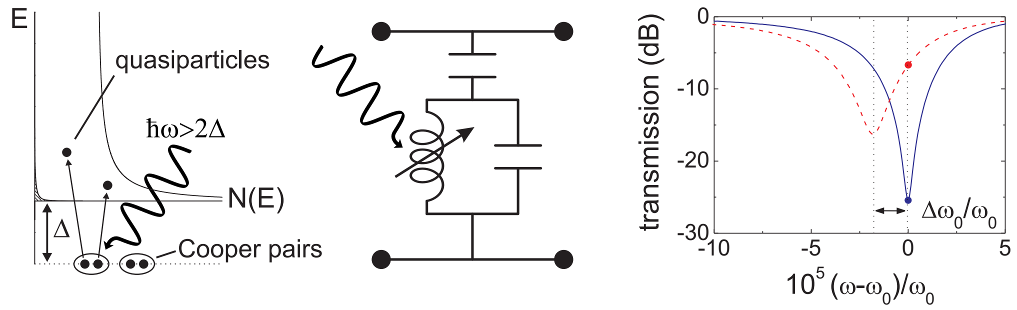

Figure 1.2: Left: A photon with energy $\hbar\omega$ is absorbed and breaks a Cooper pair, creating quasiparticle excitations on top of the thermal background. Middle: The variation in the Cooper pair and quasiparticle densities leads to a change in the kinetic inductance. Right: Subsequently the resonance frequency of the circuit shifts.

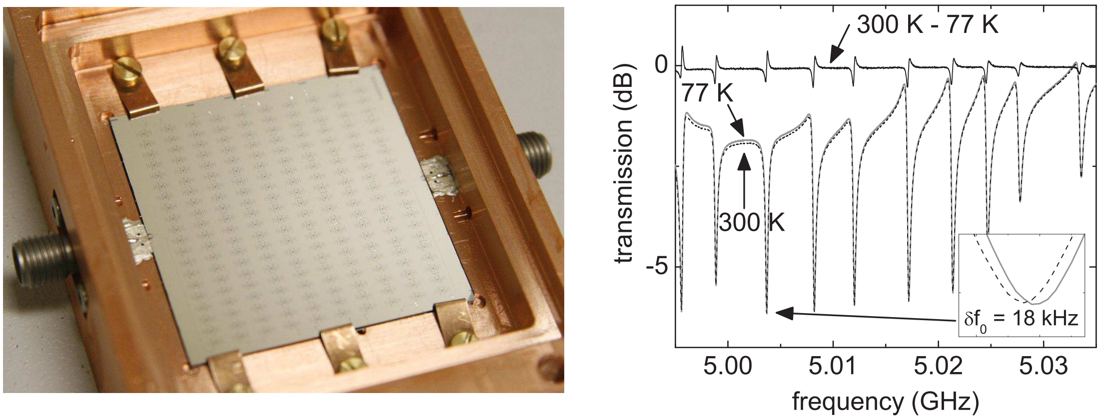

Figure 1.3: Left: A prototype 20x20 pixel far-infrared camera based on superconducting resonators. These resonators are all coupled to a single feedline which runs across the chip. The camera can be read out by connecting only a pair of coaxial cables. Right: Each of the resonators has a unique resonance frequency and can be individually addressed. When shining light from a 77 K or 300 K blackbody, the resonance frequency shifts, this response can be simultaneously read out in the frequency domain. (Provided by J. J. A. Baselmans and S. J. C. Yates, SRON Utrecht).

This response is probed by applying a microwave signal (with microwave photon energy far below 2Δ): the Cooper pairs ‘dance to the tune’, being accelerated and decelerated by the electromagnetic fields, yet with twice the mass of a single electron. This non-dissipative, accelerative response gives rise to a *kinetic inductance*, controlling the resonance frequency of the LC circuit. Therefore, the absorption of photons results in a change of the resonance frequency, see Fig. 1.2.

These resonators, or kinetic inductance detectors, are extremely sensitive: having quality factors on the order of a million, they can sense tiny photo-induced variations in the Cooper pair density. Additionally, the dynamic range is large as the sensitivity decreases only gradually in the presence of increasing signal loading. By giving each resonator a slightly different length, like the pipes in an organ, each resonator has a unique resonance frequency. Hence large amounts of resonators can be read out simultaneously in the frequency domain, see Fig. 1.3, using only a pair of cables and a single amplifier in the cryostat! A 4-8 GHz bandwidth can easily accommodate 10^4 resonators with quality factors of 10^5 or larger. Moreover, electronics already exist to read out thousands of pixels using a single board [17]. This natural ability for frequency domain multiplexing allows for constructing large and sensitive imaging arrays.

These superconducting photon detectors work best when relaxation is slow. The amount of excitations created by the stream of incoming photons, and con-

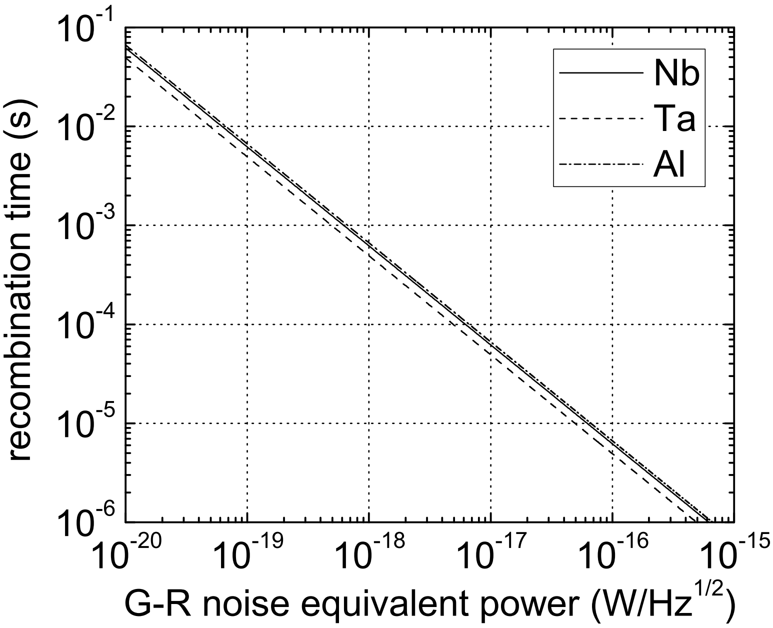

Figure 1.4: The required quasiparticle recombination time versus generation-recombination limited noise equivalent power (NEP) for a typical resonator volume and assuming unity efficiency, see Appendix A. Clearly, background-limited photometry (also see Fig. 1.1b) is possible with a recombination time around a millisecond and spectrophotometry is achievable with a recombination time in excess of tens of milliseconds.

sequently the detector sensitivity, is proportional to the relaxation time. The relaxation occurs by the pairing, or recombination, of these excitations into Cooper pairs. The recombination process is a binary reaction; the recombination time is reciprocally related to the density of quasiparticles available for recombination. As the thermal quasiparticle density decreases exponentially with decreasing temperature T as $e^{-\Delta/kT}$, the recombination time and sensitivity increase with the same temperature dependence as $e^{\Delta/kT}$. The photon detection essentially relies on counting Cooper pairs and quasiparticles, hence the noise is in principle given by the the random thermal generation of quasiparticles and the subsequent recombination: generation-recombination noise. The generation-recombination noise limited NEP is: $NEP_{G-R} = 2\Delta\sqrt{N_{qp}/\tau_r} \propto e^{-\Delta/kT}$, with N_{qp} the quasiparticle number, τ_r the recombination time and assuming unity absorption efficiency; the derivation is given in Appendix A. The recombination time needed to reach a generation-recombination noise limited NEP is plotted in Fig. 1.4, illustrating the importance of slow relaxation: background-limited detection (Fig. 1.1b) is achievable with a recombination time around a millisecond or more.

1.3 Matchmaking on a nanoscale

Interestingly, the drive for sensitive detectors for observing the *universe* boils down to understanding processes occurring at a *microscopic* scale; guided by questions like: “How do electrons interact and exchange energy?”, and equally important “What fluctuates at low temperatures, causing noise?”. These questions lie at the heart of solid state physics. At the same time, the temperatures in the superconductor are so low that less than a billionth of the conduction electrons are thermally excited and statistics of small numbers come into play. The effect of microscopic fluctuations on macroscopic parameters can no longer be considered small. Additionally, as these processes occur in superconducting films with a thickness of only several tens of nanometers, these questions connect to mesoscopic physics.

When photons are caught and their energy is dissipated, Cooper pairs are broken and quasiparticles are excited; they are distributed over the energy in such a way that they can no longer be described by a temperature: the distribution has become nonthermal and the superconductor is in a nonequilibrium state. The superconducting resonator becomes a sensitive probe to the microscopic processes of scattering and recombination, occurring at the crossroads of the energy exchange via inelastic electron-electron and electron-lattice interaction. Additionally, it is a useful tool to elucidate the physical mechanisms behind for example the influence of disorder and the possible interaction with magnetic atoms. Importantly, if the perturbation is small, the relaxation process reveals a great deal about the *equilibrium* properties.

In principle these properties are controlled by the superconductor, but possibly present dipoles and magnetic spins can couple to the electric and magnetic fields in the resonator; additionally they can influence the electron system. Indeed, configurational defects with a dipole moment, that fluctuate between low-lying energy states, have already been found in superconducting resonators through the temperature dependence of the resonance frequency [18]. These dipole systems have also been conjectured to cause noise by random fluctuation. Interestingly, superconducting resonators made of a variety of superconducting materials and dielectric substrates show significant frequency noise. The noise has been observed to *increase* with decreasing temperature [19, 20], contrary to for example noise arising from thermal fluctuations, forming a major issue for low temperature applications.

The energy exchange and noise at low temperatures are not only of fundamental importance but are of practical value in a broad context: many devices critically depend on the low temperature properties of superconducting films. A prime example is the research into quantum information processing using superconducting systems. A normal bit is either a logical 0 or 1, but a quantum bit is represented by the superposition of the two. The quantum bit can be stored in the charge on a very small superconducting island, the flux in a superconducting ring, or the phase difference between superconductors over a tunnel barrier [21]. Yet, in all these systems the evolution in time of the qubit state seems strongly disturbed by the influence of the environment. Superconducting islands seem to have more quasiparticle excitations than theoretically predicted [22, 23], an issue called ‘quasiparticle poisoning’, dipole fluctuators have been encountered in thin oxide barriers [24], and recent measurements suggest the presence of unpaired spins on the surfaces of superconductors [25]. The decoherence has proved to be a tremendous obstacle for quantum computation.

The desire for sensitive far-infrared imaging arrays stimulates the research into fundamental physical processes: the relaxation and noise at these low temperatures in superconductors are virtually untrodden territory. This forms the main theme of this thesis. As such, the recombination, the matchmaking of quasiparticles into Cooper pairs, as well as the happy marriage between astronomy and mesoscopic physics, can truly be considered as *matchmaking on a nanoscale*.

1.4 This thesis

This thesis describes a series of experiments using superconducting resonators designed to elucidate the physical mechanisms behind quasiparticle relaxation and noise, as well as to identify the fundamental limitations to using these resonators as photon detectors.

Chapter 2: In this chapter we introduce the most relevant concepts of superconductivity, relaxation and noise, forming a basis for the topics of this thesis.

Chapter 3: Here we focus on the important aspects of planar superconducting resonators, which are used throughout this thesis: we describe the geometry and fabrication, present the microwave properties for characterising these resonators and provide a practical guide for probing their properties.

Chapter 4: Here we find that the quality factors of the superconducting resonators increase with decreasing temperature, yet saturate at low temperatures, exhibiting a significant dependence on the power levels inside the resonator.

Moreover, we find a clear nonmonotonic temperature dependence in the resonance frequency of Nb and Ta resonators, signalling the presence of dipole tunnelling systems. Additionally, preliminary measurements indicate the presence of significant noise in the resonance frequency.

Chapter 5: We directly probe the low temperature recombination process for the first time and find recombination times as long as a millisecond for Al and several tens of microseconds for Ta using high quality factor superconducting resonators. Additionally, we find a remarkable saturation of the relaxation time, indicating the presence of a second recombination process dominant at low temperatures in the superconducting films. Measurements of the noise spectral density under continuous illumination confirm the relaxation process is dominated by a single timescale.

Chapter 6: Triggered by the low temperature saturation of the relaxation time and its reminiscence to experimental results with normal metals, we extend on the research in Chapter 5 and investigate the influence of magnetic impurities. We find that the low temperature recombination process is strongly enhanced by the implantation of magnetic as well as nonmagnetic atoms, pointing towards disorder, possibly at the superconductor surface.

Chapter 7: In this chapter we show that NbTiN on hydrogen passivated Si does not exhibit the peculiar nonmonotonic temperature dependence of the resonance frequency previously found in the other materials used. Moreover, we demonstrate that we can re-establish this nonmonotonic temperature dependence by covering the superconductor with a SiO_2 dielectric layer, scaling with the thickness. In contrast, the noise increases when covering the superconductor, but does *not* increase with further thickness, indicating the noise predominantly arises at the superconductor-dielectric interface and/or the interface between the dielectric layer and the substrate.

Chapter 8: We find that the noise can be significantly decreased by widening the geometry of the resonator waveguide. Additionally, the noise is lowest when using hydrogen passivated Si instead of sapphire as substrate, suggesting that the superconductor-substrate interface plays an important role as well.

Apart from the elucidating research into fundamental processes in condensed matter physics and into limitations to using superconducting resonators as photon detectors, this thesis is also a record of the joint pioneering work of the Delft University of Technology and the SRON Netherlands Institute for Space Research, which resulted in an increase of the sensitivity with *three orders of magnitude* during the course of this thesis. Noise equivalent powers as low as $6 \cdot 10^{-19}$ W/$\sqrt{\text{Hz}}$ (measured electrically) have been reached [26], which is already low enough for photometry and requires only one last order of magnitude for imaging spectrometry, limited by the universe itself, to come into focus (see Fig. 1.1b). Already large efforts are being put into the development of far-infrared imaging instruments based on these superconducting resonators; for ground based imaging such as the Caltech Submillimeter Observatory (CSO) [27], the IRAM 30m telescope, the Atacama Pathfinder Experiment (APEX) as well as for space-based telescopes such as the Spica far-infrared instrument (SAFARI) on the future Space Infrared telescope for Cosmology and Astrophysics (SPICA) satellite. These imaging arrays will be a valuable contribution to astronomy; sensing the universe alongside heterodyne receivers, such as the superconducting mixers from our group which are employed in the Heterodyne Instrument for the Far-Infrared (HIFI) of the Herschel Space Observatory [28], and the Atacama Large Millimeter Array (ALMA) [29]. As for the future discoveries in astronomy using superconducting resonators: that remains, in every meaning of the words, *written in the stars.*

References

[1] D. Leisawitz *et al.*, *Scientific motivation and technology requirements for the SPIRIT and SPECS far-infrared/submillimeter space interferometers*, Proc. SPIE **4013**, 36 (2000).

[2] P. G. Ferreira, *The cosmic microwave background*, Physics World **16**, 27 (2003).

[3] G. Hinshaw, *WMAP data put cosmic inflation to the test*, Physics World **19**, 16 (2006).

[4] A. Noriega-Crespo *et al.*, *A new look at stellar outflows: Spitzer observations of the HH 46/47 system*, Astrophys. J. Sup. Series **154**, 352 (2004).

[5] *Detector needs for long wavelength astrophysics*, a report by the Infrared, Submillimeter, and Millimeter Detector Working Group, NASA, June 2002.

[6] *Community plan for far-infrared/submillimeter space astronomy*, Februari 2003.

[7] T. G. Phillips and J. Keene, *Submillimeter astronomy*, Proc. IEEE. **80**, 1662 (1992).

[8] D. J. Benford, S. Harvey Moseley, *Cryogenic detectors for infrared astronomy: the Single Aperture Far-InfraRed (SAFIR) Observatory*, Nucl. Instr. Meth. Res. A **520**, 379 (2004).

[9] P. L. Richards and C. R. McCreight, *Infrared detectors for astrophysics*, Physics Today **58**, 41 (2005).

[10] *PACS Observer's Manual*, May 2007.

[11] W. Holland *et al.*, *SCUBA-2: a 10,000 pixel submillimeter camera for the James Clerk Maxwell Telescope*, Proc. SPIE **6275**, 62751E (2006).

[12] R. H. Dicke, *The measurement of thermal radiation at microwave frequencies*, Rev. Sci. Instr. **17**, 268 (1946).

[13] K. D. Irwin and G. C. Hilton, *Transition-Edge Sensors* in *Cryogenic Particle Detection*, edited by C. Enss (Springer-Verlag, Berlin-Heidelberg, 2005)

[14] D. J. Benford and S. Harvey Moseley, *Astronomy Applications of Superconducting Transition Edge Sensor Bolometer Arrays*, Proc. Space Detectors Workshop, 2000.

[15] A. Peacock, P. Verhoeve, N. Rando, A. van Dordrecht, B. G. Taylor, C. Erd, M. A. C. Perryman, R. Venn, J. Howlett, D. J. Goldie, J. Lumley, and M. Wallis, *Single optical photon detection with a superconducting tunnel junction*, Nature **381**, 135 (1996).

[16] P. K. Day, H. G. LeDuc, B. A. Mazin, A. Vayonakis, and J. Zmuidzinas, *A broadband superconducting detector suitable for use in large arrays*, Nature **425**, 817 (2003).

[17] S. J. C. Yates, A. M. Baryshev, J. J. A. Baselmans, B. Klein, R. Güsten, *FFTS readout for large arrays of Microwave Kinetic Inductance Detectors*, arXiv:0903.2431.

[18] J. Gao, M. Daal, A. Vayonakis, S. Kumar, J. Zmuidzinas, B. Sadoulet, B. A. Mazin, P. K. Day, and H. G. LeDuc, *Experimental evidence for a surface distribution of two-level systems in superconducting lithographed microwave resonators*, Appl. Phys. Lett. **92**, 152505 (2008).

[19] R. Barends, H. L. Hortensius, T. Zijlstra, J. J. A. Baselmans, S. J. C. Yates, J. R. Gao, and T. M. Klapwijk, *Contribution of dielectrics to frequency and noise of NbTiN superconducting resonators*, Appl. Phys. Lett. **92**, 223502 (2008).

[20] S. Kumar, J. Gao, J. Zmuidzinas, B. A. Mazin, H. G. LeDuc, and P. K. Day, *Temperature dependence of the frequency and noise of superconducting coplanar waveguide resonators*, Appl. Phys. Lett. **92**, 123503 (2008).

[21] M. H. Devoret, A. Wallraff, and J. M. Martinis, *Superconducting Qubits: A Short Review*, arXiv:cond-mat/0411174.

[22] J. Aumentado, M. W. Keller, J. M. Martinis, and M. H. Devoret, *Nonequilibrium Quasiparticles and 2e Periodicity in Single-Cooper-Pair Transistors*, Phys. Rev. Lett. **92**, 066802 (2004).

[23] J. M. Martinis, M. Ansmann and J. Aumentado, *Energy Decay in Josephson Qubits from Non-equilibrium Quasiparticles*, arXiv:0904.2171.

[24] J. M. Martinis, K. B. Cooper, R. McDermott, M. Steffen, M. Ansmann, K. D. Osborn, K. Cicak, S. Oh, D. P. Pappas, R. W. Simmonds, and C. C. Yu, *Decoherence in Josephson Qubits from Dielectric Loss*, Phys. Rev. Lett. **95**, 210503 (2005).

[25] S. Sendelbach, D. Hover, A. Kittel, M. Mück, J. M. Martinis, and R. McDermott, *Magnetism in SQUIDs at millikelvin temperatures*, Phys. Rev. Lett. **100**, 227006 (2008).

[26] J. J. A. Baselmans, S. J. C. Yates, R. Barends, Y. J. Y. Lankwarden, J. R. Gao, H. F. C. Hoevers, and T. M. Klapwijk, *Noise and sensitivity of aluminum kinetic inductance detectors for sub-mm astronomy*, J. Low Temp. Phys. **151**, 524 (2008); and unpublished results.

[27] J. Schlaerth, A. Vayonakis, P. Day, J. Glenn, J. Gao, S. Golwala, S. Kumar, H. LeDuc, B. Mazin, J. Vaillancourt, and J. Zmuidzinas, *A Millimeter and Submillimeter Kinetic Inductance Detector Camera*, J. Low Temp. Phys. **151**, 684 (2008).

[28] B. D. Jackson, G. de Lange, T. Zijlstra, M. Kroug, J. W. Kooi, J. A. Stern, and T. M. Klapwijk, *Low-Noise 0.8-0.96 and 0.96-1.12 THz Superconductor-Insulator-Superconductor Mixers for the Herschel Space Observatory*, IEEE Trans. Micr. Theory and Tech. **54**, 547 (2006).

[29] C. Kasemann, R. Güsten, S. Heyminck, B. Klein, T. Klein, S. D. Philipp, A. Korn, G. Schneider, A. Henseler, A. Baryshev, and T. M. Klapwijk, *CHAMP$^+$: a powerful array receiver for APEX*, Proc. SPIE **6275**, 62750N (2006).

Chapter 2

Relaxation, low frequency fluctuation and the response to high frequency radiation

2.1 Cooper pairs and quasiparticle excitations

In metallic solids, many of their properties are controlled by only the few electrons in the outermost shells of the ions. These electrons are so weakly bound that they become delocalised and act as mobile charge carriers, bringing about the characteristic conductivity of metals. At a first glance, metals are adequately described by treating these conduction electrons as a gas of fermions consisting of free, noninteracting electrons, constrained only by the Pauli exclusion principle; the Sommerfeld theory of metals [1].

In many metals the electron density is huge, being on the order of 10^{23} $1/\text{cm}^3$, and the mutual interaction needs to be considered. In a real gas, with increasing density and decreasing kinetic energy (by decreasing the temperature) the interactions become so dominant that the gas changes into a liquid. Analogously, with strong interactions the picture of charge carriers in metallic solids as a free electron Fermi gas needs to be reanalysed. Electrons interact by pushing each other away due to their charge, i.e. Coulomb repulsion. At the same time this repulsion is reduced by the screening of the electron charge by other electrons to relatively short distances on the order of the interatomic spacing; effectively, an electron is surrounded by its nearby screening cloud. When a particle is in motion, it moves together with the surrounding distortion brought about by the screened Coulomb interaction, perturbing the other electrons in the vicinity. As such, these charge carriers can no longer be treated purely as a collection of single electrons in a Fermi gas, but have to be thought of as electron-like particles in a Fermi liquid, so-called *quasiparticles* [2].

The consequences are far-reaching. As a quasiparticle is in essence a many-body process, quasiparticles are interdependent. Additionally, quasiparticle states are no longer stationary and have a finite lifetime. The quasiparticles adopt the role of charge carriers, affecting the electronic properties of the metal, from conductivity to the dielectric response. In normal metals these are referred to as Landau quasiparticles. Most of the changes are subtle, and the Sommerfeld free electron model is still a good starting point for many applications when using an effective density of states or particle mass, and we can loosely refer to Landau quasiparticles as ‘electrons’. Foremost, the *interdependence* of quasiparticles constitutes a fundamental shift in the approach to elastic and inelastic interactions: the non-equilibrium processes and fluctuations in metallic systems.

In metallic solids with a strong electron-lattice coupling, in addition to the Coulomb repulsion an *attractive* interaction can exist: in their motion, conduction electrons distort the lattice by attracting the positively charged ions. Due to the delayed response of the lattice a positively charged region is left in the wake

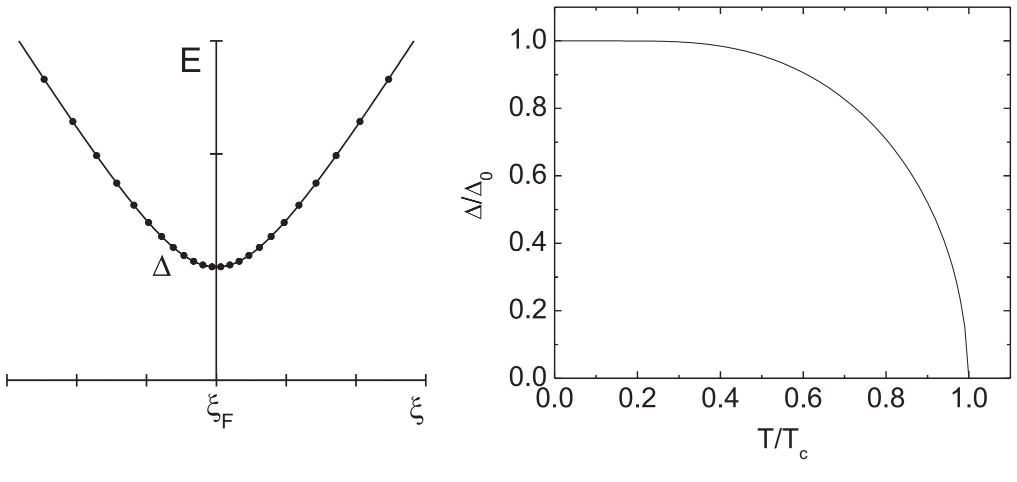

Figure 2.1: Left: The Bogoliubov quasiparticle excitation energy E versus Landau quasiparticle energy ξ relative to the Fermi level. Right: The temperature dependence of the binding energy in the superconducting state (Eq. 2.1).

of the electron path, attracting another electron which effectively forms a pair with the first one. Cooper showed in 1956 that in the presence of an attractive interaction two electrons form a bound state with binding energy Δ [3]. This notion was a crucial stepping stone to the well-known standard microscopic theory of superconductivity by Bardeen, Cooper and Schrieffer, formulated in 1957 [4]. At zero temperature the electrons condense into a macroscopic quantum state, which is formed by Cooper pairs at the Fermi energy, pairs of electrons with opposite wavevector and spin, or alternatively, pairs of time-reversed electron states. The upper limit of coherence between the individual electrons in the Cooper pair condensate, and thus the maximum spatial extent of the pair is set by the coherence length, for clean materials: $\xi_0 = \hbar v_F/\pi\Delta_0$, with v_F the Fermi velocity and Δ_0 the binding energy at zero temperature. The elementary excitations of the superconducting state are the Bogoliubov quasiparticles [5]. These quasiparticles consist of a superposition of an electron and a hole and therefore have no integer charge. They can be treated as single particles, similarly to the Landau quasiparticle concept in normal metals. The Bogoliubov quasiparticle excitation spectrum has a gap equal to the binding energy Δ. The quasiparticle excitation energy E is given by: $E^2 = \xi^2 + \Delta^2$, with ξ the energy of the single particle in the normal state (i.e. the Landau quasiparticle) relative to the Fermi energy, see Fig. 2.1. Bogoliubov quasiparticles are electron-like for $\xi > 0$ and hole-like for $\xi < 0$. In general, both are favoured equally (an exception is charge imbalance [6]). The normalised quasiparticle density of states is $N(E) = \mathrm{Re}(\frac{E}{\sqrt{E^2-\Delta^2}})$, showing a singularity at $E = \Delta$. The value of Δ is controlled by the distribution of these quasiparticles over the energy $f(E)$, [4]

$$\frac{1}{N^a(0)V_{eff}} = \int_{\Delta}^{\hbar\omega_D} \frac{1-2f(E)}{\sqrt{E^2-\Delta^2}} dE \tag{2.1}$$

with $N^a(0)$ the absolute single spin electron density of states at the Fermi level, V_{eff} the effective attractive potential and the electron-phonon interaction cut-off at the Debye energy $\hbar\omega_D$. The value of $N^a(0)V_{eff}$ is controlled by the electron-phonon coupling λ and the screened Coulomb repulsion μ^*, for weak-coupling superconductors: $N^a(0)V_{eff} = \lambda - \mu^*$ [7]. The temperature dependence of the pairing potential is shown in Fig. 2.1. The superconducting state is destroyed at a critical temperature T_c: $kT_c = 1.14\hbar\omega_D e^{-1/N^a(0)V_{eff}}$, for weak-coupling superconductors [4]. Above this temperature superconductivity appears only in fluctuations [6]. The thermal density of quasiparticle excitations is given by

$$n_{qp} = 2N^a(0)\int_{\Delta}^{\infty} N(E)f(E)dE \simeq 2N^a(0)\sqrt{2\pi kT\Delta}e^{-\Delta/kT} \tag{2.2}$$

the last part is valid for $kT \ll \Delta$ and is obtained by approximating the Fermi-Dirac distribution by a Maxwell-Boltzmann one.

The BCS theory captures the qualitative picture and allows for a quantitative description of the superconducting state. It is a microscopic explanation for the striking properties such as the complete disappearance of electrical resistivity, the active expulsion of magnetic fields, the exponentially decreasing heat capacity with decreasing temperature and strong frequency dependent far-infrared absorptivity [5, 6]. These properties challenged physicists for nearly half a century since its discovery by Kamerlingh Onnes in 1911 [8]. Remarkably, while essentially the Sommerfeld free electron model with an effective attractive potential, ignoring the energy bands and capturing the screened Coulomb repulsion only with the quantity μ^*, the superconducting state can be described by a single wavevector- and energy-independent pairing potential Δ and a macroscopic phase for nearly all s-wave superconductors, crystalline or disordered. In disordered superconductors the large amount of elastic scattering does not affect time-reversal symmetry, keeping properties of s-wave superconductors unchanged [9], yet randomizes the wave vector, allowing for dirty superconductors to be described in terms of only the *energy*.

2.2 Inelastic interaction at millikelvin temperatures

In thermal equilibrium the distribution of the quasiparticles over the energy is given by the Fermi-Dirac distribution function at an electron temperature T,

$$f_{FD}(E) = \frac{1}{1 + e^{E/kT}} \tag{2.3}$$

with E the energy relative to the Fermi level. When the electronic system is perturbed, by the absorption of energy or injection of quasiparticles, the system is driven out of the equilibrium state. The system can be described by an elevated electron temperature when instantaneous energy exchange is assumed between the quasiparticles, such as in the hot filament of a light bulb. However, at low temperatures the strength of the interactions weaken, most clearly due to the decrease of k space available for scattering near the Fermi level; additionally the phonon density decreases, in turn decreasing the energy exchange between the electron system and the lattice. Then, the quasiparticle energy distribution is no longer thermal and a nonequilibrium state results, controlled by the competition between the driving force and the inelastic interactions.

We start by discussing the energy exchange at low temperatures in normal metals and focus on the recent experiments. These experiments not only neatly clarify the shape and degree of nonequilibrium which can occur in for example metallic wires, but also illustrate that inelastic scattering at mK temperatures is unexplored territory, elucidating very recently the important role of dilute concentrations of magnetic impurities. These experiments provide a framework for investigating the equilibration processes in superconductors. Subsequently, we review the inelastic interaction processes that take place in superconducting films; here, the electron-phonon processes play an important role in quasiparticle scattering and quasiparticle recombination, the latter plays a dominant role in the low temperature equilibration. Finally, we discuss the influence of magnetic impurities on the superconducting state.

2.2.1 Scattering in the normal state

Inelastic scattering in normal metals has been investigated by nonequilibrium experiments as well as experiments on quasiparticle dephasing, probed via weak localisation. As elastic scattering does not randomise the quasiparticle phase, dephasing is a measure for the inelastic scattering time. It has become clear that at high temperature the inelastic scattering is mainly due to electron-phonon

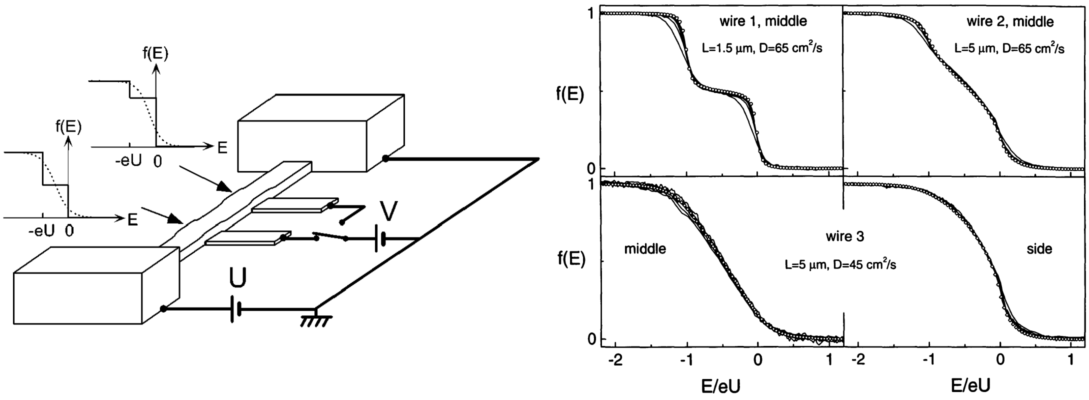

Figure 2.2: Left: A mesoscopic wire placed in between electrodes, two probing fingers are attached to the wire. Right: The distribution function inside the wire resembles a two-step function for weak inelastic scattering and is thermal in the limit of strong scattering. The distribution function becomes more thermal-like for increasing wire lengths, illustrating the competition between diffusion and inelastic scattering.

interaction whereas at low temperatures electron-electron scattering dominates, for a review see Ref. [10]. Both the temperature dependence as well as the prefactor of the scattering rate is controlled by the disorder and dimensionality of the film, the crossover between these two regimes lies roughly on the order of 1 K, for example for Al [11]. Only in specifically designed systems electron-photon processes play a significant role [12]. In practice, the emphasis for low temperature scattering lies on the interactions among quasiparticles.

In 1997 Pothier *et al.* [13] devised a way to probe the inelastic interactions by creating a nonequilibrium distribution in a voltage-biased mesoscopic wire, see Fig. 2.2. The local distribution is probed with normal metal-insulator-superconductor junctions on top of the wire. In the absence of inelastic interactions, the distribution in the wire is given by a two-step distribution function, resulting from the Boltzmann transport equation

$$f(x,E) = (1-x)f_{FD}(E+eV/2) + xf_{FD}(E-eV/2) \tag{2.4}$$

with x the coordinate along the wire and f_{FD} the Fermi-Dirac distribution function at the bath temperature. With strong inelastic scattering this distribution is rounded to a thermal one with a local, elevated temperature. Moreover, at higher voltages quasiparticles with higher energies start to play a role, allowing for probing interaction at higher energies. The actual distribution function is therefore a result of the competition between diffusion and energy-dependent inelastic scattering.

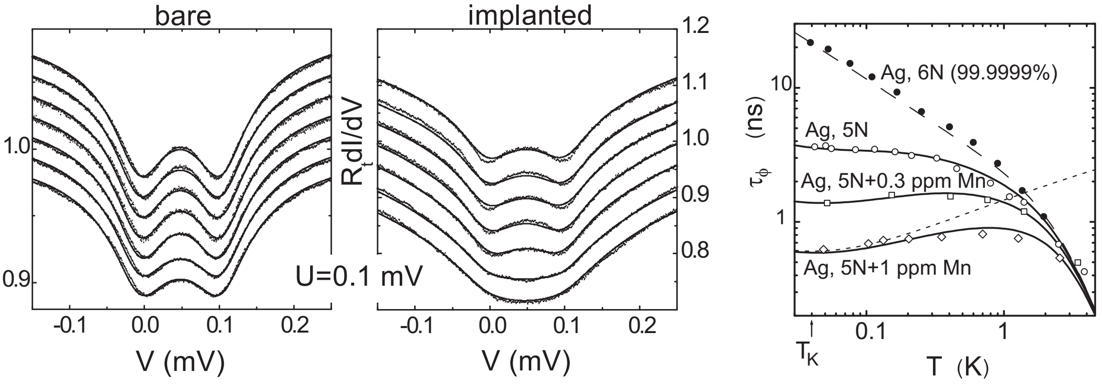

Figure 2.3: Left: The differential conductance, measured in a similar device as shown in Fig. 2.2, shows a single dip for a thermal distribution and two distinct dips for a two-step distribution. The presence of magnetic impurities leads to a stronger thermal rounding, i.e. stronger inelastic scattering. The recovery of a single dip for increasing magnetic field (from bottom to top: B=0.3 to 2.1 T with steps of 0.3 T) is an additional indication for the influence of magnetic impurities. Right: The low temperature quasiparticle dephasing time in high purity Ag is strongly reduced by the presence of only a dilute concentration of magnetic impurities.

The experiment was performed at temperatures of 25 mK in Cu wires. Whereas a two-step distribution was established in the wire for small bias voltages, for increasing voltages the distribution function was found to be more smeared, see Fig. 2.2. From these results the strength as well as the energy dependence of the inelastic electron-electron scattering was extracted; represented by the interaction kernel $K(\epsilon)$, with ϵ the exchanged energy (see Ref. [13] for details). This kernel was expected to follow $K(\epsilon) \propto 1/\epsilon^{3/2}$, reflecting screened Coulomb interaction in a quasi one-dimensional wire [14, 15]. Yet, the experimental results indicated $K(\epsilon) \propto 1/\epsilon^{2\pm0.1}$. Additionally, the strength of the interaction was stronger than predicted. These results signalled the presence of another inelastic scattering process dominating at these low temperatures.

In later experiments [16] a magnetic field dependence of the interaction in mesoscopic wires was found as well as a similar energy dependence previously obtained by Pothier *et al.*, suggesting the influence of magnetic impurities. The Kondo effect (see Chapter 2.2.3) is diminished as spin-flip scattering becomes an inelastic process due to the Zeeman splitting. At the same time, low temperature quasiparticle phase coherence times were significantly decreased by implanting magnetic impurities [17, 18], see Fig. 2.3. Recently, Huard *et al.* [19] have shown that the inelastic scattering among quasiparticles is strongly strengthened by implanting dilute concentrations (as low as 1 ppm) of magnetic impurities in similar mesoscopic Ag wires, in agreement with two-particle collisions in the presence of Kondo impurities [20] (Fig. 2.3). Further experiments show that the implantation procedure does not introduce extra dephasing in Ag [21]. This set of experiments shows that at low temperatures timescales for quasiparticles are limited by dilute concentrations of magnetic impurities, most notably the inelastic scattering between quasiparticles.

2.2.2 Quasiparticle recombination in superconducting films

A binary reaction

In superconductors, inelastic interaction becomes apparent when driving the superconductor into a nonequilibrium state. Experimentally, the nonequilibrium state can be established by injecting electrons or by creating quasiparticle excitations by inserting energy in the electron system through, for example, optical excitation. The absorption of optical photons excites quasiparticles to high energies, in turn starting a fast quasiparticle downconversion cascade. This cascade results in a large number of quasiparticles just above the superconducting gap within timescales ranging between 100 ps to 10 ns [22, 23]. Subsequent equilibration of the superconducting state takes place by the redistribution of the quasiparticles over the energy, which is accomplished by the energy exchange among quasiparticles and between quasiparticles and the lattice, as well as by recombination. Recombination is a binary process, quasiparticles with opposite wavevector and spin combine to form Cooper pairs, the energy is transferred to another excitation. It is the most important process as it allows both for large energy exchanges as well as for the recovery of the quasiparticle and Cooper pair density to their equilibrium values. It also is the slowest and therefore limiting process for equilibration. We therefore limit the discussion to recombination.

Historically, recombination has been investigated at temperatures close to the critical temperature (see for example the first experiments by Miller *et al.* [24]). Here it was found that electron-phonon processes dominate for two reasons: One, recombination with phonon emission is orders of magnitude faster than recombination with photon emission [25]. Two, recombination with phonon emission is a *binary* reaction, following $\tau_r \propto e^{\Delta/kT}$ due to the availability of quasiparticles [26]. This while recombination with electron-electron interaction only is a *trenary* reaction (two quasiparticles recombine and transfer their energy to a third), following $\tau_r \propto e^{2\Delta/kT}$ [27]. Obviously with decreasing temperature a binary reaction is much more probable than a trenary reaction. Moreover the energy gap develops, allowing large energy exchanges only through electron-phonon scatter-

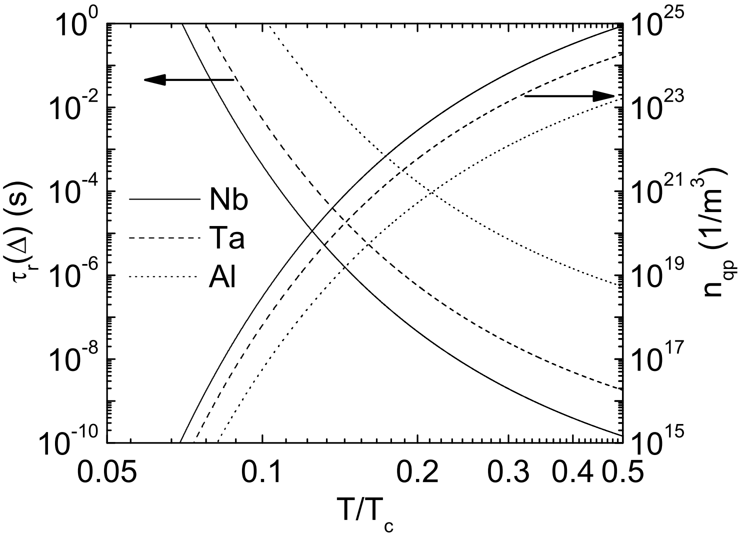

Figure 2.4: The temperature dependence of the recombination time for a quasiparticle at the gap energy and the quasiparticle density for Nb (τ_0=0.15 ns), Ta (τ_0=1.8 ns) and Al (τ_0=440 ns) [29].

ing. The inelastic electron-electron interactions are relevant only at temperatures very close to T_c. For Al, a weak-coupling superconductor, just above the critical temperature the inelastic electron-electron scattering dominates over electron-phonon scattering [11] (see also Fig. 2.5b). Moreover, in superconducting Al Klapwijk *et al.* [28] have found the inelastic electron-electron scattering rate to exceed the electron-phonon scattering rate for $T_c - T \ll T_c$.

Recombination with phonon emission occurs at the crossroads of electron-electron and electron-phonon interaction as it involves a pair of interacting quasiparticles and the transfer of energy to the lattice. The recombination time $\tau_r(\epsilon)$ for a quasiparticle at energy ϵ is controlled by the density of states and energy gap, the electron-phonon coupling, case II coherence factors [6] and the distribution of the quasiparticles over the energy. For the BCS case Kaplan *et al.* arrived at [29],

$$\frac{\tau_0}{\tau_r(\epsilon)} = \frac{1}{(kT_c)^3[1-f(\epsilon)]} \int_\Delta^\infty (E+\epsilon)^2 \mathrm{Re}\left(\frac{E}{\sqrt{E^2-\Delta^2}}\right) \times \left(1+\frac{\Delta^2}{\epsilon E}\right)[n(E+\epsilon)+1]f(E)dE \quad (2.5)$$

with τ_0 quantifying the material-specific electron-phonon interaction at energies near the gap and $n(E)$ the phonon distribution function. The value of τ_0 is related to the electron-phonon spectral function $\alpha^2F(E)$, in the above expression we follow the assumption by Kaplan *et al.* [29] that the electron-phonon interaction α^2 is only weakly dependent on the low energies concerned. Additionally, for a three dimensional system for the Debye phonon density of states: $F(E) \propto E^2$, hence for the electron-phonon spectral function: $\alpha^2F(E) \propto E^2$.

Assuming a thermal distribution of quasiparticles and phonons, for low temperatures the recombination time can be approximated by

$$\frac{\tau_0}{\tau_r(\Delta)} = \sqrt{\pi}\left(\frac{2\Delta}{kT_c}\right)^{5/2}\sqrt{\frac{T}{T_c}}e^{-\Delta/kT} = \frac{(2\Delta)^2}{(kT_c)^3}\frac{n_{qp}}{2N^a(0)} \tag{2.6}$$

using Eq. 2.2, with $N^a(0)$ the absolute single spin density of states at the Fermi level. Eq. 2.6 shows the process in its most simple form: the recombination time is controlled by the quasiparticle density and the electron-phonon interaction. The recombination time is shown for various materials in Fig. 2.4. It increases exponentially with decreasing temperature, reciprocal to the thermal quasiparticle density. The temperature dependence is due to the *Fermi-Dirac distribution*, the prefactor is set by the value of the *electron-phonon coupling* τ_0.

The possible reabsorption by the condensate of 2Δ-phonons, emitted during recombination, leads to an increase of the relaxation time. This phonon trapping is controlled by the phonon escape time τ_{esc} [37], which depends on the acoustical film-substrate matching, and the phonon pair breaking time τ_{pb} [29]. For $\tau_{esc} \ll \tau_{pb}$ the phonons quickly leave the superconducting film and their distribution is close to equilibrium. For $\tau_{esc} \gg \tau_{pb}$ energy is being put back in the electron system by reabsorption. Consequently, the relaxation time increases, given by: $\tau = \tau_r(1 + \tau_{esc}/\tau_{pb})$, for $\tau_r \gg \tau_{esc}, \tau_{pb}$, which is the case at the low temperatures we use [38]. The values of τ_{esc} and τ_{pb} are hardly temperature dependent [29], hence the exponential increase of the relaxation time with decreasing temperature remains unchanged, but the prefactor is affected. To quantify, using $\tau_{esc} = 4d/\eta u$, with d the film thickness, η the acoustic film-substrate transparency and u the phonon velocity [39] and using values for τ_{pb} from Ref. [29], for Al: $(1+\tau_{esc}/\tau_{pb}) \sim 1$ and for Ta: $(1 + \tau_{esc}/\tau_{pb}) \sim 10$.

The role of disorder

The inelastic electron-phonon processes are sensitive to disorder. This disorder dependence has been investigated in normal metals using hot electron experiments and by measurements of the phase coherence time. The temperature

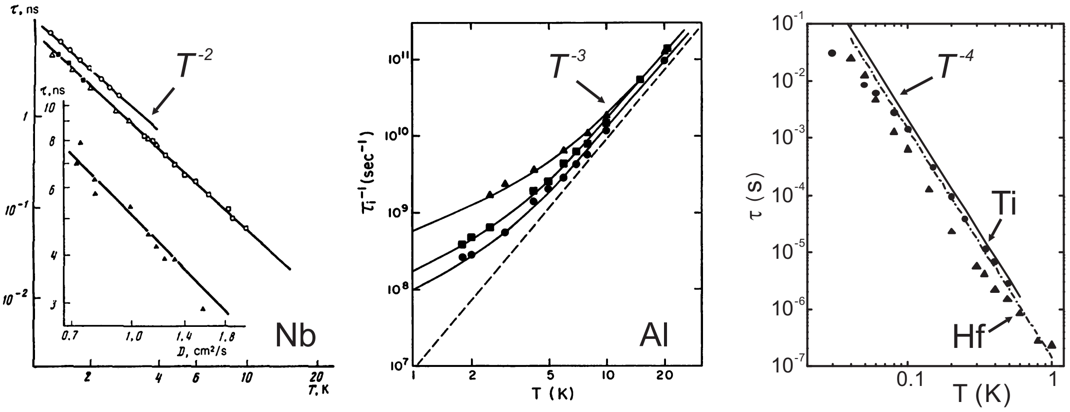

(a) (b) (c)

Figure 2.5: Three different temperature dependences of the inelastic electron-phonon scattering time in superconducting films just above the critical temperature. (a) A quadratic temperature dependence ($\tau_{ep} \propto 1/T^2$) has been found for Nb films using hot electron experiments [34]. The inset shows the dependence on the electron mean free path through the diffusion constant. (b) The phase coherence time for Al films shows at high temperatures a cubic temperature dependence, $\tau \propto 1/T^3$, consistent with inelastic electron-phonon scattering. At low temperatures electron-electron scattering dominates (following $\tau \propto 1/T$) [11]. (c) For Hf and Ti $\tau_{ep} \propto 1/T^4$ has been found using hot electron experiments [35].

dependent inelastic electron-phonon scattering time is given by [30]

$$\frac{1}{\tau_{ep}} = \frac{4\pi}{\hbar} \int_0^\infty \frac{\alpha^2 F(E)}{\sinh(E/kT)} dE \tag{2.7}$$

Obviously, if $\alpha^2 F(E) \propto E^n$, then $\tau_{ep} \propto 1/T^{n+1}$. In clean three-dimensional systems where the electron mean free path is long, scattering is mainly by longitudinal phonons, leading to a cubic temperature dependence, $\tau_{ep} \propto 1/T^3$ [31]. In an acoustically dirty film where quasiparticles experience numerous elastic scattering events within the wavelength of a phonon the interaction can be drastically changed [32, 33]. Depending on the nature of the impurity, whether they 'follow the lattice motion' or are 'pinned', the scattering can be both weakened as well as enhanced, respectively. In normal metals this leads to a strong variation in the temperature dependence of the electron-phonon scattering times as well; additionally, the *inelastic* scattering time can depend on the *elastic* scattering length; see Fig. 2.5. The recombination process depends mainly on the value of $\alpha^2 F(2\Delta)$; hence disorder changes the value of τ_0, but the exponential temperature dependence remains as it is due to the Fermi-Dirac distribution of the quasiparticles.

Superconducting tunnel junctions

Relaxation times have been extensively studied in photon detectors based on superconducting tunnel junctions [40]. Like the superconducting resonators described in this thesis, these junctions are pair-breaking detectors. The readout is however different: the detection is based on the current arising from photo-excited quasiparticles tunnelling through a very thin insulating oxide barrier. This current is very small, and is sensed with a charge integrator. Additionally the Josephson current (the tunnelling of Cooper pairs) needs to be tuned out using a magnetic field, complicating large arrays as the magnetic field needed may vary among junctions. Unlike the superconducting resonators, these tunnel junctions are sensitive only to quasiparticles *near* the barrier. The responsivity can be increased by using a material next to the tunnel barrier which has a lower energy gap than the absorber: consequently, the density of quasiparticles near the tunnel barrier increases as the quasiparticles become locally trapped.

Experiments with tunnel junctions indicate excess quasiparticle losses [41, 42, 43]. Responsivity measurements also indicate a nonmonotonic temperature dependence of these losses [44]. These losses are attributed to the ‘trapping’ of quasiparticles: quasiparticles become localised in regions with a locally reduced energy gap, containing a number of confined states (like the intentional localisation in lower gap materials near the barrier). The main idea is that the ‘trapping’ of quasiparticles leads to signal loss, as the quasiparticles cannot tunnel. The physical origin of these traps are unknown; they have been attributed to vortices, magnetic impurities, gap variations due to the lattice and oxides. Therefore, these traps have been modelled using phenomenological parameters.

Superconducting tunnel junctions have important drawbacks for elucidating physical processes and applications: First, no distinction can be made between quasiparticle trapping or recombination processes. Second, the probing of relaxation is indirect via the integrated charge. Third, practically, apart from the magnetic field needed and per-pixel charge integrators, the sensitivity is simply too low.

We show in Chapters 5 and 6 the first direct measurements of the quasiparticle relaxation time at low temperatures in superconducting films, clearly showing a saturation for Ta and Al as well as a peculiar nonmonotonic temperature dependence. As we probe the imaginary part of the complex conductivity which is associated with the Cooper pair condensate, these results show the presence of a recombination channel dominant at low temperatures in the superconducting films.

Note added in proof: Very recently Martinis *et al.* [45] conjectured that energy decay rates in Josephson qubits might be influenced by the existence of a significant quasiparticle density, about 10 per μm^2, arising from an unknown source. Such a density has been measured in Ref. [46]. Martinis *et al.* calculate the qubit energy relaxation rate using the theory by Kaplan *et al.* [29] in the presence of this nonequilibrium quasiparticle density. Interestingly, the authors find a temperature dependence - a rapid decrease in relaxation rate, reaching a minimum followed by plateau with decreasing temperature - which is strikingly similar to the recombination rate reported in Chapters 5 and 6.

2.2.3 Magnetic impurities in superconductors

In normal metals, the localised spins of magnetic impurities give rise to spin-flip scattering of conduction electrons, thereby breaking time-reversal symmetry. In the Anderson model the magnetic impurity gives rise to a localised impurity state at energy ϵ_0 below the Fermi level, in which the electron remains fixed in spin up or down position [47]. Spin flip scattering of conduction electrons then occurs as the electron is allowed by the uncertainty principle to very briefly, $\tau \sim \hbar/\epsilon_0$, exist at the Fermi level. The impurity state is then filled by another electron from the Fermi level with opposite spin. The end result is an elastic process where the spin of a conduction electron near the Fermi level is flipped [48]. Many of these processes result in the Kondo effect [48, 49]: *the localised impurity spin is screened by conduction electrons.* The Kondo effect is a many-body process: the spin-flip scattering of conduction electrons in its vicinity brings about a cloud of correlated electrons, which collectively screen the impurity. Above the Kondo temperature T_K, quantifying the magnetic nature of the impurity, the screening is only partial, and leads to an increase in the scattering and broadening of the density of states at the Fermi level. The scattering becomes stronger, hence the resistivity increases, with decreasing temperature, reaching a maximum at $T = T_K$. Well below the Kondo temperature the screening becomes total as the conduction electrons align: the screening conduction electrons and the impurity spin form a many-body singlet state, having no net spin. Consequently, the magnetic impurity and screening electrons are reduced to an elastic scatterer: the magnetic impurity has become ‘nonmagnetic’.

The strength of the interaction between impurity spin and conduction electrons depends on the impurity as well as the host. Kondo temperatures are shown in Table 2.1. Mn has the lowest Kondo temperature in a variety of materials and can be considered to be the ‘most magnetic’ of the $3d$ transition metals.

In superconductors the time reversal symmetry breaking due to spin-flip scat-

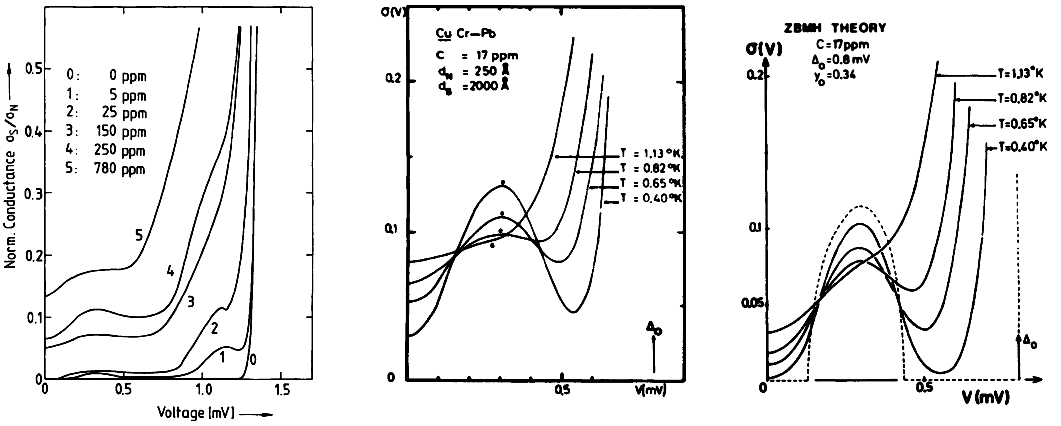

(a) (b) (c)

Figure 2.6: (a) The normalised differential conductance versus bias voltage for varying concentrations of Mn in Pb, showing the development of subgap states. Figure from Ref. [54]. (b) The differential conductance for various temperatures of a Cu layer with Cr atoms, proximitised by a Pb layer; at low temperatures the subgap states inside the gap can be clearly resolved. (c) These states are well described by the Zittartz, Bringer and Müller-Hartmann (ZBMH) theory. Figure from Ref. [55].

tering leads to Cooper pair breaking, altering the superconducting state. An increase of pair breakers leads to a decrease of the mean field parameters such as the critical temperature and superconducting gap [51]. In addition, the pairing potential and quasiparticle energy gap no longer are the same (without pair breaking, both are set by the value of Δ), giving rise to gapless superconductivity [6]. The Kondo effect gives rise to impurity bound states below the gap, which form a band of subgap states with increasing impurity concentration [52, 53]. This band of subgap states has been found experimentally in a variety of systems, for example in Pb with Mn, and in proximitised structures, see Fig. 2.6, and can be well described by the theory by Zittartz, Bringer and Müller-Hartmann [56].

Table 2.1: Kondo temperatures (in Kelvin) for $3d$ transition metals in common metals [50].

Host \ Impurity	Cr	Mn	Fe
Cu	1.0	0.01	25
Ag	~ 0.02	0.04	~ 3
Au	~ 0.01	< 0.01	0.3
Al	1200	530	> 5000

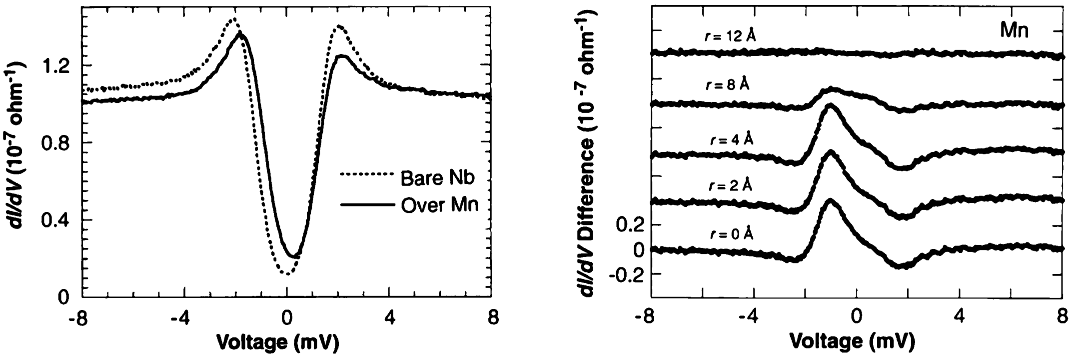

Figure 2.7: The differential conductance measured over a single Mn atom placed on Nb using scanning tunnelling microscopy. The left figure shows the conductance over bare Nb and over the Mn atom, the difference for various distances is shown in the right figure. Very locally, within a nanometer around the Mn atom, a clear asymmetry is observed in the conductance. Figure from Ref. [58].

An interesting contradiction arises at very low temperatures: In superconductors all electrons are paired and the Cooper pairs, having no net spin, are unable to screen the impurity; this while in normal metals the impurity is so well screened it is effectively nonmagnetic. This issue was addressed by Sakurai [57], who showed that in the presence of a strong ($\epsilon_0 \ll \Delta$) magnetic impurity the groundstate changes, containing a localised quasiparticle to screen the impurity. Quasiparticles in superconductors, Bogoliubov quasiparticles, are superpositions of electrons and holes. Normally in a superconductor both are favoured equally as a function of excitation energy (one exception is charge imbalance), see Ref. [6]: the differential conductance is therefore symmetric around the Fermi level. Interestingly, the changes in the groundstate imply particle-hole asymmetry on a very local scale as well [58, 59]. These local changes are not included in the impurity-averaged conventional pair breaking theories by Abrikosov and Gorkov, as well as Zittartz, Bringer and Müller-Hartmann. In 1997 Yazdani *et al.* [58] were the first to experimentally observe such a localised impurity bound state using scanning tunnelling microscopy over single Mn and Gd atoms placed on the surface of Nb, see Fig. 2.7. The differential conductance shows clear deviations within only a nanometer. Additionally, the differential conductance is asymmetric, and is understood to arise from particle-hole asymmetry brought about by the magnetic impurity [58, 59].

In Chapter 5 of this thesis we show a clear saturation of the quasiparticle recombination time at low temperatures. This saturation is reminiscent to experiments in normal metals which showed that at low temperatures timescales for quasiparticles are limited by dilute concentrations of magnetic impurities, most notably the inelastic electron-electron scattering (see Chapter 2.2.1). By analogy, we have hypothesized that low temperature recombination in superconductors could be related to magnetic impurities in the superconducting film. Modifications of the recombination time could arise from the alterations of the superconducting state such as the subgap states (related to possible quasiparticle traps [44]), the groundstate quasiparticles, the influence of the magnetic moment on the interactions between quasiparticles, as well as a possible spin-lattice coupling [60]. In order to test whether recombination is related to magnetic impurities we have implanted Mn in Ta and Al, see Chapter 6. We show that indeed the low temperature relaxation time is strongly reduced by implantation, but that this enhancement of the recombination process is not due to the magnetic moment, but due to the enhancement of disorder, possibly involving surface defects with magnetic moments.

2.3 Low frequency noise in superconducting systems

The counting of Cooper pairs and quasiparticles using superconducting resonators, for photon detection or for elucidating physical processes, is fundamentally limited by particle number fluctuations. These particle number fluctuations arise from the random generation of quasiparticles and their subsequent recombination. At the same time, other microscopic processes contribute to the noise of superconducting resonators as well. Local dipoles in dielectrics in the active region of the resonator couple to the electric fields, possibly affecting the noise properties. In addition, the time-varying orientation of magnetic moments, coupling to the magnetic fields in the resonator, would contribute to the noise. These three noise processes are apparent in the *low frequency noise*.

Interestingly, at low frequencies almost every system shows noise. Many systems with a $1/f$ or $1/f$-like power spectral density have been found [61]. Low frequency fluctuations have been encountered in SQUIDs, the most sensitive magnetometers [62], occur in everyday processes like the air temperature and wind speed [63], and even have been found in the loudness of Bach's first Brandenburg concerto [64]! While $1/f$ noise is nearly ubiquitous it is *nonuniversal*, arising from a variety of different physical processes [65]. In condensed matter physics, the spectral shape of the noise is generally attributed to an ensemble of fluctuators with a specific distribution of timescales: a $1/f$ noise spectrum can be generated by a particular superposition of Lorentzian spectra [61, 65, 66].

The superconducting resonators are ideal candidates for studying noise as they are extremely sensitive: with quality factors reaching up to a million, they can sense tiny fluctuations. At the same time, the results interest a broad community: the noise processes we discuss above play an important role in the ongoing developments in photon detection and quantum information processing. Instead of an obstacle to avoid, noise is a signal worth investigating. We start by introducing the power spectral density, and discuss the three noise processes mentioned above by reviewing recent advances in superconducting devices.

2.3.1 Power spectral density

The spectral properties of noise are described by the *power spectral density* [67], which is given by the Fourier transform of the autocorrelation, as stated by the Wiener-Khintchine theorem. This as the Fourier transform of a noise signal $x(t)$ is undefined because noise has infinite energy: $\int_{-\infty}^{\infty} |x(t)|^2 dt = \infty$ (think of Parseval's relation). This approach is valid when the noise process is strictly or weakly stationary, i.e. its main properties are time-invariant. With the autocorrelation given by $R_x(t') =< x(t)x^*(t-t') >$, the power spectral density S_x is

$$S_x(\omega) \equiv 2\mathscr{F}\{< x(t)x^*(t-t') >\} \tag{2.8}$$

It is twice the Fourier transform of the correlation function: $S_x(\omega) = 2\Phi_x(\omega)$.

The simplest example is a zero mean white noise process, where there is no correlation between different time samples: it has an autocorrelation of $R_x(t') = \sigma_x^2 \Delta t' \delta(t')$, with $\Delta t'$ a sampling time, giving a frequency independent spectrum of $S_x(\omega) = 2\sigma_x^2 \Delta t'$, with $\sigma_x^2 =< xx^* >$ the variance; examples of such processes include the Johnson noise in resistors at finite temperatures. On the other hand, a Lorentzian spectrum is the hallmark of a noise process characterised by a single timescale τ, such as for a two-level fluctuator [68]. With an autocorrelation given by $R_x(t') =< xx^* > e^{-|t'|/\tau}$, the power spectral density is

$$S_x(\omega) = 2\int_{-\infty}^{\infty} \sigma_x^2 e^{-|t'|/\tau} e^{-i\omega t'} dt' = 4\sigma_x^2 \int_0^{\infty} e^{-t'/\tau} \cos(\omega t') dt' = \frac{4\sigma_x^2 \tau}{1+(\omega\tau)^2} \tag{2.9}$$

forming a Lorentzian spectrum with a roll-off at a frequency reciprocal to the characteristic timescale.

2.3.2 Particle number fluctuations

Particle number fluctuations in a superconductor arise from the spontaneous generation and recombination of quasiparticles, leading to generation-recombination

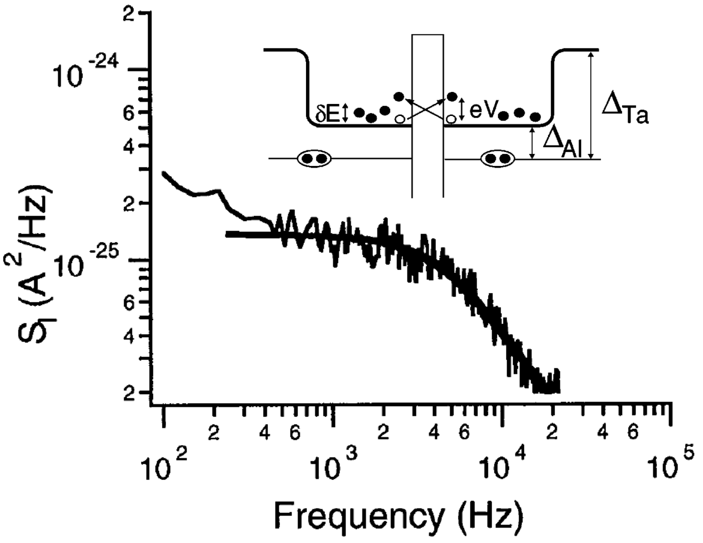

Figure 2.8: The power spectral density of the current clearly shows a Lorentzian spectrum. The inset shows the energy band diagram of the superconducting tunnel junction. Quasiparticles are confined to the Al electrodes by the higher gap Ta [70].

noise [69]. The particles are either part of the condensate or excited at energies very close the gap. As such, the electronic system can be treated as a two-level system with the quasiparticle recombination time τ_r as characteristic timescale. The variance of the quasiparticle number fluctuations is set by the total number of quasiparticles: $\sigma^2 = N_{qp}$. Using Eq. 2.9 the power spectral density is given by

$$S_N(\omega) = \frac{4N_{qp}\tau_r}{1 + (\omega\tau_r)^2} \tag{2.10}$$

These particle number fluctuations have been experimentally addressed by Wilson *et al.* [70], using a superconducting tunnel junction, see Fig. 2.8. Fluctuations in the quasiparticle number will cause fluctuations in the tunnelling current. By measurements of the current noise, a Lorentzian spectrum was found whose roll-off frequency was consistent with relaxation time measurements.

Interestingly, the product $N_{qp}\tau_r$ is temperature independent as the recombination time is reciprocally related to the quasiparticle density, see Eq. 2.6. Hence the physical process is quantified by the shape of the spectrum, not so much the absolute level: if more dominant relaxation processes are present, the noise spectrum is no longer a single Lorentzian spectrum, but will be a superposition of multiple spectra [69].

Using this analysis, we show in Chapter 5 by measurements of the noise spectra under continuous optical illumination that the quasiparticle relaxation process can be characterised by a single dominant timescale.

2.3.3 Flux noise

The existence of low temperature fluctuations in the magnetic flux has been most apparent in experiments with superconducting quantum interference devices (SQUIDs) [62]. SQUIDs consist of a superconducting ring with two tunnel barriers, forming Josephson junctions; the current through the ring depends on the phase-sensitive summation of the supercurrent passed by the two junctions [6]. SQUIDS are extremely sensitive magnetometers as the phase depends on the enclosed magnetic flux. Noise in the magnetic flux, flux noise, is presently attracting increased attention as it is critical also for Josephson-based quantum information processing. The noise has a $1/f$-like spectrum, and is found to depend only weakly on parameters like material and geometry. The origin of this noise has thus far not been identified. Proposed flux noise mechanism include electron spin locking in possible surface charge traps [71], interaction between hypothesised surface magnetic moments due to conduction electrons [72], or dangling bonds at for example the Si/SiO_2 interface [73].

The insight in the origins of flux noise is evolving, as a set of recent, unrelated experiments is pointing towards the presence of magnetic moments on the surfaces of superconducting films at low temperatures. Magnetic field-dependent measurements of the critical current in superconducting Nb and MoGe nanowires show a peak for nonzero fields [74], consistent with the paramagnetic ordering of magnetic moments. The diameter dependence indicates a surface distribution of magnetic moments. Scanning tunneling measurements on Nb show a V-shaped differential conductance, pointing towards the presence of magnetic moments in the native oxide [75]. Sendelbach *et al.* [76] have found the amount of excess flux present in both Al and Nb SQUIDs to increase with decreasing temperature, whose strength depends on the field cooled flux density. These results are consistent with the paramagnetic ordering of surface spins in the vortex cores [77].

Surface spins are relevant for our case, as they would couple to the magnetic fields in the resonator, appearing in the inductance. At the same time, magnetic moments affect the superconducting state, possibly influencing quasiparticle recombination processes (see Chapter 2.2.3).

2.3.4 Dipole fluctuators

The permittivity of a dielectric arises from the combined atomic, molecular and ionic frequency-dependent polarisability. Additionally, in disordered systems it has become clear that a significant amount of configurational defects exists, fluctuating between low lying energy states [78]. These two-level fluctuators are apparent in measurements of the low temperature heat capacity, showing a peak in the temperature dependence (this is known as the Schottky anomaly) [79]. Moreover, they bring about variations of the sound velocity and give rise to acoustic attenuation in ultrasound experiments. Some of these fluctuators have a *dipole moment* and respond to electric fields, affecting the real and imaginary part of the complex permittivity ϵ, and by extension: the phase velocity and high frequency absorptivity.

Amorphous systems are known to contain many defects, whose microscopic origins vary, giving rise to dipole two-level systems [78]. Amorphous SiO_2 for example is known to contain many dipole defects [80, 81]; these can arise from the flipping of the angles of the Si-O-Si bonds [82, 83], see inset Fig. 2.9a, the motion of groups of molecules as well as defects related to oxygen vacancies [84]. Additionally, dipole defects are brought about by foreign molecules such as OH^- ions [81, 85]. These dipole fluctuators can described as a two-level system, represented by a particle in a double well potential, see Fig. 2.9b; the characteristics, the energies and relaxation times, depend on the microscopic properties. The two-level system fluctuates between the low-energy states, each having a different dipole moment.

At low temperatures, where the frequency of the electromagnetic field is too fast for relaxation, resonant interaction of the dipole two-level systems with the electric field dominates, leading to a temperature dependence of the absolute permittivity ϵ given by [78, 81]

$$\frac{\delta\epsilon}{\epsilon} = -\frac{2p^2P}{\epsilon}\left[\mathrm{Re}\ \Psi\left(\frac{1}{2}+\frac{\hbar\omega}{2\pi ikT}\right)-\ln\left(\frac{\hbar\omega}{kT}\right)\right] \tag{2.11}$$

with p the dipole moment, P the density of states and Ψ the digamma function. In the limit $kT > \hbar\omega$ the above equation can be simplified to

$$\frac{\delta\epsilon}{\epsilon} = -\frac{2p^2P}{\epsilon}\ln\left(\frac{T}{T_0}\right) \tag{2.12}$$

with T_0 an arbitrary reference temperature. At higher temperatures relaxational interaction starts to dominate [81]. Fig. 2.9a shows such a temperature dependence in permittivity data on SiO_x.

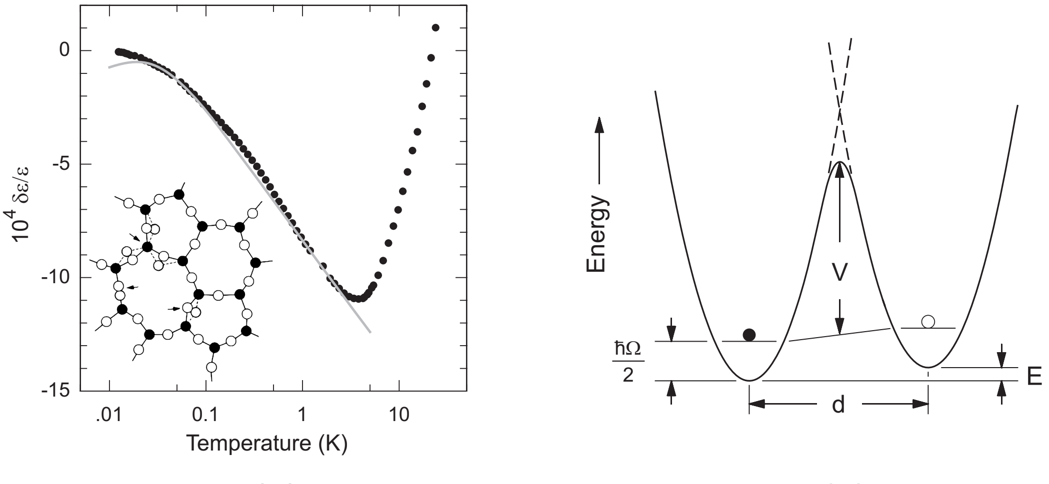

(a) (b)

Figure 2.9: (a) The temperature dependence of the permittivity of amorphous SiO_2 [86]. The solid line is Eq. 2.11. The inset shows the positions in SiO_2 which can fluctuate in configuration [83]. (b) A particle in a double well potential: $\hbar\Omega/2$ is the zero point energy, E is the energy difference between the states and V the potential barrier height.

Noise with a $1/f$ spectrum can result from a particular superposition of Lorentzian spectra of dipole two-level systems: for a noise process due to thermal activation, $\tau \propto e^{E/kT}$, $1/f$ noise results from a flat distribution of fluctuators over the energy [61, 65, 66]. The low frequency noise in the permittivity of dielectrics in the active region of a resonator translates into noise in the resonance frequency.

2.3.5 Noise and frequency deviations in superconducting resonators

One of the main themes of this thesis is the low temperature properties of superconducting resonators. In principle, these are determined by the superconductor, but in practice these resonators exhibit a large amount of frequency noise as well as deviations in the temperature dependence of the resonance frequency. A full understanding of these phenomena is emerging, although not yet complete. Here, we present an overview of the main experimental results thusfar and the proposed interpretations by the Caltech group as well as by us.

We observe a clearly present nonmonotonicity in the temperature dependence of the resonance frequency at low temperatures in superconducting resonators made of Nb, Ta and Al on Si substrates [87, 88]. Gao *et al.* [89] find a similar feature in Nb on sapphire resonators. Interestingly, we have recently found that NbTiN on Si films do not show such a dependence. However, the nonmonotonicity appears if we cover the NbTiN films with SiO_x dielectric layers and increases with the thickness of the layer. Both the data from Gao *et al.* [89] and our experimental results can be accurately fitted with Eq. 2.11. This indicates that dipole two-level systems distributed in the *volume* of dielectric layers give rise to the observed nonmonotonicity.

The superconducting resonators show substantial frequency noise. Interestingly, Gao *et al.* [90] find that the noise has a comparable level for a variety of superconducting materials (Al, Nb) and dielectric substrates (Si, Ge, sapphire). Moreover, the noise level depends on the power inside the resonator, following $S \propto 1/P^{0.5}$. The noise levels as well as the power dependence are comparable to what we find in resonators of Al, Ta and NbTiN on Si substrates.

A challenge is to reduce the noise, which requires knowledge about the location of the noise source as well as the physical mechanisms that cause the noise. The Caltech group has conjectured that this frequency noise is due to fluctuating two-level systems with a dipole moment, located in the dielectric materials, either in the bulk of the substrate, the interfaces or the surfaces. In the proposed interpretation the low temperature resonance frequency deviations with temperature are coupled to the frequency noise via the temperature-dependent, time-varying permittivity $\epsilon(\mathbf{r}, t, T)$ [89, 90, 91]. The peculiar power dependence of the noise can then be explained by assuming the two-level systems are saturated due to the high levels of electric fields used [91].

The noise also depends on the geometry, as the noise decreases with increasing width of the transmission line. The experimentally observed scaling indicates that the noise source is located on surfaces instead of in the bulk [91]. By increasing the volume to surface ratio on the open end of the resonator, where the electric fields are strongest, the noise can be significantly decreased [92].

Importantly, in Chapter 7 we find that the noise level of NbTiN on Si resonators increases as soon as SiO_x is present, but remains unchanged with increasing thickness, indicating that the noise is dominantly due to processes occurring at *interfaces*. More specifically, the superconductor-dielectric interface or/and the interface between the substrate and the sputtered dielectric layer. Additionally, the noise levels we find in uncovered NbTiN are comparable to those in Ta and Al, while the uncovered NbTiN does not show a nonmonotonicity. The noise results indicate no direct coupling between frequency deviations with temperature and frequency noise. Our results point towards the noise arising at interfaces, which is in agreement with the measurements on the width dependence of the noise.

The identification of the noise arising at the interfaces is an important step towards using these resonators for photon detection. The noise can be decreased by increasing the volume to surface ratio as well as by directly addressing the interfaces. When optimising the geometry for photon detection the volume of the central line is preferably kept small, as it acts as detector volume. In Chapter 8 we show that the noise decreases by almost an order of magnitude when widening only the gaps of the resonator transmission line while keeping the central line the same.

2.4 High frequency response of a superconducting film

The essential part of this thesis is probing the photo-induced changes in and subsequent relaxation of the superconducting state; the variation in the Cooper pair density and in the amount and distribution of quasiparticles over the energy leads to a change in the high frequency response of the superconducting film. This high frequency response is controlled by the *complex conductivity.*

Hallmarks of superconductivity are its zero resistance and its expulsion of magnetic fields. Yet, the electromagnetic fields penetrate the surface with a magnetic penetration depth λ, analogously to the skin depth in normal metals. When applying a microwave signal the charge carriers 'dance to the tune': the time-varying electric fields accelerate and decelerate both the Cooper pair condensate and the quasiparticle excitations. The quasiparticles scatter in much the same way as normal electrons do, bringing about Ohmic dissipation, limiting the *real part of the conductivity.* On the other hand, the non-dissipative, accelerative response of the Cooper pairs leads to a kinetic inductance and *imaginary part of the conductivity.* The electrodynamic response of the superconductor can be treated as the superposition of the response of the condensate and the quasiparticles, this is called the two-fluid model [6]. Applying the Drude model, the real part of the conductivity is given by: $\sigma_1 = n_n e^2 \tau / m$, with n_n the normal electron density and τ the elastic scattering time; and the imaginary part is: $\sigma_2 = n_s e^2 / m\omega$, with n_s the phenomenological superconducting electron density [6]. These approximations are intuitive, relating variations in the quasiparticle density n_{qp} or superconducting electron density n_s to changes in the complex conductivity.

The electrodynamic response is controlled by two lengthscales: the magnetic penetration depth λ and the coherence length ξ. When the coherence length is much shorter than the penetration depth, $\xi \ll \lambda$, the electromagnetic fields pretty

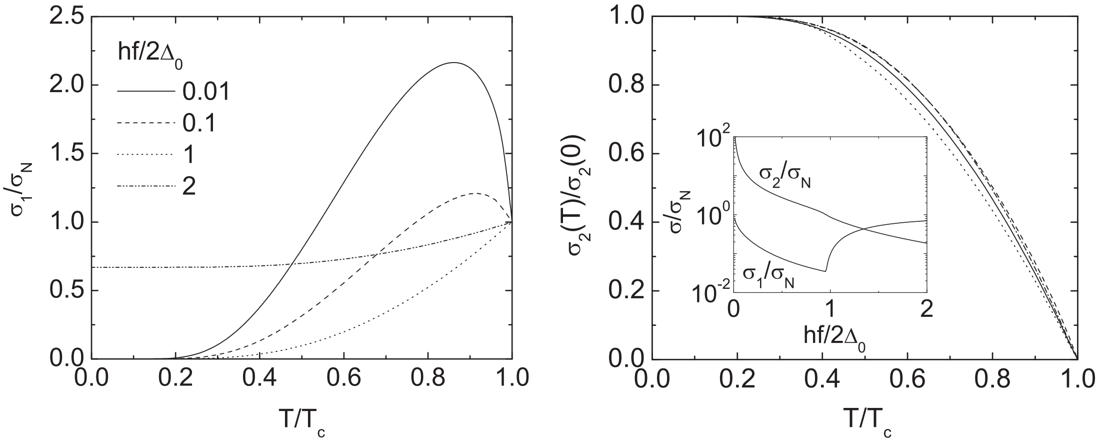

Figure 2.10: The temperature dependence of the real part and imaginary part of the complex conductivity for frequencies far below and near the gap frequency (Eq. 2.14). Left: At high temperature and for frequencies near the gap the value of σ_1/σ_N becomes significant, indicative of a large microwave absorptivity. Right: The variation of $\sigma_2(T)/\sigma_2(0)$ shows a very comparable temperature dependence over the frequencies, indicative of the decrease in the Cooper pair density. The inset shows the frequency dependence at $T/T_c = 0.5$ ($T_c = 9.2$ K).

much stay the same within the size of a Cooper pair. Intuitively, the Cooper pairs are able to locally probe the electromagnetic field; hence the current density $\mathbf{J}(\mathbf{r})$ depends only on the properties at coordinate $\mathbf{r}$: the response is *local.* On the other hand, when the coherence length is larger than the penetration depth, $\xi \gg \lambda$, the field rapidly decays within the volume occupied by a Cooper pair. Intuitively, the Cooper pair 'feels' only the average within its size. Consequently, the current density $\mathbf{J}(\mathbf{r})$ depends on the properties within a distance ξ. Hence, the response is *non-local.*

The electrodynamic response is also affected by disorder, as the coherence length ξ depends on the electron mean free path l_e. For clean films with long mean free paths, $l_e \gg \xi_0$, the low temperature coherence length is given by $\xi = \xi_0$. For dirty films with short mean free paths, $l_e \ll \xi_0$, the Ginzburg-Landau coherence length is given at low temperatures by $\xi = 0.86\sqrt{\xi_0 l_e}$ [6]. Visibly, there is a large overlap in the above definitions: in a dirty, disordered film the electron mean free path is short and the resistivity is high, hence the ξ is small and λ is large (see below), implying the local limit. The other way around defines the extreme anomalous limit: clean films with a non-local response.

The microscopic picture of the electrodynamic response was developed by Mattis and Bardeen [93]. They arrived at the following expression for the current density,

$$\mathbf{J}_\omega(\mathbf{r}) = C \int \frac{\mathbf{R}[\mathbf{R}\cdot\mathbf{A}_\omega(\mathbf{r}')]}{R^4} I(\omega, R, f(E)) e^{-R/l_e} d\mathbf{r}' \tag{2.13}$$

with $\mathbf{R} = \mathbf{r} - \mathbf{r}'$, C a constant, $\mathbf{A}$ the vector potential, ω the radial frequency and $I(\omega, R, f(E))e^{-R/l_e}$ the response kernel. Both in the extreme anomalous limit, where the response is non-local and $I(\omega, R, f(E))$ has only a weak R-dependence and drops out of the integral; as well as in the dirty limit, where the response kernel can be approximated by a local response only, the integral can be simplified. Then, the complex conductivity $\sigma_1 - i\sigma_2$, valid in the dirty and extreme anomalous limit, is given by

$$\begin{aligned}
\frac{\sigma_1}{\sigma_N} &= \frac{2}{\hbar\omega}\int_\Delta^\infty [f(E) - f(E+\hbar\omega)] g_1(E) dE \\
&\quad + \frac{1}{\hbar\omega}\int_{\Delta-\hbar\omega}^{-\Delta} [1 - 2f(E+\hbar\omega)] g_1(E) dE \\
\frac{\sigma_2}{\sigma_N} &= \frac{1}{\hbar\omega}\int_{\max(\Delta-\hbar\omega,-\Delta)}^{\Delta} [1 - 2f(E+\hbar\omega)] g_2(E) dE
\end{aligned} \tag{2.14}$$

with

$$\begin{aligned}
g_1(E) &= \left(1 + \tfrac{\Delta^2}{E(E+\hbar\omega)}\right) N_S(E) N_S(E+\hbar\omega) \\
g_2(E) &= \tfrac{E(E+\hbar\omega)+\Delta^2}{\sqrt{(E+\hbar\omega)^2-\Delta^2}\sqrt{\Delta^2-E^2}} = -i g_1(E)
\end{aligned} \tag{2.15}$$

The second part of the expression for σ_1 is relevant for $\hbar\omega > 2\Delta$; σ_n is the normal state conductivity. The complex conductivity is controlled by the *quasiparticle energy distribution*, *density of states and energy gap*, *photon energy* and *case II coherence factors*, relevant for electromagnetic absorption [6]. For a thermal distribution at temperature T, see Appendix B for the derivation, the above equations can be simplified in the limit $kT, \hbar\omega < 2\Delta$ to

$$\begin{aligned}
\frac{\sigma_1}{\sigma_N} &= \frac{4\Delta}{\hbar\omega} e^{-\Delta/kT} \sinh\left(\frac{\hbar\omega}{2kT}\right) K_0\left(\frac{\hbar\omega}{2kT}\right) \\
\frac{\sigma_2}{\sigma_N} &= \frac{\pi\Delta}{\hbar\omega}\left[1 - 2e^{-\Delta/kT} e^{-\hbar\omega/2kT} I_0\left(\frac{\hbar\omega}{2kT}\right)\right]
\end{aligned} \tag{2.16}$$

with I and K modified Bessel functions of the first and second kind. The temperature dependence of σ_1 and σ_2 is shown in Fig. 2.10.

For the local limit, the surface impedance is a direct result of Maxwell's equations, giving for dirty limit thick films [95]

$$Z_S = \sqrt{\frac{i\mu_0\omega}{\sigma_1 - i\sigma_2}} = R_S + i\omega L_S \tag{2.17}$$

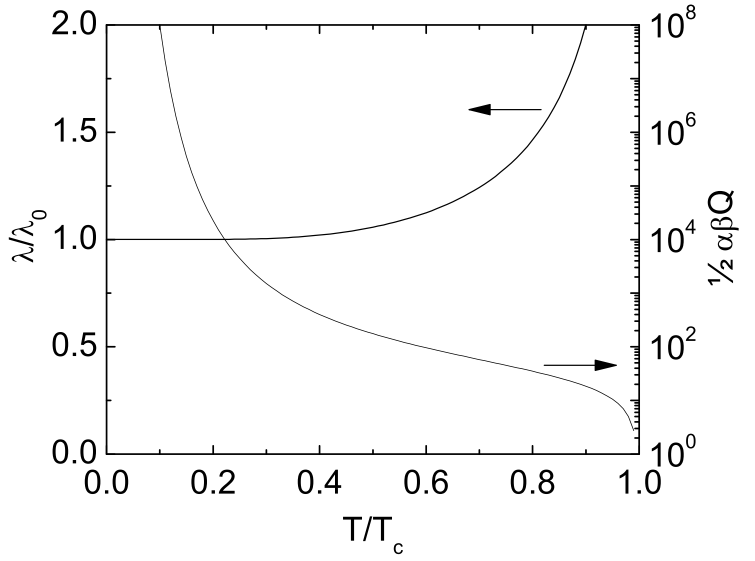

Figure 2.11: The temperature dependence of the magnetic penetration depth and quality factor ($\frac{\alpha\beta}{2}Q = \frac{\sigma_2}{\sigma_1}$) for $\hbar\omega = 0.01 \cdot 2\Delta_0$. This frequency falls in the 1-10 GHz range with the materials we use.

At low temperatures $\sigma_2 \gg \sigma_1$ and $Z_S \approx \sqrt{\frac{\mu_0\omega}{\sigma_2}}(\frac{\sigma_1}{2\sigma_2} + i)$; this relation shows that the surface reactance is positive, and can be expressed as surface inductance. Using Eq. 2.19,

$$\begin{aligned} R_S &= \sqrt{\frac{\mu_0\omega}{\sigma_2}}\frac{\sigma_1}{2\sigma_2} = \mu_0\omega\lambda\frac{\sigma_1}{2\sigma_2} \\ L_S &= \sqrt{\frac{\mu_0}{\omega\sigma_2}} = \mu_0\lambda \end{aligned} \tag{2.18}$$

the magnetic penetration depth is then given by (see also Ref. [94])

$$\lambda(\omega, T) = \frac{1}{\sqrt{\mu_0\omega\sigma_2(\omega, T)}} \tag{2.19}$$

note that at $T = 0$ this is equal to $\lambda(T = 0) = \lambda_L(0)\sqrt{\frac{\xi_0}{l_e}} = \sqrt{\frac{\hbar\rho}{\mu_0\pi\Delta_0}}$, with the London magnetic penetration depth given by: $\lambda_L(0) = \sqrt{m/\mu_0 n_s e^2} = \sqrt{\rho l_e/\mu_0 v_F}$ [6].

For arbitrary thickness d the surface resistance in the dirty limit is given by [95]

$$Z_S = \sqrt{\frac{i\mu_0\omega}{\sigma_1 - i\sigma_2}} \coth\left(\frac{d}{\lambda}\sqrt{1 + i\frac{\sigma_1}{\sigma_2}}\right) \tag{2.20}$$

with λ the bulk value. For $\sigma_2 \gg \sigma_1$, using $\coth(x+iy) \simeq \coth(x) - \frac{iy}{\sinh^2(x)}$ for $y \ll x$,

$$\begin{aligned} R_S &= \mu_0 \omega \lambda \frac{\sigma_1}{2\sigma_2} \beta \coth\left(\frac{d}{\lambda}\right) \\ L_S &= \mu_0 \lambda \coth\left(\frac{d}{\lambda}\right) \end{aligned} \tag{2.21}$$

with $\beta = 1 + \frac{2d/\lambda}{\sinh(2d/\lambda)}$; for the bulk limit: $\beta = 1$, and for the thin film limit: $\beta = 2$. The effective magnetic penetration depth for perpendicular fields is $\lambda_{eff} = \lambda \coth(\frac{d}{\lambda})$, which has been experimentally verified [96]. Quality factors of dirty limit superconducting cavities are then given by

$$Q = \frac{\omega L_{tot}}{R} = \frac{1}{\alpha}\frac{\omega L_S}{R_S} = \frac{2}{\alpha\beta}\frac{\sigma_2}{\sigma_1} \tag{2.22}$$

with $\alpha = L_S/L_{tot}$ the fraction of kinetic to total (kinetic+geometric) inductance.

A variation in the complex conductivity leads to changes in the kinetic inductance and quality factor

$$\begin{aligned} \frac{\delta L_S}{L_S} &= \beta \frac{\delta\lambda}{\lambda} = -\frac{\beta}{2}\frac{\delta\sigma_2}{\sigma_2} \\ \frac{\delta Q}{Q} &= -\left(\frac{\delta\sigma_1}{\sigma_1} - \frac{\delta\sigma_2}{\sigma_2}\right) \end{aligned} \tag{2.23}$$

References

[1] N. W. Ashcroft and N. D. Mermin, *Solid state physics*, (Thomson Learning, 1976).

[2] D. Pines and P. Nozières, *The theory of quantum liquids I*, (Addison-Wesley Publishing Co., 1989).

[3] L. N. Cooper, *Bound electron pairs in a degenerate Fermi gas*, Phys. Rev. **104**, 1189 (1956).

[4] J. Bardeen, L. N. Cooper, and J. R. Schrieffer, *Theory of superconductivity*, Phys. Rev. **108**, 1175 (1957).

[5] J. B. Ketterson and S. N. Song, *Superconductivity*, (Cambridge University Press, 1999).

[6] M. Tinkham, *Introduction to Superconductivity*, (McGraw-Hill, New York, 1996).

[7] W. L. McMillan, Phys. Rev. **167**, 331 (1968).

[8] H. Kamerlingh Onnes, *Further experiments with liquid Helium. G. On the electrical resistance of pure metals, etc. VI. On the sudden change in the rate at which resistance of mercury disappears*, Comm. Phys. Lab. Univ. Leiden, No. 124C, 1911.

[9] P. W. Anderson, *Theory of dirty superconductors*, J. Phys. Chem. Solids **11**, 26 (1959).

[10] J. J. Lin and J. P. Bird, *Recent experimental studies of electron dephasing in metal and semiconductor mesoscopic structures*, J. Phys.: Cond. Mat. **14**, R501 (2002).

[11] P. Santhanam and D. E. Prober, *Inelastic electron-scattering mechanisms in clean aluminum films*, Phys. Rev. B **29**, 3733 (1984).

[12] M. Meschke, W. Guichard, and J. P. Pekola, *Single-mode heat conduction by photons*, Nature **444**, 187 (2006).

[13] H. Pothier, S. Guéron, Norman O. Birge, D. Esteve, and M. H. Devoret, *Energy Distribution Function of Quasiparticles in Mesoscopic Wires*, Phys. Rev. Lett. **79**, 3490 (1997).

[14] B. L. Altshuler and A. G. Aronov in *Electron-electron interactions in disordered systems*, ed. by A. L. Efros and M. Pollak, (Elsevier, Amsterdam, 1985).

[15] B. Huard, *Interactions between electrons, mesoscopic Josephson effect and asymmetric current fluctuations*, Ph. D. Thesis, Pierre and Marie Curie University (2006).

[16] A. Anthore, F. Pierre, H. Pothier, and D. Esteve, *Magnetic-field-dependent quasiparticle energy relaxation in mesoscopic wires*, Phys. Rev. Lett. **90**, 076806 (2003).

[17] F. Pierre, A. B. Gougam, A. Anthore, H. Pothier, D. Esteve, and N. O. Birge, *Dephasing of electrons in mesoscopic metal wires*, Phys. Rev. B **68**, 085413 (2003).

[18] L. Saminadayar, P. Mohanty, R. A. Webb, P. Degiovanni, and C. Bäuerle, *Electron coherence at low temperatures: The role of magnetic impurities*, Physica E **40**, 12 (2007).

[19] B. Huard, A. Anthore, N. O. Birge, H. Pothier, and D. Esteve, *Effect of magnetic impurities on energy exchange between electrons*, Phys. Rev. Lett. **95**, 036802 (2005).

[20] A. Kaminski and L. I. Glazman, *Electron Energy Relaxation in the Presence of Magnetic Impurities*, Phys. Rev. Lett. **86**, 2400 (2001).

[21] T. Capron, Y. Niimi, F. Mallet, Y. Baines, D. Mailly, F. Y. Lo, A. Melnikov, A. D. Wieck, L. Saminadayar, and C. Bäuerle, *Low-temperature dephasing in irradiated metallic wires*, Phys. Rev. B **77**, 033102 (2008).

[22] Yu. N. Ovchinnikov and V. Z. Kresin, *Nonstationary state of superconductors: Application to nonequilibrium tunneling detectors*, Phys. Rev. B **58**, 12416 (1998).

[23] A. G. Kozorezov, A. F. Volkov, J. K. Wigmore, A. Peacock, A. Poelaert, and R. den Hartog, *Quasiparticle-phonon downconversion in nonequilibrium superconductors*, Phys. Rev. B **61**, 11807 (2000).

[24] B. I. Miller and A. H. Dayem, *Relaxation and recombination times of quasiparticles in superconducting Al thin films*, Phys. Rev. Lett. **18**, 1000 (1967).

[25] J. R. Schrieffer and D. M. Ginsberg, *Calculation of the Quasiparticle Recombination Time in a Superconductor*, Phys. Rev. Lett. **8**, 207 (1962).

[26] D. M. Ginsberg, *Upper Limit for Quasi-Particle Recombination Time in a Superconductor*, Phys. Rev. Lett. **8**, 204 (1962).

[27] M. Reizer, *Electron-electron relaxation in two-dimensional impure superconductors*, Phys. Rev. B **61**, 7108 (2000).

[28] T. M. Klapwijk, P. A. van der Plas, and J. E. Mooij, *Electron-electron scattering in dirty three-dimensional aluminum films*, Phys. Rev. B **33**, 1474 (1986).

[29] S. B. Kaplan, C. C. Chi, D. N. Langenberg, J. J. Chang, S. Jafarey, and D. J. Scalapino, *Quasiparticle and phonon lifetimes in superconductors*, Phys. Rev. B **14**, 4854 (1976).

[30] B. Keck and A. Schmid, *Superconductivity and electron-phonon interaction in impure simple metals*, J. Low Temp. Phys. **24**, 611 (1976).

[31] V. F. Gantmakher, *The experimental study of electron-phonon scattering in metals*, Rep. Prog. Phys. **37**, 317 (1974).

[32] J. Rammer and A. Schmid, *Destruction of phase coherence by electron-phonon interactions in disordered conductors*, Phys. Rev. B **34**, 1352 (1986).

[33] A. Sergeev and V. Mitin, *Electron-phonon interaction in disordered conductors: Static and vibrating scattering potentials*, Phys. Rev. B **61**, 6041 (2000).

[34] E. M. Gershenzon, M. E. Gershenzon, G. N. Gol'tsman, A. M. Lyul'kin, A. D. Semenov, and A. V. Sergeev, *Electron-phonon interaction in ultrathin Nb films*, Sov. Phys. JETP **70**, 505 (1990).

[35] M. E. Gershenson, D. Gong, T. Sato, B. S. Karasik, A. V. Sergeev, *Millisecond electronphonon relaxation in ultrathin disordered metal films at millikelvin temperatures*, Appl. Phys. Lett. **79**, 2049 (2001).

[36] J. Haust, M. Burst, R. Haueisen, and G. Weiss, *Low temperature acoustic properties of poly-crystalline aluminium*, J. Low Temp. Phys. **137**, 523 (2004).

[37] S. B. Kaplan, *Acoustic matching of superconducting films to substrates*, J. Low. Temp. Phys. **37**, 343, (1979).

[38] A. Rothwarf and B. N. Taylor, *Measurement of recombination lifetimes in superconductors*, Phys. Rev. Lett. **19**, 27 (1967).

[39] K. E. Gray, *Steady state measurements of the quasiparticle lifetime in superconducting Al*, J. Phys. F: Metal Phys. **1**, 290 (1971).

[40] A. Peacock, P. Verhoeve, N. Rando, A. van Dordrecht, B. G. Taylor, C. Erd, M. A. C. Perryman, R. Venn, J. Howlett, D. J. Goldie, J. Lumley, and M. Wallis, *Single optical photon detection with a superconducting tunnel junction*, Nature **381**, 135 (1996).

[41] P. Verhoeve, R. den Hartog, A. G. Kozorezov, D. Martin, A. van Dordrecht, J. K. Wigmore, and A. Peacock, *Time dependence of tunnel statistics and the energy resolution of superconducting tunnel junctions*, J. Appl. Phys. **92**, 6072 (2002).

[42] T. Nussbaumer, Ph. Lerch, E. Kirk, A. Zehnder, R. Füchslin, P. F. Meier, and H. R. Ott, *Quasiparticle diffusion in tantalum using superconducting tunnel junctions*, Phys. Rev. B **61**, 9719 (2000).

[43] L. Li, L. Frunzio, C. M. Wilson, and D. E. Prober, *Quasiparticle nonequilibrium dynamics in a superconducting Ta film*, J. Appl. Phys. **93**, 1137 (2003).

[44] A. G. Kozorezov, J. K. Wigmore, A. Peacock, A. Poelaert, P. Verhoeve, R. den Hartog, and G. Brammertz, *Local trap spectroscopy in superconducting tunnel junctions*, Appl. Phys. Lett. **78**, 3654 (2001).

[45] J. M. Martinis, M. Ansmann and J. Aumentado, *Energy Decay in Josephson Qubits from Non-equilibrium Quasiparticles*, arXiv:0904.2171.

[46] M. D. Shaw, R. M. Lutchyn, P. Delsing, and P. M. Echternach, *Kinetics of nonequilibrium quasiparticle tunneling in superconducting charge qubits*, Phys. Rev. B **78**, 024503 (2008).

[47] P. W. Anderson, *Localized magnetic states in metals*, Phys. Rev. **124**, 41 (1961).

[48] L. Kouwenhoven and L. Glazman, *Revival of the Kondo effect*, Physics World **14**, 33 (2001).

[49] J. Kondo, *Resistance minimum in dilute magnetic alloys*, Prog. Theoret. Phys. **32**, 37 (1964).

[50] D. K. Wohlleben and B. R. Coles, *Formation of local moments in metals*, in *Magnetism vol. V*, edited by H. Suhl, (Academic, New York, 1973).

[51] A. A. Abrikosov and L. P. Gorkov, *Contribution to the theory of superconducting alloys with paramagnetic impurities*, Sov. Phys. JETP **12**, 1243 (1961).

[52] M. Brian Maple, *Paramagnetic impurities in superconductors*, in *Magnetism vol. V*, edited by H. Suhl, (Academic, New York, 1973).

[53] A. V. Balatsky, I. Vekhter, J. X. Zhu, *Impurity-induced states in conventional and unconventional superconductors*, Rev. Mod. Phys. **78**, 373 (2006).

[54] W. Bauriedl, P. Ziemann, and W. Buckel, *Electron-Tunneling Observation of Impurity Bands in Superconducting Manganese-Implanted Lead*, Phys. Rev. Lett. **47**, 1163 (1981).

[55] L. Dumoulin, E. Guyon, and P. Nedellec, *Tunneling study of localized bands in superconductors with magnetic impurities (normal Kondo alloys in the superconducting proximity)*, Phys. Rev. B **16**, 1086 (1977).

[56] J. Zittartz, A. Bringer, and E. Müller-Hartmann, *Impurity bands in superconductors with magnetic impurities*, Solid State Comm. **10**, 513 (1972).

[57] A. Sakurai, *Comments on superconductors with magnetic impurities*, Prog. Theoret. Phys. **44**, 1472 (1970).

[58] A. Yazdani, B. A. Jones, C. P. Lutz, M. F. Crommie, and D. M. Eigler, *Probing the local effects of magnetic impurities on superconductivity*, Science **275**, 1767 (1997).

[59] M. E. Flatté and J. M. Byers, *Local electronic structure of defects in superconductors*, Phys. Rev. B **56**, 11213 (1997).

[60] A. G. Kozorezov, A. A. Golubov, J. K. Wigmore, D. Martin, P. Verhoeve, R. A. Hijmering, and I. Jerjen, *Inelastic scattering of quasiparticles in a superconductor with magnetic impurities*, Phys. Rev. B **78**, 174501 (2008).

[61] P. Dutta and P. M. Horn, *Low-frequency fluctuations in solids: $1/f$ noise*, Rev. Mod. Phys. **53**, 497 (1981).

[62] F. C. Wellstood, C. Urbina, and J. Clarke, *Low-frequency noise in dc superconducting quantum interference devices below 1 K*, Appl. Phys. Lett. **50**, 772 (1987).

[63] J. I. Yano, R. Blender, C. D. Zhang, and K. Fraedrich, *$1/f$ noise and pulse-like events in the tropical atmospheric surface variabilities*, Q. J. Royal Meteor. Soc. **130**, 1697 (2004).

[64] R. F. Voss and J. Clarke, *$1/f$ noise in music and speech*, Nature **258**, 317 (1975).

[65] M. B. Weissman, *$1/f$ noise and other slow, nonexponential kinetics in condensed matter*, Rev. Mod. Phys. **60**, 537 (1988).

[66] C. C. Yu, *Why study noise due to two level systems: a suggestion for experimentalists*, J. Low Temp. Phys. **137**, 251 (2004).

[67] Sh. Kogan, *Electronic noise and fluctuations in solids*, (Cambridge University Press, 1996).

[68] S. Machulp, *Noise in semiconductors: spectrum of a two-parameter random signal*, J. Appl. Phys. **25**, 341 (1954).

[69] C. M. Wilson and D. E. Prober, *Quasiparticle number fluctuations in superconductors*, Phys. Rev. B **69**, 094524 (2004).

[70] C. M. Wilson, L. Frunzio, and D. E. Prober, *Time-resolved measurements of thermodynamic fluctuations of the particle number in a nondegenerate Fermi gas*, Phys. Rev. Lett. **87**, 067004 (2001).

[71] R. H. Koch, D. P. DiVincenzo, and J. Clarke, *Model for 1/f flux noise in SQUIDs and qubits*, Phys. Rev. Lett. **98**, 267003 (2007).

[72] L. Faoro and L. B. Ioffe, *Microscopic Origin of Low-Frequency Flux Noise in Josephson Circuits*, Phys. Rev. Lett. **100**, 227005 (2008).

[73] R. de Sousa, *Dangling-bond spin relaxation and magnetic 1/f noise from the amorphous-semiconductor/oxide interface: Theory*, Phys. Rev. B **76**, 245306 (2007).

[74] A. Rogachev, T. C. Wei, D. Pekker, A. T. Bollinger, P. M. Goldbart, and A. Bezryadin, *Magnetic-field enhancement of superconductivity in ultranarrow wires*, Phys. Rev. Lett. **97**, 137001 (2006).

[75] T. Proslier, J. F. Zasadzinski, L. Cooley, C. Antoine, J. Moore, J. Norem, M. Pellin, and K. E. Gray, *Tunneling study of cavity grade Nb: Possible magnetic scattering at the surface*, Appl. Phys. Lett. **92**, 212505 (2008).

[76] S. Sendelbach, D. Hover, A. Kittel, M. Mück, J. M. Martinis, and R. McDermott, *Magnetism in SQUIDs at millikelvin temperatures*, Phys. Rev. Lett. **100**, 227006 (2008).

[77] S. Sendelbach, D. Hover, A. Kittel, M. Mck, John M. Martinis, and R. McDermott, *Calculations for magnetism in SQUIDs at millikelvin temperatures*, arXiv:0802.1511.

[78] W. A. Phillips, *Two-level states in glasses*, Rep. Prog. Phys. **50**, 1657 (1987).

[79] C. Kittel and H. Kroemer, *Thermal physics*, (Second Edition, W. H. Freeman and Company, New York, 1997).

[80] B. Golding, M. von Schickfus, S. Hunklinger, and K. Dransfeld, *Intrinsic electric dipole moment of tunneling systems in silica glasses*, Phys. Rev. Lett. **43**, 1817 (1979).

[81] M. von Schickfus and S. Hunklinger, *Dielectric coupling of low-energy excitations in vitreous silica to electromagnetic waves*, J. Phys. C: Solid State Phys. **9**, L439 (1976).

[82] J. Reinisch and A. Heuer, *What Is Moving in Silica at 1 K? A Computer Study of the Low-Temperature Anomalies*, Phys. Rev. Lett. **95**, 155502 (2005).

[83] C. Enss and S. Hunklinger, *Low-Temperature Physics*, (Springer Verlag, 2005).

[84] D. L. Griscom, *Defect structure of glasses - some outstanding questions in regard to vitreous silica*, J. Non-Crystalline Solids **73**, 51 (1985).

[85] J. M. Martinis, K. B. Cooper, R. McDermott, M. Steffen, M. Ansmann, K. D. Osborn, K. Cicak, S. Oh, D. P. Pappas, R. W. Simmonds, and C. C. Yu, *Decoherence in Josephson Qubits from Dielectric Loss*, Phys. Rev. Lett. **95**, 210503 (2005).

[86] M. Brandt, *Einfluss von Kernquadrupolmomenten auf die Amplitude von Polarisationsechos in amorphen Festkörpern*, Ph. D. Thesis, University of Heidelberg (2004).

[87] R. Barends, J. J. A. Baselmans, J. N. Hovenier, J. R. Gao, S. J. C. Yates, T. M. Klapwijk, and H. F. C. Hoevers, *Niobium and tantalum high Q resonators for photon detectors*, IEEE Trans. Appl. Sup. **17**, 263 (2007).

[88] J. J. A. Baselmans, S. J. C. Yates, R. Barends, Y. J. Y. Lankwarden, J. R. Gao, H. F. C. Hoevers, and T. M. Klapwijk, *Noise and sensitivity of aluminum kinetic inductance detectors for sub-mm astronomy*, J. Low Temp. Phys. **151**, 524 (2008).

[89] J. Gao, M. Daal, A. Vayonakis, S. Kumar, J. Zmuidzinas, B. Sadoulet, B. A. Mazin, P. K. Day, and H. G. LeDuc, *Experimental evidence for a surface distribution of two-level systems in superconducting lithographed microwave resonators*, Appl. Phys. Lett. **92**, 152505 (2008).

[90] J. Gao, J. Zmuidzinas, B. A. Mazin, H. G. LeDuc, and P. K. Day, *Noise properties of superconducting coplanar waveguide microwave resonators*, Appl. Phys. Lett. **90**, 102507 (2007).

[91] J. Gao, M. Daal, J. M. Martinis, A. Vayonakis, J. Zmuidzinas, B. Sadoulet, B. A. Mazin, P. K. Day, and H. G. LeDuc, *A semiempirical model for two-level system noise in superconducting microresonators*, Appl. Phys. Lett. **92**, 212504 (2008).

[92] O. Noroozian, *New resonator designs for reduced frequency noise in microwave kinetic inductance detectors*, 2nd Workshop on the Physics and Applications of Superconducting Microresonators, SRON Utrecht, the Netherlands, 19-20 June, 2008.

[93] D. C. Mattis and J. Bardeen, *Theory of the anomalous skin effect in normal and superconducting metals*, Phys. Rev. **111**, 412 (1958).

[94] R. F. Broom and P. Wolf, *Q factor and resonance amplitude of Josephson tunnel junctions*, Phys. Rev. B, **16**, 3100 (1977).

[95] R. L. Kautz, *Picosecond pulses on superconducting striplines*, J. Appl. Phys. **49**, 308 (1978).

[96] W. H. Henkels and C. J. Kircher, *Penetration depth measurements on type II superconductors*, IEEE Trans. Magn. **MAG-13**, 63 (1977).

Chapter 3

Superconducting resonators

3.1 Introduction

Superconducting resonators are extremely sensitive probes due to their high quality factors. Quality factors reach values over 10^6, allowing for easily observing fractional changes of less than a millionth in the complex conductivity or dielectric permittivity. When used to probe the photo-induced changes in the superconducting state, these resonators become highly sensitive photon detectors. The additional advantages are their large dynamic range and the natural possibility for reading out large imaging arrays using frequency domain multiplexing. Planar quarterwave or halfwave resonators can be easily fabricated. This versatile innovation [1] was quickly picked up not only for photon detection [2, 3, 4] but also for many more applications in condensed matter physics: resonators are used in all-solid state circuit quantum information processing [5, 6], elucidating properties of dielectrics [7], controlling nanomechanical oscillators [8], narrowband quantum-limited Josephson microwave amplifiers [9], and frequency domain multiplexing for transition edge sensor bolometers [10]. Alternatively, lumped-element resonators can be used, consisting of a tightly meandered superconducting line and an interdigitated capacitor [11]. An advantage is that these resonators can be used as polarisation sensitive absorbers at submillimeter frequencies. However, their properties are coupled to the radiation absorption properties, complicating optimisation. We therefore use straightforward planar quarterwave and halfwave resonators.

The subject of this chapter is threefold: we describe the geometry and fabrication for realising these resonators, present the microwave properties for characterising these resonators, and provide a practical guide for probing these resonators. In section 3.2 we address the design of these resonators. In section 3.3 we present the microwave description for characterising these resonators, concluding with convenient expressions for the scattering parameters and time domain observables. The fabrication process in discussed in section 3.4. We conclude in section 3.5 with a practical description of the cryogenic and room temperature setup as well as an analysis of the setup noise level: the do's and don't's in the cryostat as well as the RF setup.

3.2 Design of a quarterwave resonator

3.2.1 A coplanar waveguide transmission line resonator

The microwave resonator, a *distributed* resonant circuit, consists of a transmission line with a coupler annex open end at one side and at the other side a shorted end for quarterwave resonators, see Fig. 3.1, following Refs [1, 12]. Additionally, the resonator is meandered due to its length. The meandered quarterwave transmission line resonator is a close microwave analogon of musical instruments like the trumpet, the clarinet, and the serpent in particular; all of which are acoustical quarterwave resonators. As transmission line a coplanar waveguide (CPW) is used for both the resonator and the feedline, consisting of a central line with a pair of ground planes on both sides, separated by slits in the superconducting film exposing the dielectric substrate. The coplanar waveguide can be seen as a planar version of the coaxial transmission line plugged in the back of TV sets. The resonators are coupled capacitively to the feedline near the open end by placing part of the resonator parallel to the feedline.

Quarterwave resonators are mainly used as they are shortest, their resonance frequency is given by

$$\omega_0 = \frac{2\pi}{4l\sqrt{(L_g + L_k)C}}, \tag{3.1}$$

with resonator length l, L_k the kinetic inductance, and L_g and C the geometric inductance and capacitance per unit length. The resonators are read out at their fundamental tone; resonance frequencies used lie between 3 and 10 GHz. For this frequency range wideband high electron mobiity transistor (HEMT) amplifiers, with noise as low as ten times the quantum noise, are available [13]. The resonators are several millimeters long: a 6 GHz quarterwave resonator on a Si substrate is 5 mm long.

Coplanar waveguides are described in the literature, see Refs. [14, 15]. Here, we repeat the main aspects relevant to our work. A coplanar waveguide propagates the (quasi) transverse electromagnetic (TEM) mode: the electric and magnetic fields lie in the plane perpendicular to the direction of propagation, see Fig. 3.2. The currents flow at the edges of the central line and ground planes. The central line current is equal and antiparallel to the current in the ground plane, and the return current in both sides of the groundplane is in phase (even mode). The inductance and capacitance per unit length is [14]

$$L_g = \frac{\mu_0}{4}\frac{K(k')}{K(k)} \tag{3.2}$$

$$C = 4\epsilon_0\epsilon_{eff}\frac{K(k)}{K(k')} \tag{3.3}$$

with K the complete elliptic integral of the first kind, $k = S/(S+2W)$, $k^2+k'^2 = 1$, and S the central line width and W the slit or gap width. As roughly half of the electric field lines are in vacuum and the other half are in the substrate, the

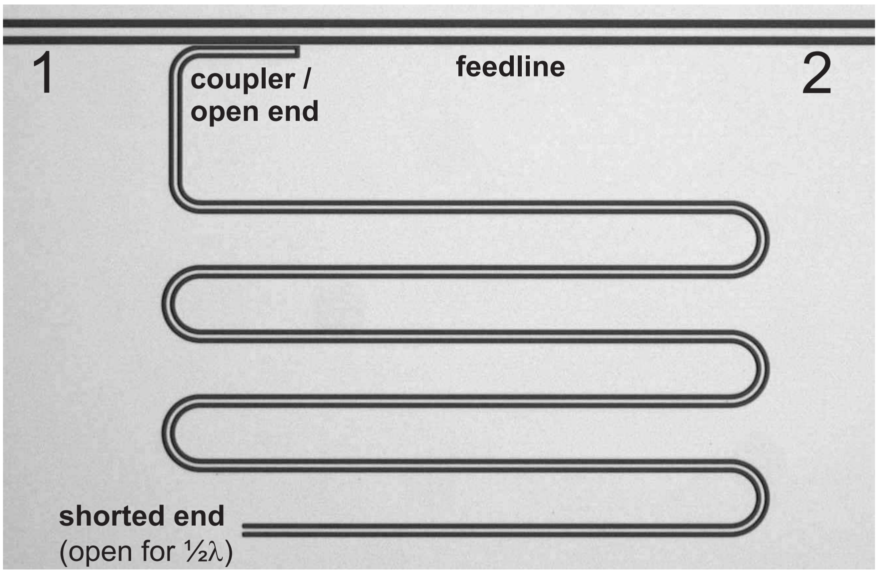

Figure 3.1: Optical micrograph of a coplanar waveguide quarter wavelength microwave resonator, formed by the superconducting film (grey) interrupted by slits exposing the substrate (black). Below the quarterwave resonator is terminated by a shorted end (open end in the case of a halfwave resonator). The resonator is capacitively coupled to the feedline by placing a part, near the open end, parallel to the feedline.

effective dielectric constant is approximately: $\epsilon_{eff} \approx (1 + \epsilon_{substrate})/2$. Typically for the resonators the central line is 3 μm and the slits are 2 μm wide while the feedline has a central line width of 10 μm and slit width of 6 μm, chosen to achieve a waveguide impedance ($Z_0 = \sqrt{L/C}$) of 50 Ω. The resonators are meandered because of their long length. Additionally, the distance between adjacent CPW-lines is an almost an order larger (standard 7 times) than its width ($S + 2W$) in order to reduce parasitic coupling.

The coplanar waveguide geometry has several advantages: As the resonator and feedline both lie in the same plane, only a single patterning step is needed, greatly simplifying fabrication. In addition, the coplanar waveguide can be widened without changing the impedance, allowing for easily connecting to the feedline using bonding wires; this technique has proven to be valuable for hot electron bolometer (HEB) mixers. Additionally, due to the proximity of the groundplanes the coplanar waveguides are well-isolated, allowing for a close packing.

The kinetic inductance L_k in Eq. 3.1 is the kinetic inductance 'as seen by the travelling wave' per unit length of the waveguide. Its value is controlled by both the surface impedance of the superconductor L_s and the waveguide geometry: $L_k = L_s g$, with g (dimension: 1/length) a geometry factor. The geometry factor,

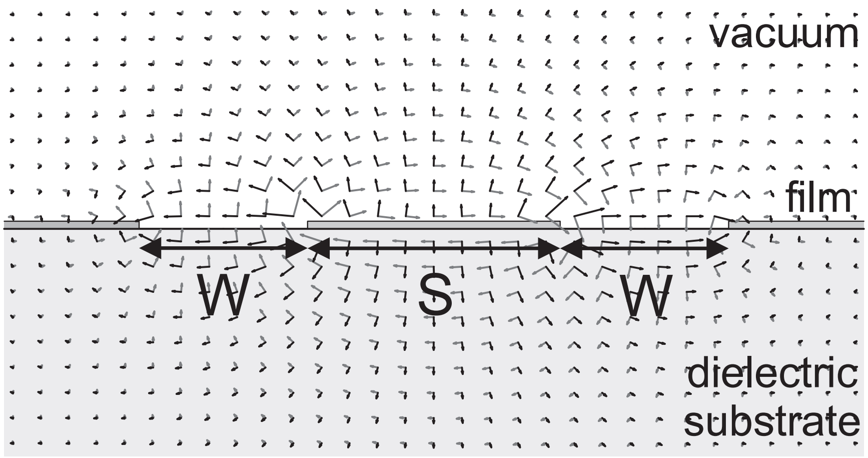

Figure 3.2: The cross section of the coplanar waveguide geometry (CPW), consisting of a central line of width S, and slits of width W in the superconducting film. The quasi transverse electromagnetic (TEM), even CPW mode is superimposed on the figure. The electric field vector is depicted by the black arrows and the magnetic field vector is depicted by the gray arrows.

accurate to within 10 % for a thickness $t < 0.05S$ and $k < 0.8$, is given by [14, 15]

$$g_c = \frac{1}{4S(1-k^2)K^2(k)}\left[\pi + \ln\left(\frac{4\pi S}{t}\right) - k\ln\left(\frac{1+k}{1-k}\right)\right] \tag{3.4}$$

$$g_g = \frac{k}{4S(1-k^2)K^2(k)}\left[\pi + \ln\left(\frac{4\pi(S+2W)}{t}\right) - \frac{1}{k}\ln\left(\frac{1+k}{1-k}\right)\right] \tag{3.5}$$

where g_c denotes the contribution of the central conductor and g_g stands for the ground planes and $k = S/(S+2W)$. The above expressions are valid also for the superconducting state [16], and have been experimentally verified for identical resonator designs as ours [17]. The fraction of kinetic to total waveguide inductance is

$$\alpha = \frac{L_k}{L_g + L_k} \tag{3.6}$$

In the CPW geometry the resonator is mainly sensitive to the central line and to a lesser degree to the nearby ground plane: $g_c/(g_c+g_g) \approx 1/(1+k)$. For our case, typically $S = 3$ μm, $W = 2$ μm and $t = 100$ nm, leading to values of $L_g = 0.44$ μH/m and $C = 0.16$ nF/m. For a surface impedance of $L_s = 0.1$ pH, a value typical for Nb (low temperature resistivity $\rho \sim 5$ $\mu\Omega$cm, Eqs. 2.18, 2.19), we get $L_k = 45$ nH/m, $g_c/(g_c+g_g) = 0.72$ and $\alpha = 0.09$.

A variation in the kinetic inductance and complex conductivity leads to changes in the resonance frequency, using Eqs. 3.1 and 2.23

$$\frac{\delta\omega_0}{\omega_0} = -\frac{\alpha}{2}\frac{\delta L_k}{L_k} = \frac{\alpha\beta}{4}\frac{\delta\sigma_2}{\sigma_2} \tag{3.7}$$

3.2.2 Coupling

The resonators are coupled capacitively to the feedline near the open end, by running a part of the resonator CPW-line alongside the feedline, while keeping the ground plane uninterrupted. An uninterrupted groundplane is imperative, otherwise the current path on one side of the groundplane differs from the other one, and undesired odd modes can arise due to the phase difference: the return current in both sides of the groundplane is no longer in phase. The quality factor is defined as the energy in the system over the energy lost per cycle

$$Q = \frac{\omega E}{P} \tag{3.8}$$

In our case, the coupler can be seen as a 3 port system: port 1 and port 2 are the left and right side of the feedline (see Fig. 3.1) and port 3 is at the resonator waveguide just under the coupler. Per cycle, i.e. two round-trips along the resonator waveguide, the travelling wave encounters the coupler twice and energy is leaked from port 3 into port 1 and 2: $P = 2fE(|S_{13}|^2 + |S_{23}|^2)$, with S_{13} the scattering matrix element denoting the voltage transmission from port 3 to 1. A quarterwave resonator also accommodates higher order modes: $n\lambda/4$ with $n = 1, 3, 5, 7$ etc. Per cycle the coupler is encountered $2/n$ times. As $S_{13} = S_{23}$, the coupling quality factor is given by

$$Q_c = \frac{n\pi}{2|S_{13}|^2} \tag{3.9}$$

with $n = 1$ for the quarter wavelength mode. The numerical value of S_{13} can be calculated using microwave simulation software, see Ref. [12] for details. Increasing the length or decreasing the distance to the feedline decreases the coupling quality factor.

The quality factor of the *loaded* resonator is given by

$$\frac{1}{Q_l} = \frac{1}{Q_c} + \frac{1}{Q_i} \tag{3.10}$$

with Q_i denoting the internal, or unloaded quality factor. It reflects the losses in the superconductor (Eq. 2.22), in the dielectric, or the radiation losses [12]. The response time of the resonator is given by $\tau_{res} = Q_l/\pi f_0$.

3.3 Microwave perspective on a superconducting resonator

In this section we consider the microwave behaviour of the resonator. We derive the scattering parameters, address the resonance circle, and define the obervables, phase θ and amplitude A, which are used to sense the resonator in the time domain. In addition we consider the power levels inside the resonator. While we focus on quarterwave resonators in this section, the analysis is valid also for both halfwave resonators and higher order modes.

3.3.1 Scattering parameters

In essence, a quarterwave resonator is a piece of transmission line with an open end on one and a shorted end on the other side. Applying the telegraph equation, a transmission line has a characteristic impedance of [18]

$$Z_0 = \sqrt{\frac{R + i\omega L}{G + i\omega C}} \approx \sqrt{\frac{L}{C}} \tag{3.11}$$

with L and C the inductance and capacitance per unit length, and R the distributed resistance of the transmission line and G the conductance of the dielectric, both contributing to the losses. The complex propagation constant is

$$\gamma = \sqrt{(R + i\omega L)(G + i\omega C)} = \alpha + i\beta \tag{3.12}$$

with $\alpha \simeq \frac{1}{2}(R/Z_0 + GZ_0)$ the attenuation constant and $\beta \simeq \omega\sqrt{LC} = \omega/v$, here $v = 1/\sqrt{LC}$ is the phase velocity. The impedance of a *shorted* transmission line resonator (i.e. terminated with a zero load) with characteristic impedance Z_0 is [18]

$$Z_{TLR} = Z_0 \tanh(\gamma l) = Z_0 \frac{1 - i\tanh(\alpha l)\cot(\beta l)}{\tanh(\alpha l) - i\cot(\beta l)} \tag{3.13}$$

The internal quality factor of an unloaded resonator is $Q_i = \frac{\beta}{2\alpha}$. Using $l = \frac{1}{4}\lambda$, near resonance: $\beta l = \frac{\pi}{2}(1 + \frac{\delta\omega}{\omega})$, $\coth(\beta l) \approx -\frac{\pi}{2}\frac{\delta\omega}{\omega}$ and $\tanh(\alpha l) \approx \frac{1}{2Q_i}\frac{\pi}{2}(1 + \frac{\delta\omega}{\omega})$. The unloaded resonator resonates at a frequency $\omega_{1/4}$, which takes both geometry, dielectrics and kinetic inductance into account: $\frac{\delta\omega_{1/4}}{\omega_{1/4}} = \frac{\omega - \omega_{1/4}}{\omega_{1/4}}$. Putting it all together and simplifying results in

$$Z_{TLR} = Z_0 \frac{4Q_i/\pi}{1 + i2Q_i\frac{\delta\omega_{1/4}}{\omega_{1/4}}} = Z_0 \frac{\frac{4Q_i}{\pi} - i\frac{8Q_i^2}{\pi}\frac{\delta\omega_{1/4}}{\omega_{1/4}}}{1 + 4Q_i^2(\frac{\delta\omega_{1/4}}{\omega_{1/4}})^2} \tag{3.14}$$

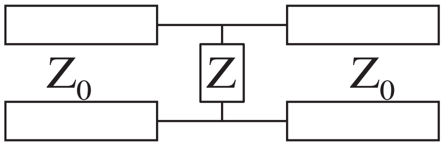

Figure 3.3: Network representation of a resonator. Z_0 denotes the feedline resistance, 50 Ω, and Z is given by Eq. 3.17.

Our resonators are capacitively coupled to the feedline. The impedance of such a *loaded* resonator is

$$Z = \frac{-i}{\omega C} + Z_{TLR} \tag{3.15}$$

with quarterwave resonator coupling quality factor $Q_c = \frac{\pi}{2Z_0^2(\omega C)^2}$ [12]. The total impedance is

$$Z/Z_0 = \frac{\frac{4Q_i}{\pi} - i\frac{8Q_i^2}{\pi}\frac{\delta\omega_{1/4}}{\omega_{1/4}} - i\sqrt{\frac{2Q_c}{\pi}}[1 + 4Q_i^2(\frac{\delta\omega_{1/4}}{\omega_{1/4}})^2]}{1 + 4Q_i^2(\frac{\delta\omega_{1/4}}{\omega_{1/4}})^2} \tag{3.16}$$

at resonance $\mathrm{Im}(Z) = 0$, and the resonance frequency is: $\frac{\delta\omega_{1/4}}{\omega_{1/4}} = -\sqrt{\frac{2}{\pi Q_c}} \ \surd \ 0$. The first solution is the one with small $\mathrm{Re}(Z)$. *Hence the loaded resonator will resonate at another frequency* $\omega_0 \lesssim \omega_{1/4}$. At ω_0 the resonator acts as a short. We redefine the normalised frequency: $\frac{\delta\omega_0}{\omega_0} = \frac{\omega - \omega_0}{\omega_0}$, $\frac{\delta\omega_{1/4}}{\omega_{1/4}} = \frac{\delta\omega_0}{\omega_0} - \sqrt{\frac{2}{\pi Q_c}}$. The impedance of the loaded transmission line resonator near resonance is

$$\frac{Z}{Z_0} = \sqrt{\frac{2Q_c}{\pi}} \frac{2Q_i\frac{\delta\omega_0}{\omega_0} - i}{1 + i2Q_i\frac{\delta\omega_0}{\omega_0} - i2Q_i\sqrt{\frac{2}{\pi Q_c}}} \tag{3.17}$$

The schematic representation of the resonator is depicted in Fig. 3.3. The scattering parameters (S) of such a system are [18]: $S_{21} = S_{12} = \frac{2}{2 + Z_0/Z}$ and $S_{11} = S_{22} = \frac{-Z_0/Z}{2 + Z_0/Z}$. At resonance

$$S_{21}^{min} = \frac{Q_c}{Q_c + Q_i} \qquad S_{11} = \frac{-Q_i}{Q_i + Q_c} \tag{3.18}$$

Near resonance, using Eq. 3.17 and neglecting higher order terms,

$$S_{21} = \frac{S_{21}^{min} + i2Q_l\frac{\delta\omega_0}{\omega_0}}{1 + i2Q_l\frac{\delta\omega_0}{\omega_0}} \tag{3.19}$$

with $Q_l = \frac{Q_iQ_c}{Q_i + Q_c}$ the loaded quality factor. Eq. 3.19 quantifies the voltage transmission coefficient of a travelling wave propagating in the feedline from port

1 to port 2, i.e. left to right in Fig. 3.1. The above equation is valid for any resonator coupled to a feedline, also for lumped-element resonators [11].

Alternatively, the feedline transmission can be derived by considering the travelling waves inside the resonator, just under the coupler, travelling towards the shorted end. The waves leak in from the feedline through the coupler, hence acting as a virtual source $V_1 S_{31}^* e^{-i\omega t}$ (the conjugate of S_{31} as the frames of reference of port 1 and 3 are anti-parallel). Consider a single travelling wave which goes around in the resonator (length l) once, i.e. runs across $\frac{1}{4}\lambda$, gets a 180° phase shift due to the shorted end, runs again across $\frac{1}{4}\lambda$, gets reflected off the coupler; its voltage is multiplied by $S_{33}e^{\gamma 2l}e^{i\pi}$. Hence just under the coupler the travelling waves interfere into

$$V_1 S_{31}^* \sum_{n=0}^{\infty} \left(-S_{33}e^{\gamma 2l}\right)^n = V_1 S_{31}^* \frac{1}{1+S_{33}e^{\gamma 2l}} \tag{3.20}$$

with $S_{13} = i\sqrt{\pi/2Q_c}$ (Eq. 3.9) and $S_{33} = \sqrt{1-\pi/Q_c}$ (50 Ω) ($\angle S_{13}$=+90°, $\angle S_{33}$=0). What leaks into the feedline is given by multiplying the above equation with $S_{23}^* e^{\gamma 2l}e^{i\pi}$, as it travels once more through the resonator and finally through the coupler, resulting in

$$S_{21} = \left(1 - \frac{S_{31}^* S_{23}^* e^{\gamma 2l}}{1+S_{33}e^{\gamma 2l}}\right)^* \tag{3.21}$$

which is identical to Eq. 3.19.

The feedline transmission of a Ta resonator at five temperatures between 350 mK and 1 K is shown in Fig. 3.4a. The resonator gives rise to a dip in the magnitude and characteristic signature in the phase near the resonance frequency, tracing a resonance circle in the complex plane (inset) when sweeping the probing frequency. With increasing temperature the resonance frequency shifts to lower frequencies and the dips in the magnitude become shallower due to the decrease in quality factor, leading to a decrease of the radius of the resonance circle and shift of its origin in the complex plane.

3.3.2 Phase, amplitude and the resonance circle

The resonance circle traced by the feedline transmission is shown in the inset of Fig. 3.4a, lying in the half of the complex plane with the positive real axis. Its midpoint lies on the real axis at $x_c = (1+S_{21}^{min})/2$, its radius is $r = (1 - S_{21}^{min})/2 = 1 - x_c = Q_l/2Q_c$. We sense the transmission at the equilibrium resonance frequency ω_0. A change in resonance frequency or quality factor leads to a change in the transmission, as illustrated by the open circles. The resonance

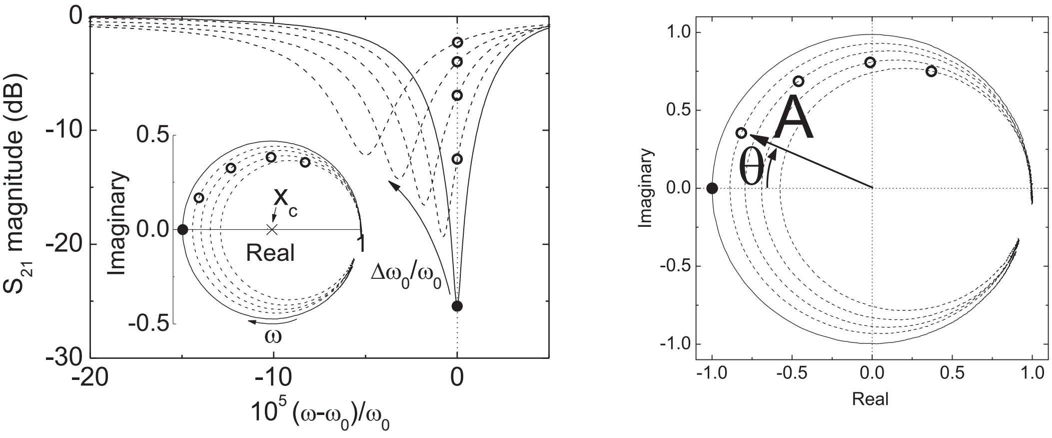

(a) (b)

Figure 3.4: (a) The magnitude of the feedline transmission S_{21} near the resonance frequency of a 150 nm thick Ta resonator for five different temperatures. The inset shows the same feedline transmission in the complex plane. The resonance circle at equilibrium conditions, taken as reference, is denoted by x_c. The transmission at the equilibrium resonance frequency is depicted by the open circles, tracing a round path (the 'quasiparticle trajectory') in the complex plane with x_c as the center. This quasiparticle trajectory is followed upon optical excitation. The angle between this path and the imaginary axis, when it intersects the real axis, is given by: $\tan(\psi) = -\frac{Q_i}{Q_i+Q_c}\frac{\delta\sigma_1}{\delta\sigma_2}$. (b) The resonance circles normalised to the reference resonance circle and the observables: phase θ and amplitude A. The response to an optical pulse of this Ta resonator is shown in Fig. 5.1.

circle at *equilibrium* conditions is taken as reference, with x_c fixed: we shift the resonance circle to the origin and give it unity radius, see Fig. 3.4b. A change in the feedline transmission appears as a variation in phase θ and amplitude A:

$$\tan(\theta) = \frac{\mathrm{Im}(S_{21})}{x_c - \mathrm{Re}(S_{21})} \tag{3.22}$$

$$A = \frac{\sqrt{[\mathrm{Re}(S_{21}) - x_c]^2 + \mathrm{Im}(S_{21})^2}}{1 - x_c} \tag{3.23}$$

To first order, near the equilibrium resonance frequency ω_0, using $\tan(\theta) \approx \theta$,

$$\theta = -\frac{2Q_l\frac{\delta\omega_0}{\omega_0}(1 - S_{21}^{min})}{x_c - S_{21}^{min}} = -4Q_l\frac{\delta\omega_0}{\omega_0} \tag{3.24}$$

$$\delta A = -\frac{\delta\mathrm{Re}(S_{21})}{1 - x_c} = -\frac{\delta S_{21}^{min}}{1 - x_c} = \frac{2Q_c}{Q_i + Q_c}\frac{\delta Q_i}{Q_i} \tag{3.25}$$

where for θ the minus sign arises from the fact that under operation the resonator is continuously probed at the equilibrium value of ω_0, and the path in the complex plane for decreasing resonance frequency is opposite to the the path for increasing probing frequency ω. When only the complex conductivity is concerned, using Eqs. 2.23 and 3.7, θ and A become

$$\theta = -\alpha\beta Q_l \frac{\delta\sigma_2}{\sigma_2} \tag{3.26}$$

$$A = 1 - 2\frac{Q_l}{Q_i}\left(\frac{\delta\sigma_1}{\sigma_1} - \frac{\delta\sigma_2}{\sigma_2}\right). \tag{3.27}$$

Accordingly, both θ and A are probes for the complex conductivity. The choice for θ and A as observables allows for easily comparing different resonators due to the normalisation. Additionally, the contribution of the system to the on and off resonance noise is identical in both cases.

3.3.3 Probing signal power

Here we derive the power as well as the electric field strength at resonance. Suppose we have a 3 port network, port 1 is input, port 2 is output and port 3 is just under the resonator coupler, see Fig. 3.1. A travelling wave with amplitude V_1 travels from 1 to 2, and undergoes destructive interference, as such that at port 2 the amplitude is only $V_1 S_{21}$. The travelling wave from the resonator travelling towards the coupler has amplitude V_3. The decrease in V_1 is largely due to the signal travelling from port 3 to 2 ($V_3 S_{23}$), being exactly out of phase, and to a smaller degree due to part of the signal travelling from port 1 to port 3 ($V_1 S_{31}$). Hence,

$$V_1 S_{21} = V_1(1 - S_{31}) - V_3 S_{23} \tag{3.28}$$

$$\frac{V_3}{V_1} = \frac{Q_l}{Q_c}\sqrt{\frac{2Q_c}{\pi}} - 1 \tag{3.29}$$

$$\frac{P_{internal}}{P_{readout}} = \frac{V_3^2/Z_{resonator}}{V_1^2/Z_{feedline}} \cong \frac{2}{\pi}\frac{Q_l^2}{Q_c}\frac{Z_{feedline}}{Z_{resonator}} \tag{3.30}$$

with $P_{internal}$ the power of the travelling wave inside the resonator (not the standing wave) and for the same transmission line impedance. The forward and backward travelling wave interfere into a standing wave which has an amplitude of $V_r = 2V_3$ (root mean square voltage). Typically for the characteristic impedance: $Z_{resonator} = Z_{feedline} = 50\ \Omega$.

The energy inside is

$$2\int_0^l \frac{1}{2}C\left[V_r \sin\left(\frac{2\pi}{4l}x\right)\right]^2 dx = \frac{1}{2}CV_r^2 l \tag{3.31}$$

with C the capacitance per unit length of the CPW. The factor 2 in front is because the same amount of energy resides in the inductance at resonance. To give an example: consider applying -90 dBm in the feedline, i.e. 1 pW readout power, to a resonator on a Si substrate ($\epsilon_{substrate} = 11.9$) with $Q_i = 10^6$, $Q_c = 10^5$, $f_{res} = 10$ GHz, $l = 2.95$ mm, with a central line width of 3 μm and gap width of 2 μm, giving $C = 165$ pF/m (Eq. 3.3). The internal resonator power becomes $P_{internal}$=-43 dBm, giving $V_3 = 1.6$ mV ($P_{internal} = V_3^2/Z_{resonator}$), and $V_r = 3.2$ mV. The electric field strength results in $E = 1.6$ kV/m near the open end. The energy inside the resonator is 2.6 aJ, equal to $3.9 \cdot 10^5$ photons.

3.4 Sample fabrication

Fabrication starts with the deposition of a superconducting film on a cleaned Si or sapphire wafer. In general, we use (100)-oriented Si (purchased from Topsil Semiconductor Materials A/S) with a room temperature resistivity in excess of 1 kΩcm or in excess of 10 kΩcm. Prior to deposition, the wafer is dipped into HF to remove the native oxide and passivate the dangling bonds on the Si surface with hydrogen. We believe the oxide to be detrimental to the resonator properties, hence this step is crucial: silicon oxide is known to contain many defects [19], giving rising to possible electron trapping states [20] as well as dipole two-level systems [21]. Additionally, the dangling bonds in the Si/SiO$_2$ interface have been suggested to lead to flux noise in Josephson flux qubits [22]. The sapphire (from UniversityWafers.com) used for the samples described in this thesis is A-plane oriented.

The superconducting resonators used in this thesis are made of Al, Ta, Nb or NbTiN. The Nb and NbTiN films have been DC sputter deposited in the Nordiko sputtering system at Delft University of Technology. The Nb has also been used as counterelectrodes in the superconductor-insulator-superconductor (SIS) junctions fabricated in our group, and the NbTiN has been used as part of the tuning structure in Nb SIS junctions for HIFI band 3 and 4 of the Herschel space-based observatory [23]. Patterning is done using photolithography and reactive ion etching in a SF$_6$/O$_2$ plasma, using laser endpoint detection to avoid overetching of the substrate. The Ta and Al samples are fabricated in the SRON cleanroom in Utrecht. For the Ta samples used, prior to Ta DC sputter deposition, a 6 nm Nb seed layer is deposited in situ to promote the growth of the desired body-centered-cubic crystal orientation [24]. Subsequently the film is patterned using photolithography and CF$_4$/O$_2$ reactive ion etching. The Al is evaporated or sputtered and is patterned using photolithography and wet etching in a solution of phosphoric acid, acetic acid and nitric acid. After fabrication the samples are covered with a poly(methyl methacrylate) (PMMA) layer to protect them during dicing, this layer is removed prior to measuring.

A wafer contains chips with resonators as well as chips with DC test devices. The chips with resonators have dimensions of 20x4 mm, and typically contain around 30-50 resonators. The DC test devices, with strips with varying widths, are used to ascertain the DC properties of the film, i.e. the critical temperature, resistivity and residual resistance ratio.

3.5 Measurement techniques

To reduce the density of quasiparticle excitations, for reaching high quality factors and long relaxation times for photon detection, the samples need to be cooled to below a tenth of the critical temperature; at temperatures between several tens and hundreds of millikelvin. At the same time frequencies up to 10 GHz are used, where impedance matching is not trivial. Care has to be taken to ensure thermalisation of the cables while keeping the reflections to a minimum; microwave and cryogenics are interwoven in the setup. The readout is done using a signal generator, low noise amplifier, quadrature mixer and digitiser. The quadrature mixer needs to be calibrated carefully. Additionally, possible ground loops result in large spikes in the noise spectra. The unforgiving combination of high frequencies, low temperatures and quadrature mixing makes a reliable, low noise measurement setup a key ingredient.

3.5.1 Cryostat

We use a two-stage He-3 sorption cooler [25] inside a liquid He cryostat to reach a base temperature of 310 mK. Inside the sorption cooler a porous material (the sorption pump) releases He-3 when heated to about 40 K. The He-3 gas subsequently liquefies as it passes a condenser, in contact with a pumped He-4 bath (the second stage), and trickles down onto the sample stage. When the sorption pump is no longer heated it starts to absorb the He-3 and decrease the vapour pressure. The sample stage is cooled by evaporative cooling. The sample box is mounted on top of the He-3 sorption cooler, see Fig. 3.5. The samples are glued into the sample box using GE varnish. Several sample box lids are coated on the inside with a mixture of stycast and 1 mm SiC grains to form a blackbody [26] in order to absorb stray photons entering the sample box. We find that the amplitude of the response to optical pulses is reduced by over 90 % when using coated lids, indicating their effectiveness. We find no effect on the

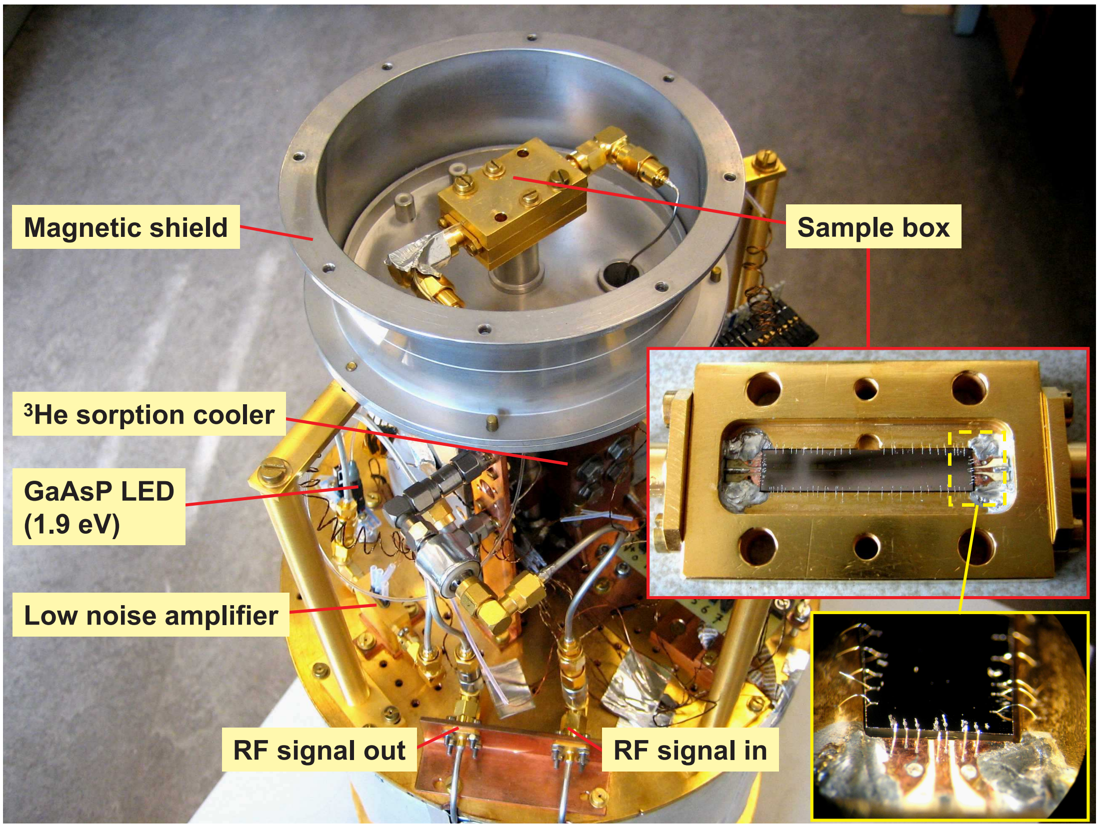

Figure 3.5: The cryostat used in Delft, showing the 4.2 K cold plate, the He-3 sorption cooler, magnetic shield, sample box, RF cabling, low noise cryogenic amplifier, LED for providing optical pulses and the wiring of temperature sensors and heaters. The RF cabling outer conductor is thermally anchored four times on to 4.2 K: twice when entering the 4.2 K space and twice by anchoring one side of the CuNi SMA cables connecting to the sample box. The sample chip is glued into the sample box and electrically connected by wire-bonding (upper and lower insets).

relaxation time, indicating stray radiation does not play a role (experiments with Al in Utrecht need additional gaskets, filtering and silver taping of the sample box, as Al is more sensitive and has a lower gap [27]). The sample space is surround by a superconducting magnetic shield, made from copper clad with a Pb/Sn alloy. We use a gold-plated copper sample box (gold directly over copper) with two microwave launchers on both sides with SMA connectors, see insets Fig. 3.5. The SMA launcher is connected to a transition board. This board forms the transition between the SMA launcher and the feedline on the sample chip. It transforms the waveguide from the SMA launcher to a microstrip, consisting of a central top wire and bottom groundplane. The launcher's central pin is soldered onto the copper top wire. Subsequently the waveguide is transformed from a microstrip to an ungrounded CPW. Here, electrical connection is made from the transition board to the feedline of the sample chip by means of ultrasonic wirebonding using 25 μm wide Al-Si (1 % Si) wires, see insets of Fig. 3.5. For this purpose, the feedline is widened to a central strip width of 400 μm and gap widths of 220 μm; due to the large gap width the electric fields protrude underneath the substrate, therefore underneath these widened feedline sections the metal of the sample box is removed. Additional bond wires are placed at all sides to have a well-defined ground. This avoids spurious resonances as well as possible odd CPW propagation modes, by electrically joining the two groundplanes on the chip, separated by the feedline, into a single groundplane.

The cryostat is shown in Fig. 3.5. The sample box is connected via 15 cm long 0.86 mm diameter CuNi SMA cables to the low noise amplifier (LNA) as well as the attenuator, both firmly thermally anchored to the 4.2 K cold plate. The choice for thin CuNi cabling is threefold: First, the CuNi has a high resistivity at low temperatures and the cables are very narrow, reducing the thermal load on the sample box. Second, blackbody photons coming down the SMA cabling (the Planck peak at 4.2 K lies at 247 GHz) are efficiently attenuated in the CuNi SMA cables. Their narrowness ensures that the intended TEM mode is sustained at much higher frequencies, their resistivity ensures that these frequencies are strongly attenuated [28]. Third, at the GHz frequencies we are interested in the attenuation of these cables is roughly 2-3 dB, hence possible reflections are reduced by roughly 4-6 dB. The CuNi SMA cables connect the sample box to a 20 dB thermally anchored attenuator on one side and to the low noise amplifier on the other side. On the 4.2 K plate RF connections from and to the low noise amplifier are made with 2.2 mm wide Al SMA cables; a 2.2 mm wide stainless steel SMA cable is used just after where the RF signal enters the 4.2 K space ("RF signal in" in Fig. 3.5). The RF signal between the cold plate and room temperature is carried by 2.2 mm wide stainless steel SMA cables. The RF cabling outer conductor is firmly thermally anchored to the 4.2 K stage four times (see Fig. 3.5) and two times to the 77 K stage. Additionally the low noise amplifier is a firm thermal anchor.

Optical pulses, for measuring relaxation times, are generated by a GaAsP LED (bandgap is 1.9 eV) at the 4.2 K cold plate, which is fibre-optically coupled to the sample box. The voltage pulse over the LED and a resistor in series is provided by a home-built computer-linked pulser module, consisting of a programmable microcontroller (Atmel ATtiny2313) and circuitry, placed on the liquid nitrogen stage. The duration of the optical pulse can be set and the intensity of the optical pulse can be varied by choosing the resistor. The circuit includes five resistors for this purpose and corresponding metal-oxide-semiconductor FETs to be able to switch the intensity during measurements. As both the voltage rise and decay time over the LED is approximately 10 ns and the response time of the LED itself is 10 ns, the rise and decay time of the optical pulse is expected to be close to 10 ns. The pulser module provides an optional trigger output for synchronising with the digitiser.

Measurements on Al resonators have been done in Utrecht using an adiabatic demagnetisation refrigerator (ADR) to reach a bath temperature of 30 mK. The ADR is mounted inside a dry cryostat (pulse tube cooler), capable of reaching a cold plate temperature of 3 K. The ADR consists of a ferric ammonium alum (FAA) salt pill and a gadolinium gallium garnet (GGG) crystal, surrounded by superconducting wiring to reach a magnetic field strength up to 6 T in order to magnetise the salt pill and crystal. Cooling occurs when the magnetic spins are aligned and the magnetic field is turned off: the spin orientation starts to randomise, increasing the entropy and hence decreasing the temperature. The FAA pill reaches 30 mK and the GGG crystal reaches 700 mK at negligible remaining magnetic field. At 100 mK FAA temperature the system has a hold time of 48 hours; this hold time is with one pair of NbTi coaxial cables connected to the sample box. Due to the high (but localised) magnetic fields an outer cryoperm as well as an inner superconducting magnetic shield are used. Apart from the cooling mechanism, the RF cabling inside the cryostat and the RF setup in general is very similar to the setup in Delft.

3.5.2 RF setup

A schematic overview of both the cryogenic and warm RF setup is shown in Fig. 3.6. The signal generator (Agilent E8257D) provides the microwave signal, which is split in two parts: one goes into the LO port of the quadrature mixer (Miteq IR0208LC2Q), the other one travels down to the cryostat. In the cryostat, the signal travels through attenuators and a double DC block: these thermalise the cabling as well as prevent thermal radiation from room temperature entering the sample box. An attenuation of 30 dB is chosen to suppress room temperature thermal radiation down to negligible levels. Additionally, inside the attenuators there is a galvanic connection between the inner and outer conductor, allowing for thermalising the inner cable. The double DC blocks galvanically disconnect both the inner and outer conductors, reducing the thermal conductivity.

After travelling through the sample box the signal is amplified using a low noise 4-12 GHz amplifier at the cold plate (CITCRYO4-12A) and a second amplifier (Miteq AFS5 0.1-8 GHz amplifier) at room temperature. The attenuator between these amplifiers is for thermalising the inner cable and reducing stand-

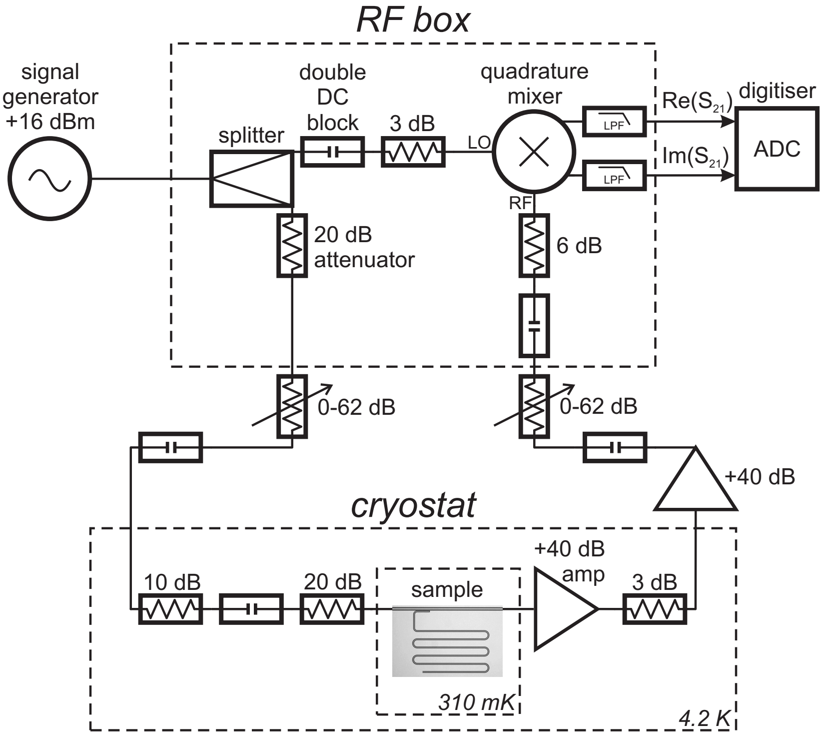

Figure 3.6: The RF circuit. The signal generator provides the microwave signal which travels down the cryostat through the sample feedline, subsequently it is amplified and mixed with a copy of the original signal in the quadrature mixer, forming a homodyne detection scheme. Quadrature mixing is discussed in section 3.5.3. The double DC blocks on the outside of the cryostat are for preventing ground loops.

ing waves. Subsequently it is mixed in a quadrature mixer, whose outputs are acquired in a 2 channel digitiser with self-adjusting anti-aliasing filter (National Instruments PXI-5922). The quadrature mixer requires a constant level of LO power, consequently the signal generator power level is kept constant. Power dependent measurements are performed by adjusting the variable attenuators, provided by a two channel step attenuator (Aeroflex/Weinschel 8310).

To determine the feedline transmission we need to correct for the frequency-dependent transmission coefficients of the other elements in the RF chain: the cabling, microwave amplifiers, and quadrature mixer. To this end, we warm up the sample to about 80 % of T_c, where the resonance frequencies shift to lower values and the resonance dips become very shallow because the quality factor decreases (see Fig. 2.11). The transmission at this temperature is taken as reference. When cooling down, the resonance features appear, calibrated for the other elements in the RF chain.

The temperature of the sample box is controlled under 4.2 K by varying the temperature of the He-3 sorption pump in the sorption cooler. Above 4.2 K a resistor connected to the sample stage allows for direct heating.

3.5.3 Quadrature mixing

In order to sense the feedline transmission in the time domain we use a homodyne detection scheme. The signals (the LO and RF input to the mixer) have identical frequency, the information we want is stored in the phase difference and amplitude of these signals. A standard mixer is insufficient: for example, if the signals would be out of phase or if the amplitude is zero, the output of a standard mixer is in both cases zero. A quadrature mixer, or IQ mixer, consists of two separate mixers and a 90 degree phase shifter. In the first mixer the local oscillator (LO) and RF signal are mixed, giving the in-phase component, I, as in a standard mixer. The quadrature component, Q (not to be mistaken for the quality factor), arises from mixing the LO signal with the RF signal which is now shifted 90 degrees. This mixing scheme allows for reconstructing the complex transmission: the in-phase component is proportional to the real part of the transmission and the quadrature component is proportional to the imaginary part.

A nonideal quadrature mixer suffers from phase imbalance (phase shifter is not exactly 90 degrees), gain imbalance (both mixers have different gain) and DC offsets. Calibrating can be done by applying a LO and RF signal from two frequency locked signal generators, with a constant difference frequency of say, 100 kHz. The raw I and Q output are then

$$I_{raw} = I_{DC} + G_I \cdot r\cos(\phi) \tag{3.32}$$

$$Q_{raw} = Q_{DC} + G_Q \cdot r\sin(\phi + \delta\phi) \tag{3.33}$$

with $\phi = \omega t$, I_{DC} and Q_{DC} the DC offset, G_I and G_Q the gain of the I and Q channel respectively, G_I/G_Q denoting the gain imbalance, and $\delta\phi$ the phase imbalance. The DC offsets, gain imbalance and phase imbalance for the quadrature mixer used (Miteq IR0208LC2Q) are shown in Fig. 3.7. The phase imbalance of this mixer reaches up to 10 degrees at 3 GHz and is even worse above 8 GHz to give an example. A 10 degrees phase imbalance, if not corrected for, gives an I to Q crosstalk of -15 dB ($10\log_{10}\{\sin^2[\delta\phi]\}$), while typically the phase noise (Q to first order) is about 20-30 dB higher than the amplitude noise (I to first order), showing that calibrating the quadrature mixer is extremely important.

The raw data are corrected: First, by subtracting the DC offsets. Second, by multiplying Q with G_I/G_Q. Third, by correcting for the phase imbalance: redefining $I = r\cos(\phi)$ and $Q = r\sin(\phi + \delta\phi)$, corrected now for the DC offsets

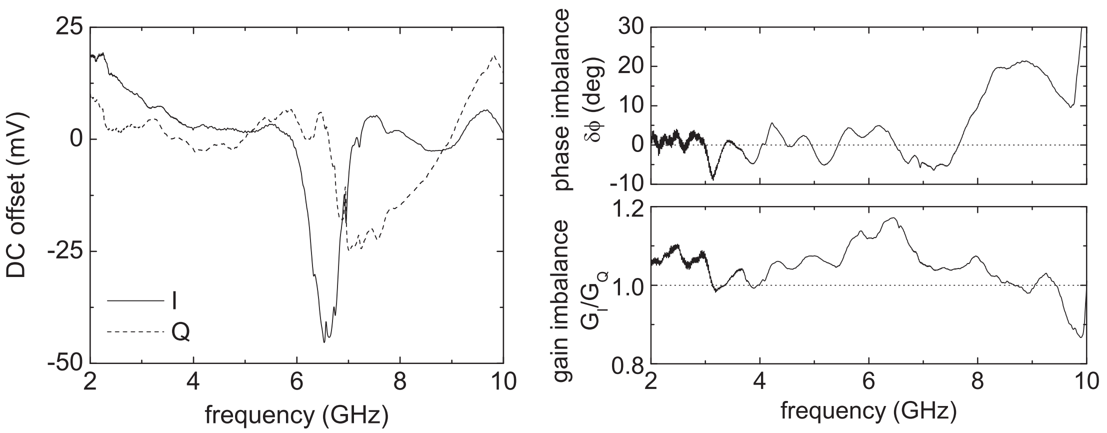

Figure 3.7: DC offsets (left) and the gain and phase imbalances (right) of the Miteq IR0208LC2Q quadrature mixer used in Delft.

and gain imbalance, the procedure to correct for the phase imbalance is

$$
\begin{aligned}
\phi &= \arctan(Q - I\sin(\delta\phi), I\cos(\delta\phi)) \\
r^2 &= \frac{I^2 + Q^2}{\cos^2(\phi) + \sin^2(\phi + \delta\phi)} \\
I_{cal} &= r\cos(\phi) \\
Q_{cal} &= r\sin(\phi)
\end{aligned}
\tag{3.34}
$$

with $\delta\phi$ known from the calibration procedure and $\arctan(y, x)$ valid in all quadrants.

Additionally, the quadrature mixer has a mediocre matching and LO to RF isolation. Typically, the mixer is driven with a +10 dBm signal on the LO input, and the RF signal is -10 dBm. The LO to RF isolation is specified at 20 dB, hence an undesired signal is exiting the RF input port with nearly equal strength as the desired RF signal. This undesired signal can interfere and appear as DC offset, depending on the reflection coefficient (S_{22}) of the output port of the second variable attenuator. This is impossible to calibrate for, as changing the setting of the variable attenuator changes the phase of the reflection coefficient and therefore the interference, leading to a different DC offset. To enhance the matching (the S_{11} of the mixer at optimal conditions is as high as -6 dB) and, more importantly, to decrease the effect of the mediocre LO-RF isolation a considerable attenuator at the RF input of the quadrature mixer is necessary. Moreover, to remove undesired effects of ground loops double DC blocks at the LO and RF input are used, connecting the mixer galvanically only to the digitiser. Additionally, the effects of the mediocre LO to I and Q port isolation, the LO to IF isolation is 20 dB as well, are removed by placing lowpass filters with a cutoff at 1.5 GHz at the I and Q output. The connection from the mixer output to the digitiser is made using a twisted pair of coaxial cables. For our case, the combination of these steps leads to a reduction of the noise spikes to a level comparable to or under the noise floor of the setup, i.e. effectively removing nearly all spikes in the noise spectra.

3.5.4 Setup noise analysis

In this section the setup noise is discussed. After introducing the noise temperature, we focus on the noise for our case. Relevant expressions for the phase and amplitude noise are given. Lastly, we find that they are in good agreement with the data.

Noise temperature

The root mean square (RMS) voltage noise over a resistor due to thermal noise at a temperature T is in the Rayleigh-Jeans limit ($hf \ll kT$, the GHz frequencies under consideration are far below the Planck peak) given by:

$$V_N = \sqrt{4kTR}\sqrt{B} \tag{3.35}$$

which corresponds to 0.9 nV/Hz$^{1/2}$ at room temperature for a 50 Ω resistor; B is the bandwidth. We now consider its Thévenin equivalent, a voltage source V_N in series with source impedance R, which is now connected to a load resistance R_L. The power dissipated in the load P_L is

$$P_L = \frac{V_L^2}{R_L} = V_N^2 \frac{R_L}{(R_L + R)^2} = 4kTB\frac{R_L R}{(R_L + R)^2} \tag{3.36}$$

Maximum power transfer occurs for $R_L = R$, and the power *per unit bandwidth* dissipated in the load is

$$P_L = kT \text{ for } R_L = R \tag{3.37}$$

As in our RF system nearly all the components are matched to 50 Ω we can simply express the noise power per unit bandwidth as kT.

An amplifier with gain G and input noise power P_N produces an output power P_{out} if an input power P_{in} is supplied of $P_{out} = G \cdot (P_{in} + P_N)$ which in the Rayleigh-Jeans limit can be rewritten as

$$P_{out} = G \cdot (P_{in} + kT_N) \tag{3.38}$$

with T_N the amplifier input noise temperature. The noise level kT_N indicates the *noise power per unit bandwidth at the input.* For an attenuator with gain $G < 1$ and a power P_{in} at its input the output power is given by:

$$P_{out} = GP_{in} + (1 - G) \cdot kT_a \tag{3.39}$$

with T_a the physical temperature of the attenuator. The input noise temperature of the attenuator is given by $T_N = T_a(1 - G)/G$. Hence for an attenuator with $G \ll 1$, the *output* noise power per unit bandwidth is given by its physical temperature.

A series combination of n elements in the chain results in a system gain of $G = \prod_{j=1}^{n} G_j$ (cartesian) and a noise temperature of

$$T_N = T_1 + \sum_{i=2}^{n} \left[\frac{T_i}{\prod_{j=1}^{i-1} G_j} \right] = T_1 + \frac{T_2}{G_1} + \frac{T_3}{G_1 G_2} + ... \tag{3.40}$$

Our system

For our system, the RF setup is mainly noise limited by the noise sources close to the sample: the first amplifier and the attenuator in front of the sample box. At the input of the sample box the noise is mainly due to the physical temperature of the last attenuator, 4.2 K, and to a lesser degree due to the 300 K thermal radiation attenuated by 30 dB, adding 0.3 K. At the output of the sample box the noise temperature is dominated by the low noise amplifier. We use a 4-12 GHz high electron mobility transistor amplifier (CITCRYO4-12A) [13], with an input noise temperature of $T_N \approx 3-5$ K and a gain of $\sim$ 40 dB. Due to this high gain, the noise temperature of the second amplifier (Miteq AFS5-00100800-14-10P-5, $T_N = 110$ K) hardly matters. *The input noise temperature of our system is typically* $T_N \approx 9K$, if the gain between the sample box output and the mixer input is kept above 60 dB, due to the noise contribution from the digitiser (see below). This implies a readout power of under -70 dBm, as the RF input power at the quadrature mixer lies around -10 dBm. As we use a homodyne detection scheme, mixing two signals of the exact same frequency, the frequency noise of the signal generator is essentially negated. Only at frequencies above several 100 MHz in the noise spectrum, well above the range we are interested in (1 Hz - 100 kHz) signal generator frequency noise can appear due to the RF cabling length.

After amplification the signal is mixed and subsequently digitised. An n-bit digitiser has quantisation noise, yielding a signal to noise ratio of $SNR = 20\log_{10}(2^n)$, i.e. $\sim 6.0n$ in dB, resulting in 144 dB for a 24 bit and 96 dB for a 16 bit digitiser. For our 24 bit digitiser (National Instruments PXI-5922) the noise density floor is -170 dBFS/Hz (dB Full Scale), in agreement with the $3.4\mu V$ RMS voltage noise specification at 50 kSample/s at ±5 V input range: $(V_{rms}/V_{range})^2 \cdot B^{-1}$ = -170 dBFS/Hz, reducing the accuracy of the digitiser to effectively 20.5 bits. This corresponds to a voltage noise density of 15 nV/Hz$^{1/2}$, which can be converted to a noise temperature of $T_N = 10^5$ K (Eq. 3.35) using R=50 Ω. The value $R = 50\ \Omega$ is taken since this is the RF chain characteristic impedance, the digitiser impedance is not matched (1 MΩ). Referred to the quadrature mixer input (conversion gain of ∼ -10 dB), the noise of the digitiser (now on the order of 10^6 K) exceeds that of the mixer ($T_N \sim 2 \cdot 10^3$ K). Additionally, both the digitiser and the quadrature mixer have a significant $1/f$ slope at low frequencies in the noise spectrum. We find that the $1/f$ noise levels at the output of the mixer and at the input of the digitiser are very comparable, differing by only 2 dB.

We now convert the single side band (SSB) noise temperature of the system into a double side band (DSB) phase noise. The power spectral density of an arbitrary function, such as a voltage $V(t)$ is the Fourier transform of the auto-correlation function, $S_V = 2\mathscr{F}\{< V(t)V(0) >\}$, see Eq. 2.8. We now treat noise *power.* The absolute SSB power spectral density of the power in a system with voltage fluctuations over a resistance R is: $S_P^{SSB,abs} = S_V^{SSB,abs}(f)/R$, with S_V in V^2/Hz. In case we use a mixer to determine these around frequency f_0, we cannot discern between $S_V(f_0 + f)$ and $S_V(f_0 - f)$. Usually these are equal, and we only need to consider the DSB noise. However, amplifier noise temperatures are given in SSB. Defining the DSB relative noise power spectral density using the SSB input noise temperature T

$$S_P^{DSB,rel} = \frac{S_V^{DSB,abs}/R}{< V^2 > /R} = \frac{2kT^{SSB}}{P_{in}} \tag{3.41}$$

with S_P in dimension 1/Hz and P_{in} the input power. *The value kT reflects the absolute noise power per unit bandwidth at the input.*

With a complex signal, such as the feedline transmission, half the additive system noise power is in the real ($I = \mathrm{Re}(S_{21})$) and half is in the imaginary ($Q = \mathrm{Im}(S_{21})$) direction as these are two orthonormal variables,

$$S_I^{DSB,rel} = S_Q^{DSB,rel} = \frac{kT^{SSB}}{P_{in}} \tag{3.42}$$

We now reformulate the noise in S_{21} into noise in phase θ and amplitude A with respect to the resonance circle. Consider the polar plane with the resonance circle with radius $r = Q_l/2Q_c$, see Fig. 3.4a. Off resonance, for the phase: $\tan\theta = \delta Q/r$, so $S_\theta = S_Q/r^2$. For the amplitude: $A = |I - x_c|/r$, so $S_A = S_I/r^2$.

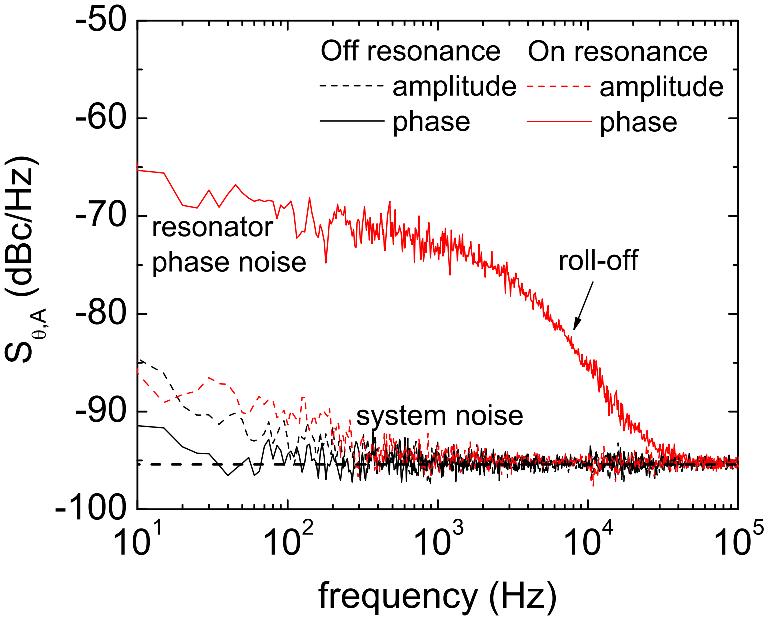

Figure 3.8: The noise power spectral density of the phase θ and amplitude A for a 300 nm thick NbTiN resonator; it is the same resonator used in Fig. 7.3 to describe the frequency noise of uncovered NbTiN resonators. Readout power: $P_{readout}$=-81 dBm, $S_{21}^{min} = 0.55$, $r = 0.23$. On resonance a large amount of phase noise appears, rolling off at a frequency reciprocal to the resonator response time. The noise off resonance gives the system noise which lies very close to the expected system noise level at -95.4 dBc/Hz (Eq. 3.43) (dashed horizontal line).

For the power: $P_{in} = P_{readout}$. On resonance the system noise level is the same, i.e. noise in I or Q leads to a similar noise level in A and θ both on and off resonance due to our choice of x_c. Hence, for both on and off resonance the system noise is given by

$$S_{\theta,A}^{DSB,rel} = \frac{kT}{r^2 P_{readout}} \tag{3.43}$$

For resonators with a high internal and low coupling quality factor, $Q_i \gg Q_c$, which show a very deep dip in the magnitude of the feedline transmission (see Fig. 3.4a): $r \to \frac{1}{2}$.

To illustrate the strength of the above analysis we show in Fig. 3.8 the phase and amplitude noise data of a resonator made from a 300 nm thick NbTiN film. This exact same resonator is used in Figs. 7.2 and 7.3 to show the temperature dependence of the resonance frequency as well as the frequency noise of uncovered NbTiN resonators when comparing with various dielectric layers in Chapter 7. Both off resonance, here the transmission is probed far away from the resonance frequency giving the system noise, and on resonance, probing the transmission at ω_0 giving the noise generated by the resonator, are shown. For this resonator: $r = 0.23$, and the applied readout power in the feedline in the sample chip is -81 dBm. At 4.4 GHz, the resonance frequency, the CuNi SMA cables attenuate 2.0 dB, the LNA noise temperature is 2.7 K, and together with 4.5 K thermal radiation from the attenuators this combines into a 8.8 K system noise temperature at this frequency. With a SSB system noise temperature of 8.8 K we get a system phase and amplitude noise level of $S_{\theta,A} =$ -95.4 dBc/Hz (dBc: dB relative to the carrier signal). This system noise level is what we find (Fig. 3.8). The large amount of phase noise which is being generated by the resonator, also indicated by the roll-off, is described in detail in Chapters 7 and 8. The increase in mainly amplitude noise, both on and off resonance, at lower frequencies in the spectrum is attributed to the amplitude noise of the low noise cryogenic amplifier.

References

[1] P. K. Day, H. G. LeDuc, B. A. Mazin, A. Vayonakis, and J. Zmuidzinas, *A broadband superconducting detector suitable for use in large arrays*, Nature **425**, 817 (2003).

[2] J. J. A. Baselmans, S. J. C. Yates, R. Barends, Y. J. Y. Lankwarden, J. R. Gao, H. F. C. Hoevers, and T. M. Klapwijk, *Noise and sensitivity of aluminum kinetic inductance detectors for sub-mm astronomy*, J. Low Temp. Phys. **151**, 524 (2008).

[3] G. Vardulakis, S. Withington, D. J. Goldie and D. M. Glowacka, *Superconducting kinetic inductance detectors for astrophysics*, Meas. Sci. Technol. **19**, 015509 (2008).

[4] G. Hammer, S. Wünsch, M. Rösch, K. Ilin, E. Crocoll and M. Siegel, *Superconducting coplanar waveguide resonators for detector applications*, Supercond. Sci. Technol. **20**, S408 (2007).

[5] A. Wallraff, D. I. Schuster, A. Blais, L. Frunzio, R. S. Huang, J. Majer, S. Kumar, S. M. Girvin, and R. J. Schoelkopf, *Strong coupling of a single photon to a superconducting qubit using circuit quantum electrodynamics*, Nature **431**, 162 (2004).

[6] M. Sandberg, C. M. Wilson, F. Persson, T. Bauch, G. Johansson, V. Shumeiko, T. Duty, and P. Delsing, *Tuning the field in a microwave resonator faster than the photon lifetime* , Appl. Phys. Lett. 92, 203501 (2008).

[7] G. J. Grabovskij, L. J. Swenson, O. Buisson, C. Hoffmann, A. Monfardini, and J. C. Villégier, *In situ measurement of the permittivity of helium using microwave NbN resonators*, Appl. Phys. Lett. **93**, 134102 (2008).

[8] C. A. Regal, J. D. Teufel, and K. W. Lehnert, *Measuring nanomechanical motion with a microwave cavity interferometer*, Nature Physics **4**, 555 (2008).

[9] M. A. Castellanos-Beltran and K. W. Lehnert, *Widely tunable parametric amplifier based on a superconducting quantum interference device array resonator*, Appl. Phys. Lett. 91, 083509 (2007).

[10] K. W. Lehnert, K. D. Irwin, M. A. Castellanos-Beltran, J. A. B. Mates, and L. R. Vale, *Evaluation of a microwave SQUID multiplexer prototype*, IEEE Trans. Appl. Sup. **17**, 705 (2007).

[11] S. Doyle, P. Mauskopf, J. Naylon, A. Porch, and C. Duncombe, *Lumped element kinetic inductance detectors*, J. Low Temp. Phys. **151**, 530 (2008); S. Doyle, *Lumped element kinetic inductance detectors*, Ph. D. Thesis, Cardiff University (2008).

[12] B. A. Mazin, *Microwave kinetic inductance detectors*, Ph. D. Thesis, California Institute of Technology (2004).

[13] N. Wadefalk *et al.*, *Cryogenic wide-band ultra-low-noise IF amplifiers operating at ultra-low DC power*, IEEE Trans. on Micr. Theory and Tech. **51**, 1705 (2003).

[14] R. E. Collin, *Foundations for Microwave Engineering*, (McGraw-Hill, New York, 1992).

[15] R. N. Simons, *Coplanar waveguide circuits, components and systems*, (John Wiley and Sons, 2001).

[16] J. C. Booth and C. L. Holloway, *Conductor loss in superconducting planar structures: Calculations and measurements*, IEEE Trans. on Micr. Theory and Tech. **47**, 769 (1999); C. L. Holloway and E. F. Kuester, *A quasi-closed form expression for the conductor loss of CPW lines, with an investigation of edge shape effects*, IEEE Trans. on Micr. Theory and Tech. **43**, 2695 (1995).

[17] J. Gao, J. Zmuidzinas, B. A. Mazin, P. K. Day, and H. G. Leduc, *Experimental study of the kinetic inductance fraction of superconducting coplanar waveguide*, Nucl. Instr. and Meth. in Phys. Res. A **559**, 585 (2006).

[18] D. M. Pozar, *Microwave Engineering*, Second Edition, (John Wiley and Sons, 1998).

[19] D. L. Griscom, *Defect structure of glasses - some outstanding questions in regard to vitreous silica*, J. Non-Crystalline Solids **73**, 51 (1985).

[20] R. H. Koch, D. P. DiVincenzo, and J. Clarke, *Model for 1/f flux noise in SQUIDs and qubits*, Phys. Rev. Lett. **98**, 267003 (2007).

[21] B. Golding, M. von Schickfus, S. Hunklinger, and K. Dransfeld, *Intrinsic electric-dipole moment of tunnelling systems in silica glasses*, Phys. Rev. Lett. **43**, 1817 (1979).

[22] R. de Sousa, *Dangling-bond spin relaxation and magnetic 1/f noise from the amorphous-semiconductor/oxide interface: Theory*, Phys. Rev. B **76**, 245306 (2007).

[23] B. D. Jackson, G. de Lange, T. Zijlstra, M. Kroug, J. W. Kooi, J. A. Stern, and T. M. Klapwijk, *Low-noise 0.8-0.96-and 0.96-1.12-THz superconductor-insulator-superconductor mixers for the Herschel space observatory*, IEEE Trans. on Micr. Theory and Tech. **54**, 547 (2006).

[24] D. W. Face and D. E. Prober, *Nucleation of body-centered-cubic tantalum films with a thin niobium underlayer*, J. Vac. Sci. Tech. A **5**, 3408 (1987).

[25] L. Duband, L. Clerc, and A. Ravex, *Socool: A 300 K - 0.3 K pulse tube/sorption cooler*, Proc. AIP Conference **613**, 1233 (2002).

[26] T. O. Klaassen, J. H. Blok, J. N. Hovenier, G. Jakob, D. Rosenthal, and K. J. Wildeman, *Absorbing coatings and diffuse reflectors for the Herschel platform sub-millimeter spectrometers HIFI and PACS*, Proceedings of the IEEE tenth International Conference on Terahertz Electronics, p. 32 (2002).

[27] J. J. A. Baselmans and S. J. C. Yates, private communication.

[28] On the basis of the attenuation at GHz frequencies, the attenuation at 300 GHz is expected to be on the order of 20 dB [18] for the transverse electromagnetic (TEM) mode in a 15 cm long CuNi SMA cable with 0.86 mm outer diameter. When the wavelength is on the order of the diameter of the coaxial cable, propagation modes other than the TEM mode can be excited [18]. Some of these modes have a much weaker attenuation, reminiscent of light in an optical fibre.

Chapter 4

Niobium and tantalum high-Q resonators for photon detectors

We have measured the quality factors and phase noise of niobium and tantalum coplanar waveguide microwave resonators on silicon. The results of both materials are similar. We reach quality factors up to 10^5. At low temperatures the quality factors show an anomalous increase, while the resonance frequency remains constant for increasing power levels. The resonance frequency starts to decrease at temperatures around a tenth of the critical temperature. The phase noise exhibits a 1/f like slope. We attribute this behavior to the silicon dielectric.

This chapter is published as R. Barends, J. J. A. Baselmans, J. N. Hovenier, J. R. Gao, S. J. C. Yates, T. M. Klapwijk, and H. F. C. Hoevers, IEEE Trans. on Appl. Supercond. **17**, 263 (2007).

4.1 Introduction

One of the greatest challenges for far infrared astronomy is the development of sensitive cameras with many pixels (100 x 100 pixels or more), having a background limited sensitivity. To date no such detector exists. Recently a new detector concept has been proposed [1], based on kinetic inductance detectors (KIDs).

Low T_c microwave superconducting resonators with a high quality factor and low noise are the building blocks for KIDs. These consist of $\frac{1}{4}\lambda$ superconducting thin film resonators with a high quality factor (Q factor). These resonators are all capacitively coupled to a through line. Near the resonance frequency they act as a short, and manifest themselves as a dip in the magnitude and a shift in the phase of the through line transmission. KIDs are pair breaking detectors; incident radiation breaks Cooper pairs into quasiparticles, changing the kinetic inductance of the superconductor, and thus the resonance frequency [2, 3].

Typical resonance frequencies lie within the GHz band. Many resonators, each of them having a slightly different resonance frequency, can be operated simultaneously. With only one wideband cryogenic amplifier and commercially available readout electronics a camera with 10^5 pixels can become a reality. KIDs can address the spectrum from the submm range to X-ray, depending on the antenna or absorber.

Recently, there is further interest in low T_c microwave superconducting resonators for the field of cavity quantum electrodynamics (CQED) [5]. Both in the KIDs and CQED case low T_c resonators are operated at subkelvin temperatures.

Whether these KIDs can truly reach a background limited sensitivity is an open question. The sensitivity is a function of the phase noise, quasiparticle lifetime and resonator Q factor [4]. Therefore a clear understanding and characterization of the device is urgently needed.

Here, we focus on the quality factor, resonance frequency and phase noise of low T_c superconducting microwave resonators at subkelvin temperatures.

4.2 Experiment

A layout of the structure can be seen in Fig. 4.1. The chip is placed inside a copper sample box with two SMA panel connectors, which are connected via SMA to CPW circuit boards to the through line. The resonator is capacitively coupled via its open end to the through line. Near the resonance frequency it acts as a short, and a dip in the magnitude and a shift in the phase of the through line transmission can be seen. The transmission near the resonance frequency is

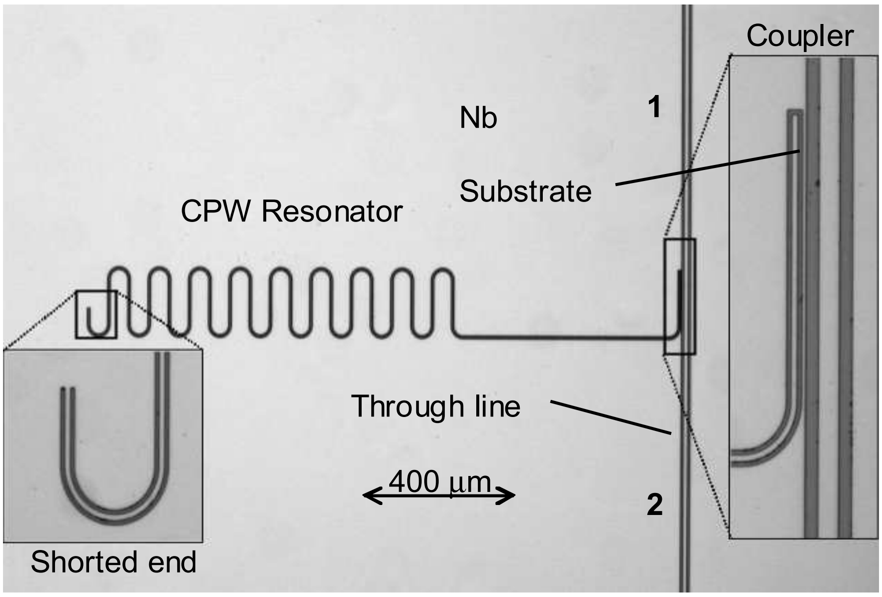

Figure 4.1: The resonator layout. The light areas indicate the superconducting film and the dark areas the substrate. The transmission line is a coplanar waveguide, the central line of the resonator is 3 μm wide, and the gaps are 2 μm wide. The open end of the resonator is coupled to the main through line, which runs across the chip. The resonator is meandered due to its long length (typically a few mm).

given by

$$S_{21} = \frac{S_{21}^{min} + i2Q\frac{\delta\omega_0}{\omega_0}}{1 + i2Q\frac{\delta\omega_0}{\omega_0}} \tag{4.1}$$

with S_{21}^{min} the size of the resonance dip, Q the loaded quality factor and ω_0 the resonance frequency. The unloaded quality factor can be extracted from the transmission since $Q^{-1} = Q_c^{-1} + Q_i^{-1}$ and $S_{21}^{min} = Q_c/(Q_c + Q_i)$, with Q_c the coupling quality factor and Q_i the unloaded quality factor.

The optimal materials for KIDs are still a subject of research, as low losses, a long quasiparticle lifetime, the cryogenic system to be used and KID-antenna coupling schemes are aspects to be considered. As superconductors niobium, due to its relatively large gap and availability, and tantalum, for its quasiparticle lifetime, are chosen. The niobium film is deposited using DC sputter deposition and has a thickness of 100 nm, a critical temperature of 9.2 K and a residual resistivity ratio (RRR) of 4. Prior to 100 nm tantalum deposition a 5 nm niobium seed layer was sputtered to promote growth of the tantalum alpha phase [6]. The critical temperature is 4.0 K, and the RRR is 2.5. The films are deposited on the native oxide of a [100] oriented silicon substrate having a resistivity in excess of

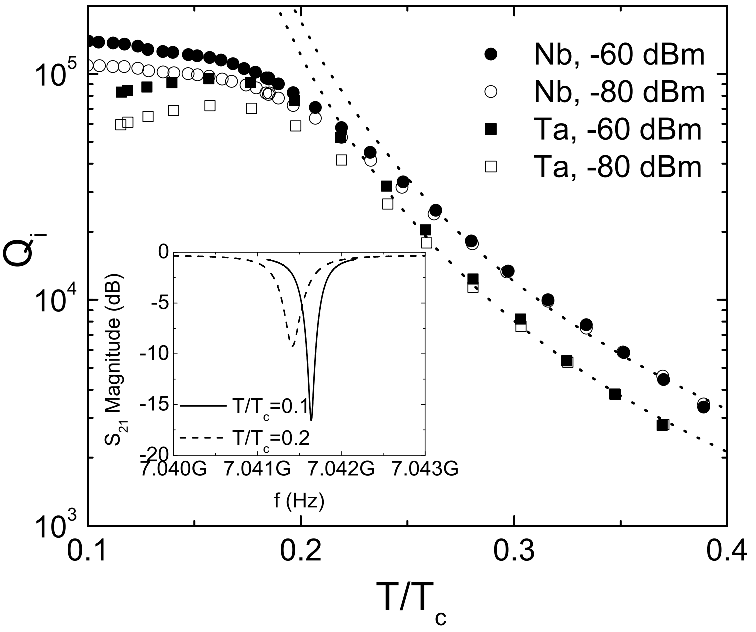

Figure 4.2: Unloaded quality factor of a niobium and tantalum resonator as a function of the reduced temperature. Eq. 4.2 is dotted for both resonators. The inset shows the forward transmission S_{21} of the niobium resonator. For extracting the Q factors these sweeps are fitted to Eq. 4.1.

1 kΩcm and a thickness of 300 μm. Patterning is done using dry etching and e-beam lithography for the niobium and optical lithography for the tantalum film. Both films are in the dirty limit; the electron mean free path is smaller than the coherence length ($l_e \ll \xi_0$).

The sample box is mounted on a He-3 sorption cooler in a cryostat. Aluminum SMA cables carry the signal from and to the 4.2 K cold plate, where a wideband low noise InP MMIC amplifier with a noise temperature of 4 K is mounted. Stainless steel SMA cables are used from the cold plate to room temperature. A room temperature amplifier is used for extra amplification. Only semi-rigid and phase stable flexible SMA cables are used in the setup. For determining the Q factor and resonance frequency we measure the forward transmission S_{21} with a Rohde & Schwarz ZVM vector network analyzer.

The phase noise is obtained using a homodyne detection scheme. The on or off resonance signal is generated by the signal generator. The signal is split with one part traveling through the cryostat and KID chip and being mixed with the other part in an IQ mixer. The I and Q channels are sampled with a 2 channel fast ADC card. A 2 channel variable attenuator is used to control both the power level at the chip and the power level at the IQ mixer RF input. Hence the magnitude and phase of the transmitted signal, $\sqrt{I^2 + Q^2}$ and $\tan(\theta) = \frac{Q}{I}$, can be monitored in time. Calculating the power spectral density gives the magnitude and phase noise.

4.3 Results

We have measured the Q factor, frequency and phase noise of a niobium and tantalum resonator. The niobium resonator has a resonance frequency of 7.04 GHz and a coupling quality $Q_c = 25 \cdot 10^3$. For tantalum the resonance frequency is 2.77 GHz and $Q_c = 19 \cdot 10^3$. Both resonators have a resonance dip of around -15 dB at base temperature. The observed behavior is similar for both devices, therefore the results are plotted together. Typical resonance features can be seen in the inset of Fig. 4.2, with a lowering of temperature the resonance frequency grows and the dip deepens.

The temperature dependence of the unloaded quality factor is shown in Fig. 4.2. The quality factor rises with decreasing temperature and starts to saturate at around $T/T_c = 0.25$ for both niobium and tantalum. The rise follows the two fluid Mattis-Bardeen description of a superconductor [7],

$$Q_{MB} = \frac{2}{\alpha}\frac{\sigma_2}{\sigma_1} \tag{4.2}$$

with $\sigma = \sigma_1 - i\sigma_2$ the complex conductivity and $\alpha = \frac{L_k}{L_t}$ the kinetic inductance fraction. The difference between niobium and tantalum in the unloaded Q factor is due to α.

The unloaded Q factor can be written as $Q_i^{-1} = Q_{MB}^{-1} + Q_s^{-1}$, with Q_s the saturation Q factor, representing the deviation from Mattis-Bardeen theory. At lower temperatures, the Mattis-Bardeen description is no longer applicable, as the Q factor saturates at around 10^5 for both niobium and tantalum, a value which is comparable to results on aluminum KIDs [4]. At $T/T_c = 0.13$ a small jump upwards in the niobium Q factor can be seen and a slight decrease in the tantalum Q factor occurs for $T/T_c < 0.15$. As the readout power is lowered from -60 dBm to -80 dBm, clearly the saturation Q factor decreases, while the Q factor in the range where the Mattis-Bardeen description is valid does not visibly change.

The latter is shown in more detail in Fig. 4.3; the unloaded Q factor is plotted for varying power levels and constant temperatures. Only in the satura-

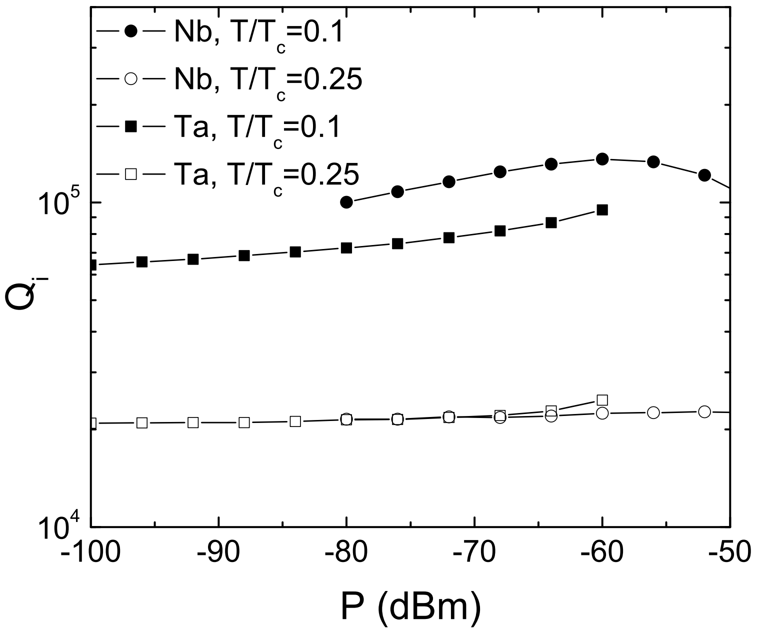

Figure 4.3: Unloaded quality factor versus the microwave power level in the through line for different reduced temperatures. At higher temperatures Q_{MB} (Eq. 4.2) dominates and is power independent for low power levels.

tion regime, at $T/T_c = 0.1$, the Q factor monotonically increases with increasing power levels over a large domain up to -60 dBm. This increase occurs in both the niobium and tantalum device. At $T/T_c = 0.25$ the Q factor starts to change only for high power levels.

The resonance frequency versus temperature is shown in Fig. 4.4. With a lowering of bath temperature the resonance frequency increases and seems to settle at around $T/T_c = 0.2$. Closer inspection reveals that the slope changes sign at low temperatures, see inset. The resonance frequency depends non-monotonically on the temperature in both devices. The resonance frequency is power independent up to -55 dBm where it starts to decrease for both devices (not shown).

The phase noise of both resonators is shown in Fig. 4.5. The key result is that there is a logarithmic dependence of the phase noise on the frequency at lower frequencies ($S_\theta \propto f^{-k}$). For the niobium resonator the dependence is close to 1/f ($k \approx 1$), while for tantalum the power k is not an integer, which we will refer to as 1/f *like*. For the tantalum resonator a plateau exists at -115 dBc/Hz, between settling of the slope and the noise roll-off frequency given by the response time

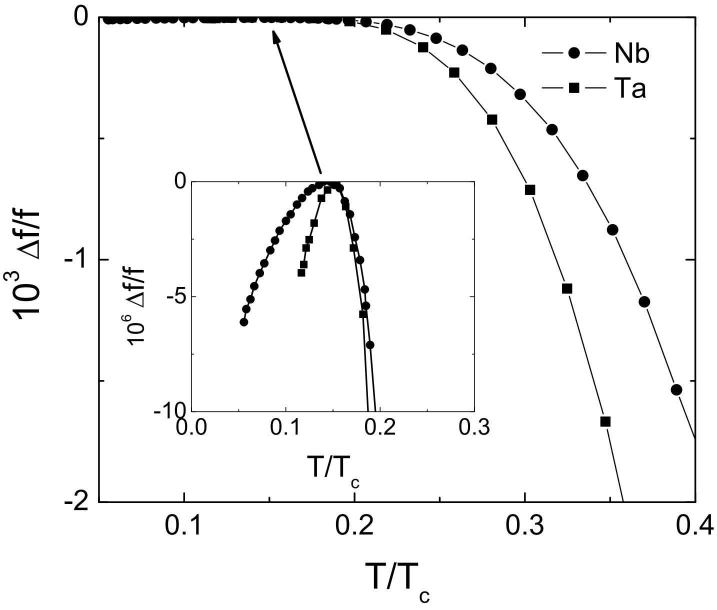

Figure 4.4: Resonance frequency versus temperature. At lower temperatures the kinetic inductance decreases and the resonance frequency increases subsequently. The inset reveals that the slope changes sign at low temperatures.

of the resonator.

4.4 Discussion

We focus on the saturation quality factor power dependence, non-monotonic temperature dependence of the resonance frequency and 1/f like phase noise. The quality factor is $Q = \frac{\omega L}{R}$, with L the inductance and R the resistance. The resonance frequency depends on the inductance only and we can discriminate whether Q factor behavior should be ascribed to L or R. The Q factor increases with power level, while the resonance frequency does not visibly change. We attribute this behavior to a power dependent loss mechanism.

Both films are sputter deposited and have been exposed to air prior to being measured. Microwave cavities with oxidized films and a certain degree of granularity are known to involve grain boundaries, vortices and weak links in the residual surface resistance [8, 9, 10, 11, 12]. Niobium oxides are known to be partly metallic, creating subgap quasiparticle states [13] leading to a non-exponential decay of the surface resistance. The niobium oxides are also known to be superconducting under certain conditions which might be related to the

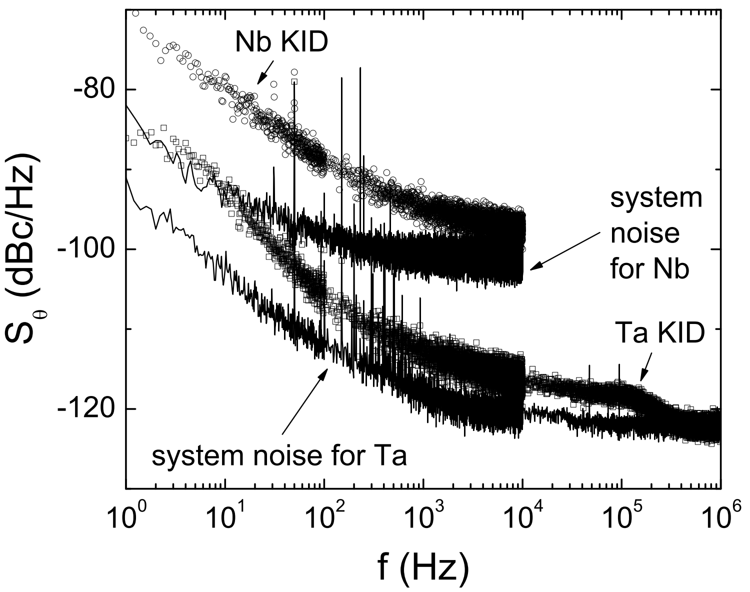

Figure 4.5: The phase noise S_θ of a niobium and tantalum resonator, measured at a power of -60 dBm for niobium and -55 dBm for tantalum. For on resonance the signal is applied at exactly the resonance frequency, for off resonance the signal is applied outside of the resonance dip, giving the system noise. The noise roll-off of the tantalum resonator can be seen at 100 KHz.

small jump in the Q factor [14]. The niobium and tantalum films are in the dirty limit, and due to their thickness are type II superconductors, leading to vortex related effects.

Both cases of a Q factor increasing or decreasing with power level have been reported [8, 9, 10, 11, 12]. The magnetic field strength is proportional to the square root of power inside the resonator. Several degrees of surface resistance field dependence $R_s \propto {H_{rf}}^n$ have been observed. The behavior has been observed to be independent, sublinear, linear, quadratic or even a more rapid function of the microwave field. This leads to a Q factor which, depending on the powerlaw behavior of L and R, increases or decreases with power. In our case however clearly the losses decrease with increasing power while the inductance remains constant; which seems to be not consistent with mechanisms taking place in the superconducting film. The non-monotonic temperature dependence of the resonance frequency in the same temperature range also does not seem to originate from superconductivity related effects.

Resonator losses can also be raised by the dielectric. In a CPW geometry the electric fields stand between the center and outer conductors, and are strongest at the silicon surface. The devices are exposed to air prior to being measured, and native oxide is formed. Native silicon oxide formed on [100] wafers is amorphous [15].

Microwave properties of amorphous systems are known to be affected by two level systems [16, 17]. Two level systems with a dipole moment can couple to the electric field and the associated dielectric losses reduce with a growing microwave field intensity. The dielectric constant and thus the resonance frequency can also be affected. Depending on wether resonant or relaxation two level systems dominate, the dielectric constant shrinks or grows with an increase of temperature. The small decrease of the resonance frequency at low temperatures is consistent with resonant tunneling systems in amorphous dielectrics [16]. The importance of dipole defects has recently been appreciated in relating the decrease of losses to the substrate in a superconducting cavity [18].

The phase noise of both resonators shows a 1/f like slope. Our measurements are in agreement with earlier results on KIDs with aluminum CPW resonators on silicon [4]. Moreover, in this experiment the silicon substrate was replaced by a sapphire one or etched away, leading in both cases to a reduction in S_θ of around 20 dBc/Hz at low frequencies, convincingly showing that a 1/f like noise source, in their case a dominant one, resides in or on the silicon substrate. It is interesting to note that two level systems are a possible 1/f noise source [19, 20]. For our case the noise in the dielectric constant translates into noise in the resonance frequency and observed phase.

4.5 Conclusions

To conclude, we have measured the quality factor, resonance frequency and phase noise of niobium and tantalum on silicon $\frac{1}{4}\lambda$ CPW GHz resonators, with temperatures down to 300 mK. The measurements were done using a vector network analyzer and IQ mixer.

The results of the niobium and tantalum resonator are similar. In both materials the quality factor follows Mattis-Bardeen theory up to a saturation value, typically being 10^5. This saturation value is comparable to results on aluminum KIDs. The saturation Q factor increases with readout power, while the resonance frequency starts to decrease only at high power levels. We attribute the Q factor power dependence to a decrease of microwave losses for increasing power levels. The resonance frequency has a non-monotonic temperature dependence. When lowering the temperature the resonance frequency grows, yet at around a tenth of the critical temperature the frequency starts to decrease. The phase noise of both resonators exhibits a 1/f like slope. Superconductivity related mechanisms are not enough to explain this behavior. The various mechanisms in the superconductor such as film granularity and vortices are known to increase the surface impedance with increasing power in the low power limit, whereas we observe the opposite.

Qualitatively the Q factor power dependence, non-monotonic frequency temperature dependence and 1/f like slope in the phase noise at low temperatures could be attributed to two level systems in the silicon dielectric. The resonators used here are a unique tool capable of observing these probably interrelated effects. Further research is needed to understand the saturation regime and identify the limitations of low temperature microwave resonators.

References

[1] P. K. Day, H. G. LeDuc, B. A. Mazin, A. Vayonakis and J. Zmuidzinas, *A broadband superconducting detector for use in large arrays*, Nature **425**, 817 (2003).

[2] S. Doyle, J. Naylon, J. Cox, P. Mauskopf, A. Porch, *Kinetic inductance detectors for 200 μm astronomy*, Proc. SPIE **6275**, 6275O1 (2006).

[3] J. J. A. Baselmans, R. Barends, S. J. C. Yates, J. N. Hovenier, J. R. Gao, H. F. C. Hoevers and T. M. Klapwijk, *Development of high-Q superconducting resonators for use as kinetic inductance detectors*, Proc. 7th Int. Workshop on Low Temperature Electronics, Noordwijk, The Netherlands, June 2006.

[4] B. A. Mazin, *Microwave kinetic inductance detectors*, Ph.D. dissertation, California Institute of Technology, 2004.

[5] A. Wallraff, D. I. Schuster, A. Blais, L. Frunzio, R. S. Huang, J. Majer, S. Kumar, S. M. Girvin and R. J. Schoelkopf, *Strong coupling of a single photon to a superconducting qubit using circuit quantum electrodynamics*, Nature **431**, 162 (2004).

[6] D. W. Face and D. E. Prober, *Nucleation of body-centered-cubic tantalum films with a thin niobium underlayer*, J. Vac. Sci. Tech. A **5**, 3408 (1987).

[7] D. C. Mattis and J. Bardeen, *Theory of the anomalous skin effect in normal and superconducting metals*, Phys. Rev. **111**, 412 (1958).

[8] A. V. Velichko, M. J. Lancaster and A. Porch, *Nonlinear microwave properties of high T_c thin films*, Supercond. Sci. Technol. **18**, R24 (2005).

[9] J. Halbritter, *Transport in superconducting niobium films for radio frequency applications*, J. Appl. Phys. **97**, 083904 (2005).

[10] C. Attanasio, L. Maritato and R. Vaglio, *Residual surface resistance of polycrystalline superconductors*, Phys. Rev. B **43**, 6128 (1991).

[11] C. C. Chin, D. E. Oates, G. Dresselhaus and M. S. Dresselhaus, *Nonlinear electrodynamics of superconducting NbN and Nb thin films at microwave frequencies*, Phys. Rev. B **45**, 4788 (1992).

[12] P. Lahl and R. Wördenweber, *Fundamental microwave-power-limiting mechanism of epitaxial high-temperature superconducting thin-film devices*, J. Appl. Phys **97**, 113911 (2005).

[13] M. Ohkubo, J. Martin, K. Drachsler, R. Gross, R. P. Huebener, I. Sakamoto and N. Hyashi, *Asymmetric response of superconducting niobium-tunnel-junction x-ray detectors*, Phys. Rev. B **54**, 9484 (1996).

[14] J. K. Hulm, C. K. Jones, R. A. Hein and J. W. Gibson, *Superconductivity in the TiO and NbO systems*, J. Low Temp. Phys. **7**, 291 (1972).

[15] A. H. Carim, M. M. Dovek, C. F. Quate, R. Sinclair and C. Vorst, *High-resolution electron microscopy and scanning tunneling microscopy of native oxides on silicon*, Science **237**, 630 (1987).

[16] C. Enss and S. Hunklinger, *Low-Temperature Physics*, (Springer Verlag, 2005).

[17] W. A. Phillips, *Two-level states in glasses*, Rep. Prog. Phys. **50**, 1657 (1987).

[18] M. A. Hein, D. E. Oates, P. J. Hirst, R. G. Humphreys and A. V. Velichko, *Nonlinear dielectric microwave losses in MgO substrates*, Appl. Phys. Lett. **80**, 1007 (2002).

[19] M. B. Weissman, *1/f noise and other slow, nonexponential kinetics in condensed matter*, Rev. Mod. Phys. **60**, 537 (1988).

[20] C. C. Yu, *Why study noise due to two level systems: a suggestion for experimentalists*, J. Low Temp. Phys. **137**, 251 (2004).

Chapter 5

Quasiparticle relaxation in optically excited high-Q superconducting resonators

The quasiparticle relaxation time in superconducting films has been measured as a function of temperature using the response of the complex conductivity to photon flux. For tantalum and aluminium, chosen for their difference in electron-phonon coupling strength, we find that at high temperatures the relaxation time increases with decreasing temperature, as expected for electron-phonon interaction. At low temperatures we find in both superconducting materials a saturation of the relaxation time, suggesting the presence of a second relaxation channel not due to electron-phonon interaction.

This chapter is published as R. Barends, J. J. A. Baselmans, S. J. C. Yates, J. R. Gao, J. N. Hovenier, and T. M. Klapwijk, Phys. Rev. Lett. **100**, 257002 (2008).

5.1 Introduction

The equilibrium state of a superconductor at finite temperatures consists of the Cooper pair condensate and thermally excited quasiparticles. The quasiparticle density n_{qp} decreases exponentially with decreasing temperature. These charge carriers control the high frequency (ω) response of the superconductor through the complex conductivity $\sigma_1 - i\sigma_2$. At nonzero frequencies the real part σ_1 denotes the conductivity by quasiparticles and the imaginary part σ_2 is due to the superconducting condensate [1, 2]. When the superconductor is driven out of equilibrium it relaxes back to the equilibrium state by the redistribution of quasiparticles over energy and by recombination of quasiparticles to Cooper pairs. The recombination is a binary reaction, quasiparticles with opposite wavevector and spin combine, and the remaining energy is transferred to another excitation. The latter process is usually controlled by the material dependent electron-phonon interaction [3, 4]. With decreasing temperatures the recombination time increases exponentially reflecting the reduced availability of quasiparticles. Here, we report relaxation time measurements in superconducting films far below the critical temperature T_c. We find strong deviations from exponentially rising behavior, which we attribute to the emergence of an additional relaxation channel in the superconducting films.

5.2 Probing quasiparticle relaxation with the complex conductivity

We have measured the time dependence of the complex conductivity of superconducting films after applying an optical photon pulse. In addition, the noise spectrum is measured in the presence of a continuous photon flux [5]. The superconducting film is patterned as a planar microwave resonator. The resonator is formed by a meandering coplanar waveguide (CPW), with the central line 3 μm and the slits 2 μm wide, and is coupled to a feedline, see Fig. 5.1a [6]. The complex conductivity results in a kinetic inductance $L_k \propto 1/d\omega\sigma_2$, for thin films with thickness d, which is due to the inertia of the Cooper pair condensate. It sets together with the length of the central line the resonance frequency: $\omega_0 = 2\pi/4l\sqrt{(L_g + L_k)C}$, with l the length of a quarterwave resonator, L_g the geometric inductance and C the capacitance, both per unit length. The variation in kinetic inductance due to photons is connected to the quasiparticle density n_{qp} by $\delta L_k/L_k = \frac{1}{2}\delta n_{qp}/n_{cp}$, with n_{cp} the Cooper pair density ($n_{qp} \ll n_{cp}$). Resonance frequencies used lie between 3-6 GHz. For a quarterwave resonator at

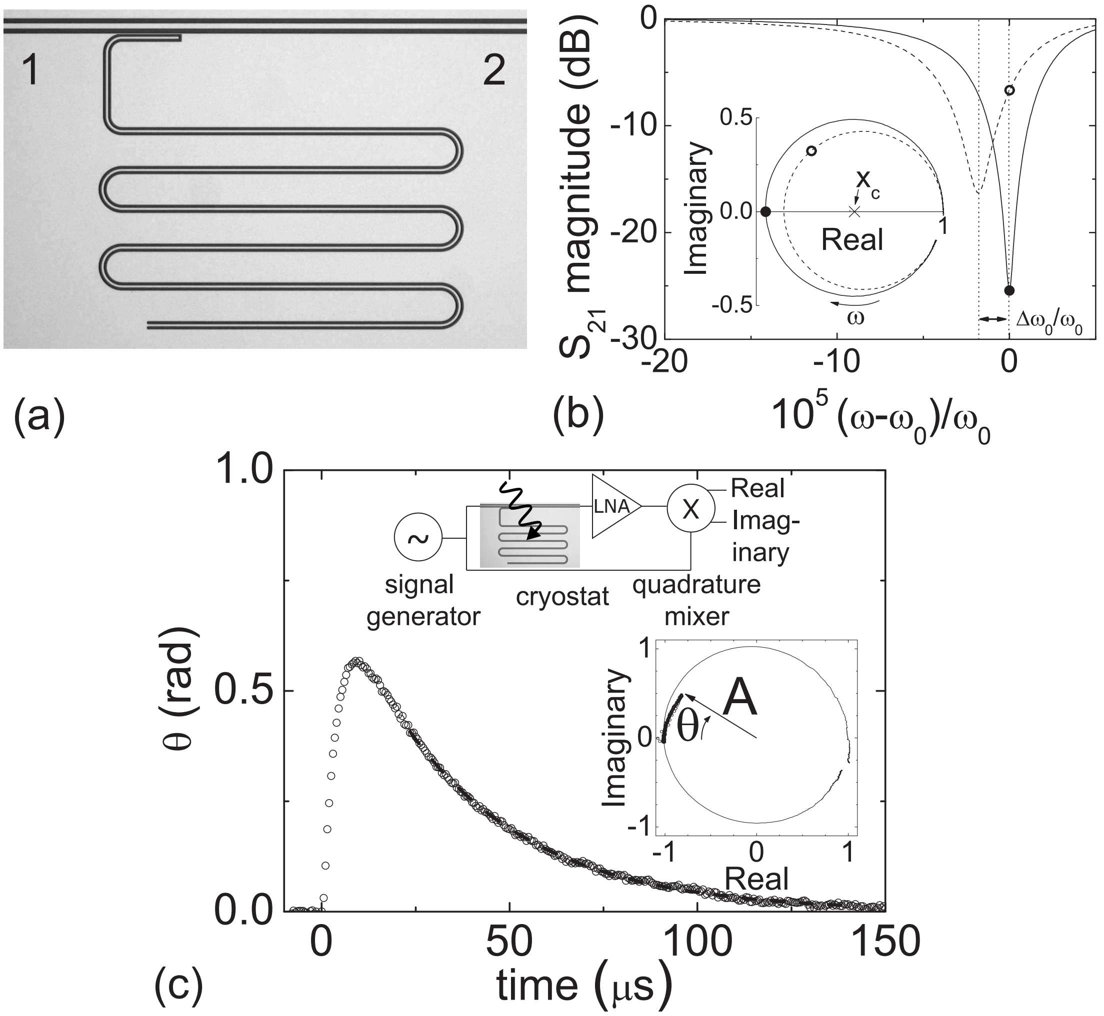

Figure 5.1: (a) A quarter wavelength resonator, capacitively coupled to a feedline, formed by the superconducting film (gray) interrupted by slits (black). (b) The resonator exhibits a dip in the magnitude and circle in the complex plane (inset) of the feedline transmission S_{21}. (c) The feedline transmission is converted into a phase θ and amplitude A using the equilibrium resonance circle as reference (right inset). The response to an optical pulse of length 0.5 μs (at t=0) (open circles) exhibits an initial rise due to the response time (3.7 μs) of the resonator and subsequently follows an exponential decay (34 μs) (dashed), reflecting the restoration of equilibrium (Eq. 5.1). The response is measured with a signal generator, low noise amplifier (LNA) and quadrature mixer (upper inset).

6 GHz, the length of the meandering superconducting CPW-line is 5 mm. The resonator is capacitively coupled by placing a part parallel to the feedline.

The resonators are made from superconducting materials with different electron-phonon interaction strengths, tantalum (strong interaction) and aluminium (weak interaction). The tantalum film, 150 nm thick, is sputtered on a high resistivity silicon substrate. A 6 nm thick niobium seed layer is used to promote the growth of the desired tantalum alpha phase [7]. The critical temperature T_c is 4.43 K, the low temperature resistivity ρ is 8.4 $\mu\Omega$cm and the residual resistance ratio (RRR) is 3.0. A 100 nm thick aluminium film is sputtered on silicon (T_c=1.25, ρ=1.3 $\mu\Omega$cm, RRR=3.7). Alternatively, a film of 250 nm thick is sputtered on silicon (T_c=1.22, ρ=1.0 $\mu\Omega$cm, RRR=6.9) and another one of 250 nm is sputtered on A-plane sapphire (T_c=1.20, ρ=0.25 $\mu\Omega$cm, RRR=11). The samples are patterned using optical lithography, followed by wet etching for aluminium and reactive ion etching for tantalum. For both materials quality factors in the order of 10^6 are reached. The sample is cooled in a cryostat with an adiabatic demagnetization refrigerator. The sample space is surrounded by a cryoperm and a superconducting magnetic shield. Alternatively, the sample is cooled in a cryostat with a ^{3}He sorption cooler without magnetic shields. A GaAsP LED (1.9 eV) acts as photon source, fibre-optically coupled to the sample box.

The complex transmission S_{21} of the circuit is measured by sweeping the frequency of the signal applied along the feedline (Fig. 5.1a). Near the resonance frequency ω_0 the feedline transmission exhibits a decrease in magnitude and traces a circle in the complex plane (full lines in Fig. 5.1b). A non-equilibrium state results in a resonance frequency shift and broadening of the dip, and a reduction and shift of the resonance circle in the complex plane (dashed lines in Fig. 5.1b). The actual signals (filled dot and open circle in Fig. 5.1b) are obtained by sending a continuous wave at the equilibrium resonance frequency ω_0 through the feedline, which is amplified and mixed with a copy of the original signal in a quadrature mixer, whose output gives the real and imaginary part of the feedline transmission (upper inset Fig. 5.1c). The non-equilibrium response (open circle), compared to the equilibrium response (filled dot), is characterized by a changed phase θ and amplitude A, referred to a shifted origin in the complex plane (from the equilibrium position x_c).

The phase θ with respect to the resonance circle center x_c is given by $\theta = \arctan\{\text{Im }(S_{21})/[x_c - \text{Re }(S_{21})]\}$ and is related to the change in resonance frequency by: $\theta = -4Q\frac{\delta\omega_0}{\omega_0}$, with Q the resonator loaded quality factor [6]. A related change in L_k is given by $\delta\omega_0/\omega_0 = -\frac{\alpha}{2}\delta L_k/L_k$, with α the ratio of the kinetic to the total inductance. The phase θ is therefore a direct measure of the change in complex conductivity (given in the dirty limit by):

$$\theta = -2\alpha Q\frac{\delta\sigma_2}{\sigma_2}\Big(f(E),\Delta\Big), \tag{5.1}$$

with $f(E)$ the electronic distribution function characterizing the non-equilibrium and Δ the superconductor energy gap.

The amplitude A depends predominantly on σ_1 and to a smaller degree on σ_2. The amplitude is determined by the complex transmission S_{21} by: $A = \sqrt{[\mathrm{Re}(S_{21}) - x_c]^2 + \mathrm{Im}(S_{21})^2}/(1 - x_c)$. On resonance $S_{21} = Q_c/(Q_c + Q_u)$ with $Q_u \propto \sigma_2/\sigma_1$ the unloaded resonator quality factor and Q_c the coupling quality factor, leading to

$$A = 1 - 2\frac{Q}{Q_u}\left[\frac{\delta\sigma_1}{\sigma_1}\Big(f(E), \Delta\Big) - \frac{\delta\sigma_2}{\sigma_2}\Big(f(E), \Delta\Big)\right]. \tag{5.2}$$

By measuring A and θ in the frequency- and time-domain we obtain direct information on the relaxation through the complex conductivity of the superconducting films.

5.3 Relaxation in the frequency domain

A typical pulse response is shown in Fig. 5.1c. The initial rise of the phase θ is due to the response time of the resonator. The relaxation shows up as an exponential decay. The right inset of Fig. 5.1c shows the evolution of the response in the transformed polar plane. These data are interpreted as governed by one relaxation time. This is justified by performing measurements of the noise spectrum and applying the analysis by Wilson *et al.* [5]. Since the superconducting condensate and the quasiparticle excitations form a two-level system a Lorentzian spectrum is expected, with the relaxation time determining the roll-off frequency. If more dominant relaxation processes are present, the noise spectrum is no longer a single Lorentzian [8]. We have studied the superconducting films under exposure to a *continuous* photon flux. Our films are exposed to an optical white noise signal due to photon shot noise, resulting in fluctuations in $f(E)$. Where a single time τ determines the relaxation process the phase or amplitude noise spectrum is

$$S_{\theta,A} = \frac{2\hbar\Omega}{P}\frac{r_{\theta,A}}{1 + (2\pi f\tau)^2}, \tag{5.3}$$

with P the absorbed power, $\hbar\Omega$ the photon energy, and $r_{\theta,A}$ denoting the responsivity of the phase or amplitude to an optical signal.

The measured noise power spectra of the amplitude and phase of a tantalum sample are shown in Fig. 5.2. In equilibrium the amplitude noise spectrum is flat over the full range, and the phase noise follows $1/f^a$ with $a \approx 0.25$. The amplitude noise is due to the amplifier, remaining unchanged at frequencies far away from ω_0 while the phase noise is dominated by resonator noise [9, 10], rolling

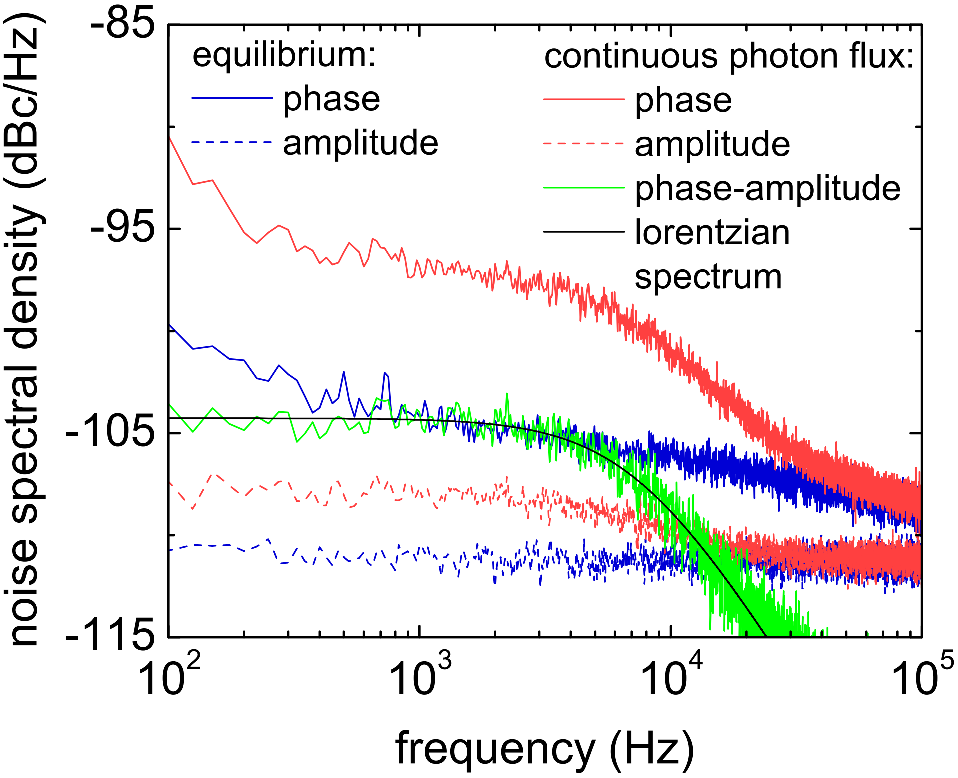

Figure 5.2: The power spectral density of phase (solid line) and amplitude (dashed) in equilibrium and under a continuous photon flux at a bath temperature of 310 mK. The cross-power spectral density under a continuous photon flux follows a single pole Lorentzian spectrum, $S \propto [1 + (2\pi f\tau)^2]^{-1}$, with a characteristic time of 21.7±0.3 μs (solid line). The response time of the resonator is 0.5 μs.

off at a frequency corresponding to the resonator response time (0.5 μs). Under a continuous photon flux we observe excess noise in both amplitude and phase that rolls off to the equilibrium value around 8 kHz.

The difference in noise levels is equal to the difference in responsivity: $r_A/r_\theta = 0.23$ (-13 dB), measured for this sample. In addition, we estimate, based on 20 pW optical power absorbed by the resonator, a phase noise level of -94 dBc/Hz due to photon shot noise (see Appendix C), which is close to the observed value. Thus we conclude that the excess noise is due to variations in $f(E)$ induced by the photon flux. In order to eliminate the system and resonator noise we calculate the phase-amplitude cross-power spectral density. We find that its spectrum is

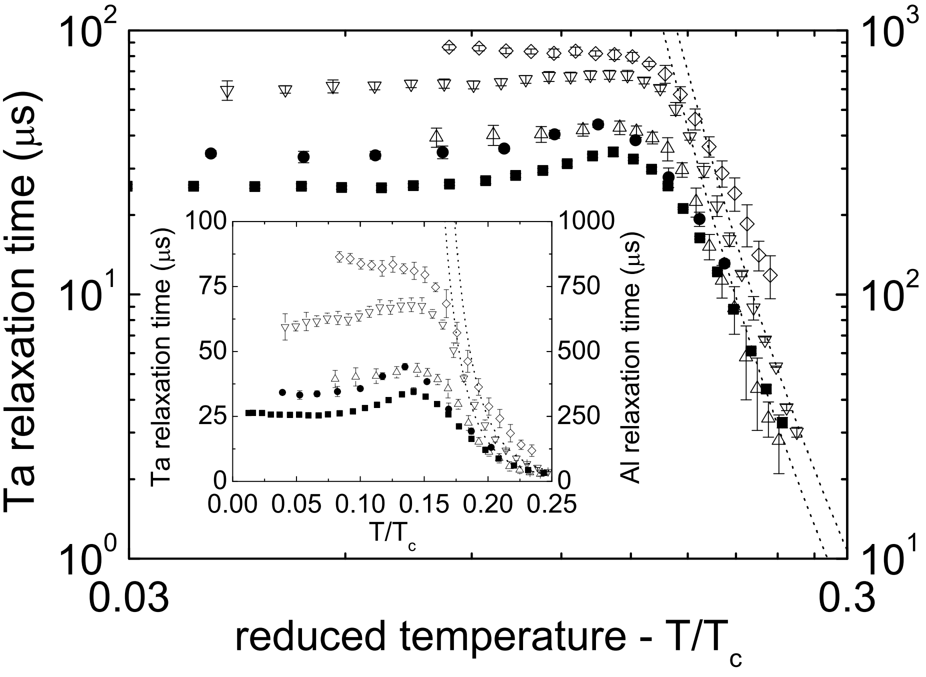

Figure 5.3: The relaxation times as a function of reduced bath temperature for 150 nm Ta on Si (■, ●), 100 nm Al on Si (△), 250 nm Al on Si (▽) and 250 nm Al on sapphire (◇) samples. The inset shows the same data on a linear scale. The dotted lines are fits to the data using Eq. 5.4.

real, indicating that variations in $f(E)$ appear as fluctuations in the amplitude and phase without relative time delay, and that the data follow a Lorentzian spectrum with a single time. The time measured in the pulse response (23.0±0.5 μs) agrees with the one determined from the noise spectrum (21.7±0.3 μs). We have checked at several bath temperatures and found, also for aluminium samples, only a single time. We conclude that the relaxation time is the single dominant time in the recovery of equilibrium.

5.4 Low temperature saturation of relaxation

The measured relaxation times for temperatures down to 50 mK are displayed in Fig. 5.3. The data shown are representative for the relaxation times found in all samples of different films. In the high temperature regime ($T/T_c \gtrsim 0.175$) the relaxation times increase for decreasing bath temperature in a similar manner for both tantalum and aluminium samples until a new regime is entered around $T/T_c \sim 0.15$. The tantalum samples clearly show a non-monotonic temperature dependence, exhibiting a maximum near $T/T_c \sim 0.15$. Two aluminium films show a less pronounced non-monotonic temperature dependence. We do not see a non-monotonic temperature dependence in samples of aluminium with the lowest level of disorder (highest RRR). Below $T/T_c \sim 0.1$ the relaxation times become temperature independent at a plateau value of 25-35 μs for Ta, 390 μs for 100 nm thick Al on Si, 600 μs for 250 nm thick Al on Si and 860 μs for 250 nm thick Al on sapphire.

The relaxation times for aluminium are measured in half wavelength resonators where the central line is isolated from the ground plane. For the directly connected quarter wavelength resonators a length dependence was found. For tantalum the values are found to be length independent in both cases. Consequently, the data shown are not influenced by quasiparticle outdiffusion. Also, the relaxation times remain unchanged when instead of an optical pulse a microwave pulse at frequency ω_0 is used. In this method only quasiparticle excitations near the gap energy are created by the pair-breaking current. This observation leads us to believe that the observed decay is due to recombination of quasiparticles with energies near the gap.

The exponential temperature dependence for $T/T_c \gtrsim 0.175$ is consistent with the theory of recombination by electron-phonon interaction [4]. The dotted lines in Fig. 5.3 follow the expression for the recombination time,

$$\frac{1}{\tau_{rec}} = \frac{1}{\tau_0}\sqrt{\pi}\Big(\frac{2\Delta}{kT_c}\Big)^{5/2}\sqrt{\frac{T}{T_c}}e^{-\frac{\Delta}{kT}}, \tag{5.4}$$

with τ_0 a material-specific electron-phonon scattering time. We find for 150 nm Ta on Si $\tau_0 = 42\pm2$ ns and for 250 nm Al on Si $\tau_0 = 687\pm6$ ns. The deviation from the exponential rise and the low temperature behavior is incompatible with the established theory for electron-phonon relaxation. We assume that an additional relaxation channel [11] is dominant at low temperatures, where the electron-phonon mechanism becomes too slow.

5.5 Discussion

In previous experiments using superconducting tunnel junctions a similar saturation in the quasiparticle loss has been reported. For photon detectors inverse loss rates in the order of tens of microseconds have been found for tantalum [12, 13, 14, 15] and hundreds of microseconds for aluminium [6]. Some of these experiments also indicated a non-monotonic temperature dependence [16]. Most of these observations have been attributed to trapping states at surfaces or in dielectrics. The fact that our similar experimental results occur in simple superconducting films and two different materials suggests that processes in the superconducting film itself lead to the observed low temperature behavior.

The observed saturation in the relaxation times in our samples is reminiscent of experiments in normal metals on inelastic scattering in non-thermal distributions and on dephasing in weak localization studies. The apparent saturation of the dephasing time and the strong quasiparticle energy exchange at low temperatures have been shown to be caused by dilute concentrations of magnetic impurities [17, 18, 19, 20]. It is known that in superconductors a large density of magnetic impurities decreases the critical temperature. For dilute magnetic impurities the local properties are most important. In experiments with magnetic adatoms impurity bound excitations arise [21], tails in the density of states within the gap might form and the formation of an intragap band with growing impurity concentration are predicted [22, 23]. In ongoing experiments we observe a gradual decrease of the relaxation time with an increasing ion-implanted magnetic impurity concentration (0-100 ppm). However, disorder plays a role as well and further experiments are needed to clarify possible relaxation processes [24].

In conclusion, we find that the quasiparticle relaxation times, probed by means of the complex conductivity, saturate for both tantalum and aluminium, below a tenth of the critical temperature. We suggest that the saturation of the relaxation time is due to the presence of a relaxation channel, which is not caused by the conventional process dominated by electron-phonon interaction.

References

[1] M. Tinkham, *Introduction to Superconductivity* (McGraw-Hill, New York, 1996).

[2] D. C. Mattis and J. Bardeen, *Theory of the anomalous skin effect in normal and superconducting metals*, Phys. Rev. **111**, 412 (1958).

[3] B. I. Miller and A. H. Dayem, *Relaxation and recombination times of quasiparticles in superconducting Al thin films*, Phys. Rev. Lett. **18**, 1000 (1967).

[4] S. B. Kaplan, C. C. Chi, D. N. Langenberg, J. J. Chang, S. Jafarey, and D. J. Scalapino, *Quasiparticle and phonon lifetimes in superconductors*, Phys. Rev. B **14**, 4854 (1976).

[5] C. M. Wilson, L. Frunzio, and D. E. Prober, *Time-resolved measurements of thermodynamic fluctuations of the particle number in a nondegenerate Fermi gas*, Phys. Rev. Lett. **87**, 067004 (2001).

[6] P. K. Day, H. G. LeDuc, B. A. Mazin, A. Vayonakis, and J. Zmuidzinas, *A broadband superconducting detector suitable for use in large arrays*, Nature **425**, 817 (2003).

[7] D. W. Face and D. E. Prober, *Nucleation of body-centered-cubic tantalum films with a thin niobium underlayer*, J. Vac. Sci. Tech. A **5**, 3408 (1987).

[8] C. M. Wilson and D. E. Prober, *Quasiparticle number fluctuations in superconductors*, Phys. Rev. B **69**, 094524 (2004).

[9] J. Gao, J. Zmuidzinas, B. A. Mazin, H. G. LeDuc, and P. K. Day, *Noise properties of superconducting coplanar waveguide microwave resonators*, Appl. Phys. Lett. **90**, 102507 (2007).

[10] R. Barends, H. L. Hortensius, T. Zijlstra, J. J. A. Baselmans, S. J. C. Yates, J. R. Gao, and T. M. Klapwijk, *Contribution of dielectrics to frequency and noise of NbTiN superconducting resonators*, Appl. Phys. Lett. **92**, 223502 (2008).

[11] A possible contribution to quasiparticle recombination by electron-electron interaction involving a three body process has been proposed in M. Reizer, *Electron-electron relaxation in two-dimensional impure superconductors*, Phys. Rev. B **61**, 7108 (2000); in which also an exponential increase with decreasing temperature is predicted.

[12] P. Verhoeve, R. den Hartog, A. G. Kozorezov, D. Martin, A. van Dordrecht, J. K. Wigmore, and A. Peacock, *Time dependence of tunnel statistics and the energy resolution of superconducting tunnel junctions*, J. Appl. Phys. **92**, 6072 (2002).

[13] T. Nussbaumer, Ph. Lerch, E. Kirk, A. Zehnder, R. Füchslin, P. F. Meier, and H. R. Ott, *Quasiparticle diffusion in tantalum using superconducting tunnel junctions*, Phys. Rev. B **61**, 9719 (2000).

[14] L. Li, L. Frunzio, C. M. Wilson, and D. E. Prober, *Quasiparticle nonequilibrium dynamics in a superconducting Ta film*, J. Appl. Phys. **93**, 1137 (2003).

[15] B. A. Mazin, B. Bumble, P. K. Day, M. E. Eckart, S. Golwala, J. Zmuidzinas, and F. A. Harrison, *Position sensitive x-ray spectrophotometer using microwave kinetic inductance detectors*, Appl. Phys. Lett., **89**, 222507 (2006).

[16] A. G. Kozorezov, J. K. Wigmore, A. Peacock, A. Poelaert, P. Verhoeve, R. den Hartog, and G. Brammertz, *Local trap spectroscopy in superconducting tunnel junctions*, Appl. Phys. Lett. **78**, 3654 (2001).

[17] F. Pierre, A. B. Gougam, A. Anthore, H. Pothier, D. Esteve, and N. O. Birge, *Dephasing of electrons in mesoscopic metal wires*, Phys. Rev. B **68**, 085413 (2003).

[18] A. Anthore, F. Pierre, H. Pothier, and D. Esteve, *Magnetic-field-dependent quasiparticle energy relaxation in mesoscopic wires*, Phys. Rev. Lett. **90**, 076806 (2003).

[19] B. Huard, A. Anthore, N. O. Birge, H. Pothier, and D. Esteve, *Effect of magnetic impurities on energy exchange between electrons*, Phys. Rev. Lett. **95**, 036802 (2005).

[20] L. Saminadayar, P. Mohanty, R. A. Webb, P. Degiovanni, and C. Bäuerle, *Electron coherence at low temperatures: The role of magnetic impurities*, Physica E **40**, 12 (2007).

[21] A. Yazdani, B. A. Jones, C. P. Lutz, M. F. Crommie, and D. M. Eigler, *Probing the local effects of magnetic impurities on superconductivity*, Science **275**, 1767 (1997).

[22] A. Silva and L. B. Ioffe, *Subgap states in dirty superconductors and their effect on dephasing in Josephson qubits*, Phys. Rev. B **71**, 104502 (2005).

[23] A. V. Balatsky, I. Vekhter, and J. X. Zhu, *Impurity-induced states in conventional and unconventional superconductors*, Rev. Mod. Phys. **78**, 373 (2006).

[24] A. G. Kozorezov, A. A. Golubov, J. K. Wigmore, D. Martin, P. Verhoeve, R. A. Hijmering, and I. Jerjen, *Inelastic scattering of quasiparticles in a superconductor with magnetic impurities*, Phys. Rev. B **78**, 174501 (2008).

Chapter 6

Enhancement of quasiparticle recombination in Ta and Al superconductors by implantation of magnetic and nonmagnetic atoms

The quasiparticle recombination time in superconducting films, consisting of the standard electron-phonon interaction and a yet to be identified low temperature process, is studied for different densities of magnetic and nonmagnetic atoms. For both Ta and Al, implanted with Mn, Ta and Al, we observe an increase of the recombination rate. We conclude that the enhancement of recombination is not due to the magnetic moment, but arises from an enhancement of disorder.

This chapter is published as R. Barends, S. van Vliet, J. J. A. Baselmans, S. J. C. Yates, J. R. Gao, and T. M. Klapwijk, Phys. Rev. B **79**, 020509(R) (2009).

6.1 Introduction

When a superconductor is perturbed, the equilibrium state is recovered by the recombination of excess quasiparticle excitations. Recombination is a binary reaction, quasiparticles with opposite wave vector and spin combine and join the superconducting condensate formed by the Cooper pairs, pairs of time-reversed electron states; the energy is transferred to the lattice by the material-dependent electron-phonon interaction [1] (symbolically represented by the lower inset of Fig. 6.1). With decreasing bath temperature the number of thermal quasiparticle excitations available for recombination reduces, and consequently the recombination time increases exponentially. There is however a discrepancy between this theory and experiments performed at low temperatures [2]. We have found that the relaxation saturates at low temperatures in both Ta and Al, indicating the presence of a second physical process which dominates low temperature relaxation. The energy flux in hot electron experiments suggests the same pattern [3].

In the normal state it has become clear that a dilute concentration of magnetic atoms significantly enhances the inelastic scattering among quasiparticles [4, 5]. In a superconductor the magnetic moment of the impurity leads to time-reversal symmetry breaking by spin-flip scattering, altering the superconducting state. The critical temperature T_c and energy gap Δ decrease with increasing impurity concentration [6]. Depending on the magnetic atom and the host, localized impurity bound states as well as a band of states within the energy gap can appear [7, 8, 9]. In order to test the influence of magnetic impurities on the inelastic interaction in superconducting films we have implanted both magnetic and nonmagnetic atoms and measured the relaxation times at temperatures far below the critical temperature.

6.2 Ta and Al superconducting resonators

We use the complex conductivity $\sigma_1 - i\sigma_2$ to probe the superconducting state. The real part, σ_1, reflects the conduction by quasiparticles while the imaginary part, σ_2, arises from the accelerative response of the Cooper pairs, controlling the high frequency (ω) response of the superconductor [10]. The restoration of the equilibrium state is measured by sensing the complex conductivity while applying an optical photon pulse. To this end, the superconducting film is patterned into planar quarter and half wavelength resonators, comprised of a meandering coplanar waveguide (CPW) with a central line, 3 μm wide, and metal slits, 2 μm wide, see upper inset Fig. 6.1, for details see Refs. [2, 11]. The condensate gives

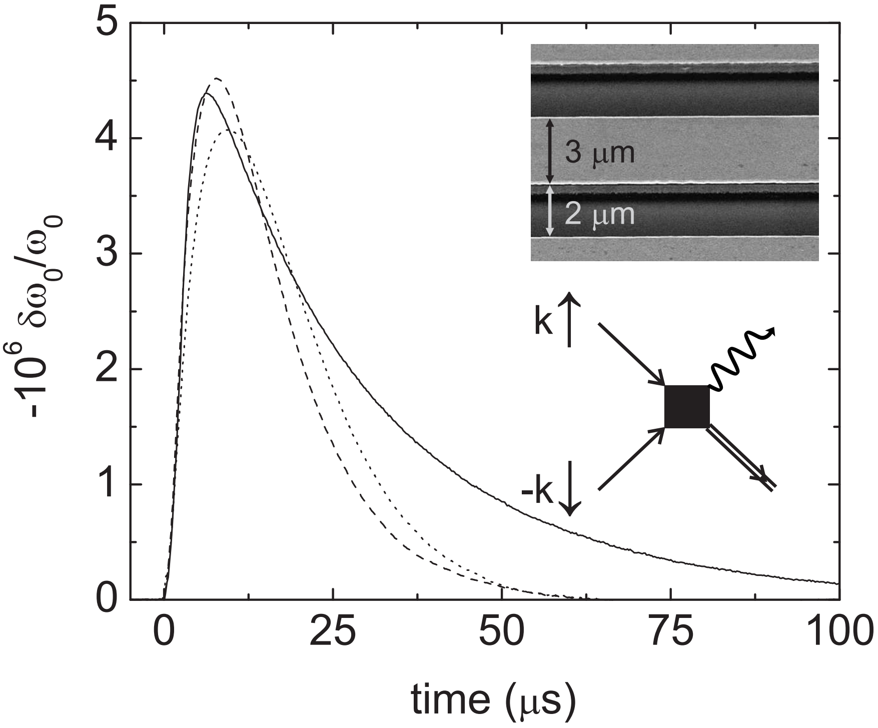

Figure 6.1: The evolution of the resonance frequency in response to an optical pulse (2 μs duration) of a Ta sample (solid line), Ta implanted with 100 ppm Mn (dashed) and 100 ppm Ta (dotted) (average of 100 traces). The initial rise is due to the response time of the resonator, the subsequent exponential decay (Ta: τ=28 μs , Ta with Mn: τ=11 μs, Ta with Ta: τ=11 μs) reflects the recovery of the equilibrium state (Eq. 6.1). The relaxation is due to recombination of quasiparticles into Cooper pairs (depicted in the lower inset). A scanning electron micrograph of the coplanar waveguide geometry of the resonator is shown in the upper inset, the width of the central line is 3 μm and the width of the slits is 2 μm.

rise to a kinetic inductance $L_k \sim 1/d\omega\sigma_2$, with d the thin film thickness, which controls the resonance frequency: $\omega_0 = 2\pi/4l\sqrt{(L_g + L_k)C}$ for a quarterwave resonator with length l, L_g the geometric inductance and C the capacitance per unit length. Lengths of several millimeters are used, corresponding to resonance frequencies of typically 3-6 GHz. The resonators are capacitively coupled to a feedline. Upon optical excitation the complex conductivity reflects the change in the quasiparticle density n_{qp} by: $\delta\sigma_2/\sigma_2 = -\frac{1}{2}\delta n_{qp}/n_{cp}$, with n_{cp} the Cooper pair density ($n_{qp} \ll n_{cp}$). The resonance frequency directly senses the variation in the superconducting state,

$$\frac{\delta\omega_0}{\omega_0} = \frac{\alpha}{2}\frac{\delta\sigma_2}{\sigma_2}\Big(f(E), \Delta\Big), \tag{6.1}$$

with $f(E)$ the distribution of quasiparticles over the energy and α the fraction of the kinetic to total inductance.

The resonators are made from Ta and Al. The Ta film, 280 nm thick, is sputter-deposited onto a hydrogen passivated, high resistivity ($>$ 10 kΩcm) (100)-oriented Si substrate. A 6 nm Nb seed layer is used underneath the Ta layer to promote growth of the desired body-centered-cubic phase [12]. The film critical temperature is 4.4 K, the low temperature resistivity (ρ) is 8.8 $\mu\Omega$cm and the residual resistance ratio (RRR) is 3.2. The Al film, with a thickness of 100 nm, is sputtered onto a similar Si substrate (T_c=1.2 K, ρ=0.81 $\mu\Omega$cm and RRR=4.5). Patterning is done using optical lithography, followed by reactive ion etching for Ta and wet etching for Al. After patterning various concentrations of Mn, as magnetic atom, and Ta and Al have been ion-implanted. The Ta film has been implanted with Mn, Ta and Al at energies of 500, 500 and 250 keV respectively, and the Al film has been implanted with Mn and Al at 60 and 30 keV, to place the peak of the concentration near the middle of the film [13]. The Ta samples are placed on a He-3 sorption cooler in a He-4 cryostat, with the sample space surrounded by a superconducting magnetic shield. The Al samples are placed on an adiabatic demagnetization refrigerator; here a superconducting and cryoperm shield are used. The optical pulse is provided by a GaAsP (1.9 eV) LED, which is fibre-optically coupled to the sample box. The transmission of the feedline near the resonance frequency is sensed using a signal generator, low noise amplifier and quadrature mixer, allowing for monitoring the resonance frequency in the time domain [2, 11].

6.3 Enhancement of low temperature recombination

Typical optical pulse responses are shown in Fig. 6.1 for Ta quarterwave resonators at the base temperature of 325 mK. The exponential decrease reflects the restoration of equilibrium in the superconducting state. The initial rise is due to the response time of the resonator. The faster decay indicates a faster relaxation for implanted Ta samples. The temperature dependence of the relaxation times is shown in Fig. 6.2 for Ta samples implanted with a range of concentrations from 0 to 100 ppm Mn, and with 100 ppm Ta and Al. At low temperatures a clear trend of a *decreasing* relaxation time with *increasing* impurity concentration is visible, both for samples implanted with Mn as well as with Ta and Al. Below $T/T_c \sim 0.1$ the relaxation times become independent of temperature, reaching plateau values of 26 μs for the unimplanted samples,

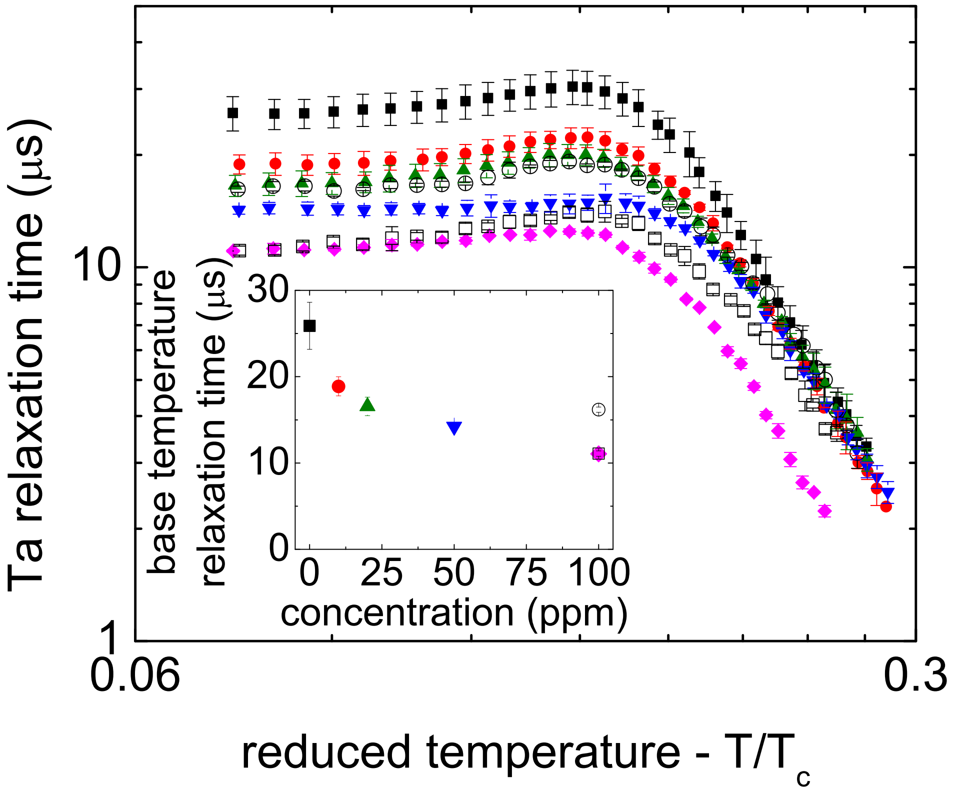

Figure 6.2: The relaxation time as a function of reduced bath temperature in Ta (T_c=4.4 K) with ion-implanted concentrations of Mn: 0 (■), 10 (●), 20 (▲), 50 (▼) and 100 ppm (◆), as well as with 100 ppm Ta (□) and 100 ppm Al (○). The relaxation times at base temperature (325 mK) are plotted in the inset versus ion concentration.

values down to 11 μs for samples implanted with Mn, 11 μs with Ta and 16 μs with Al, clearly decreasing with increasing impurity concentration (see inset). Near $T/T_c \sim 0.15$ the relaxation times reach a peak value in all samples. At high temperatures ($T/T_c \gtrsim 0.2$) we find that the relaxation times increase with decreasing temperature. Here, the relaxation times of the implanted samples, except for the sample with 100 ppm Mn, join with the values of the unimplanted sample, and is understood as due to the conventional electron-phonon process [2]. The critical temperature remains unchanged.

In Al samples, halfwave resonators, implanted with 0 to 100 ppm Mn or 100 ppm Al the relaxation times follow a similar pattern, see Fig. 6.3. The effect of

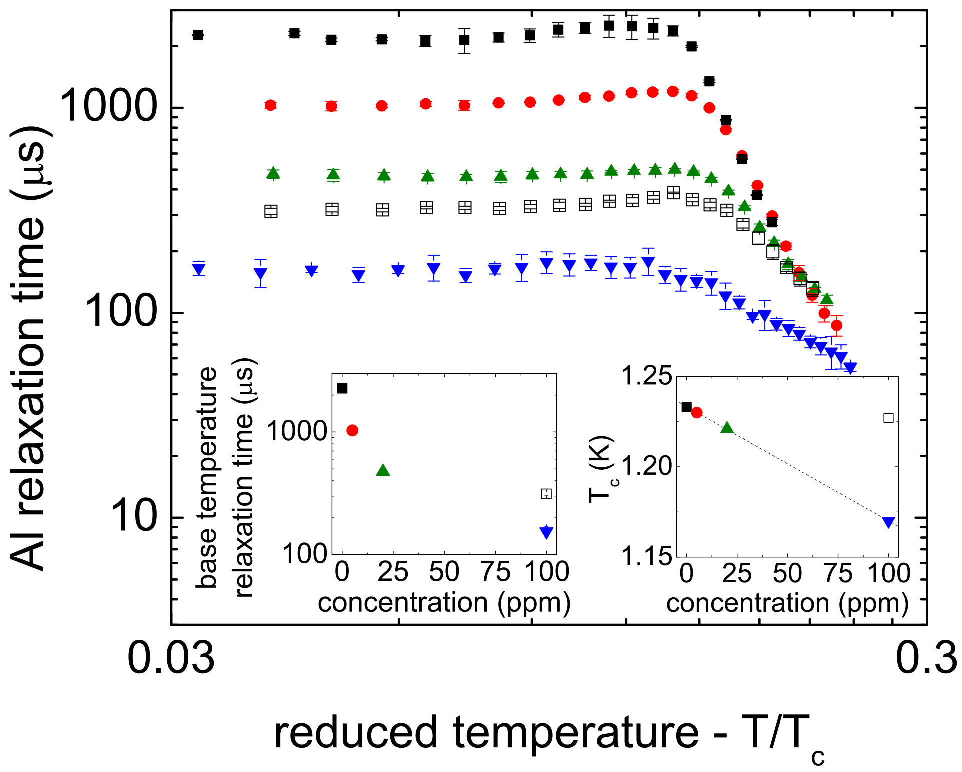

Figure 6.3: The relaxation time as a function of reduced bath temperature in Al with various ion-implanted concentrations of Mn: 0 (■), 5 (●), 20 (▲) and 100 ppm (▼), as well as with 100 ppm Al (□). The left inset shows the relaxation time at base temperature versus ion concentration. The critical temperature decreases only with increasing Mn concentration (right inset).

the implanted impurities is most significant at the lowest temperatures (below $T/T_c \sim 0.1$), where the plateau value of the relaxation time is decreased by an order of magnitude: from a value of 2.3 ms for unimplanted Al down to 320 μs for Al with 100 ppm Al and 150 μs for Al with 100 ppm Mn (see left inset). A slight nonmonotonic temperature dependence is observed for all samples. Above $T/T_c \gtrsim 0.2$ the relaxation times increase with decreasing temperature. In addition, the sample critical temperature decreases linearly with increasing Mn concentration, see right inset of Fig. 6.3, with $\Delta T_c/\Delta c_{\mathrm{Mn}} = -0.63$ mK/ppm (dashed line), while remaining unchanged when implanting Al.

We interpret the relaxation as due to the recombination of quasiparticles near the gap energy: First, we probe σ_2 which is associated with the Cooper pairs. Second, identical relaxation times are found when creating quasiparticle excitations near the gap energy by applying a microwave pulse at the resonance frequency ω_0. In addition, the data are not influenced by quasiparticle outdiffusion as no length dependence was observed in the Al half wavelength resonators, where the central line is isolated from the groundplane, and Ta quarter wavelength resonators used. Moreover, the relaxation time is independent of the photon flux for the small intensities used. Furthermore, the samples are well isolated from thermal radiation: we observe no significant change in relaxation time when varying the temperature of the cryostat or of a blackbody placed next to the sample box. Finally, the significant effect of the implantation of impurities indicates that the relaxation time reflects the restoration of equilibrium in the superconducting films.

The data show a clear trend of decreasing relaxation time in both Ta and Al with an increasing ion-implanted impurity concentration. The significant decrease at the lowest temperatures indicates that the dominant low temperature relaxation channel is enhanced while the relaxation process at higher temperatures is less affected.

6.4 Conventional pair breaking and pair weakening theory

In a superconductor the magnetic nature of the atom depends on the coupling between its spin and the host conduction electrons. Mn has been shown to retain its magnetic moment in Nb, V [14] and Pb [8], acting as pair breaker and giving rise to subgap states. On the other hand, when Mn is placed inside Al $s-d$ mixing occurs: the localized d electron states of the transition metal impurity strongly mix with the conduction band, resulting in the impurity effectively loosing its magnetic moment as well as an increase in the Coulomb repulsion [15]. It acts predominantly as pair weakener: suppressing superconductivity, yet contrary to the case of pair breaking, showing no evidence of subgap states [16].

In order to quantify a possible influence of magnetic impurities on recombination we use the conventional theories by Zittartz, Bringer and Müller-Hartmann [17] and Kaiser [15]. In the presence of pair-breaking impurity bound states develop within the energy gap near reduced energy γ. The quasiparticle excitations, denoted by the Green's function G, and the paired electrons, F, are described by: $E = u(\Delta + \Gamma\frac{\sqrt{1-u^2}}{u^2-\gamma^2})$, with $G(E) = u(E)/\sqrt{u(E)^2-1}$, $F(E) = i/\sqrt{u(E)^2-1}$ and $\Gamma = \hbar/\tau_{sf}$ the pair-breaking parameter. For $\gamma \rightarrow 1$ the Abrikosov-Gorkov

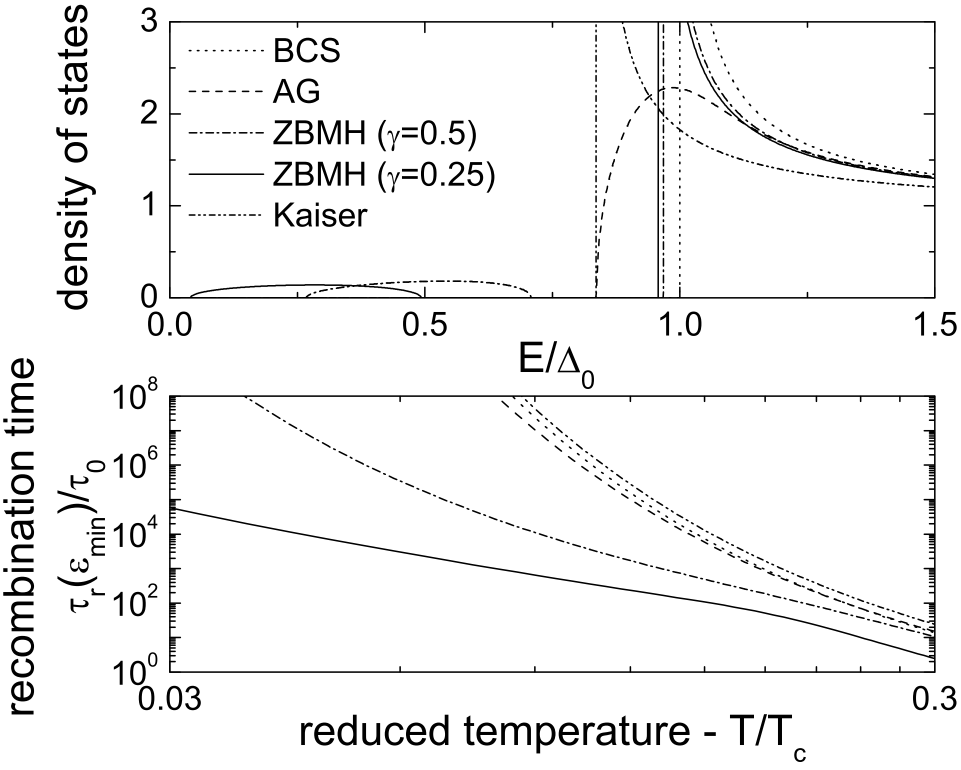

Figure 6.4: Upper figure: Normalized quasiparticle density of states in the presence of magnetic impurities according to pair breaking theories by Abrikosov and Gorkov (AG) as well as Zittartz, Bringer and Müller-Hartmann (ZBMH) (Γ/Δ_0=0.03) and the pair weakening theory by Kaiser (for Δ identical to the AG case). Lower figure: the corresponding recombination times, using Eq. 6.2.

and for $\Gamma \to 0$ the BCS result is recovered. The normalized density of states is $\mathrm{Re}[G(E)]$. The rate of recombination with phonon emission is [1],

$$\begin{aligned}\frac{1}{\tau_r(\epsilon)} = \frac{1}{\tau_0 (kT_{c0})^3[1-f(\epsilon)]}\int_0^\infty (E+\epsilon)^2\Big(\mathrm{Re}[G(E)] \\ + \frac{\Delta}{\epsilon}\mathrm{Im}[F(E)]\Big)[n(E+\epsilon)+1]f(E)dE \quad (6.2)\end{aligned}$$

with τ_0 denoting the material-dependent electron-phonon time, assuming for the electron-phonon spectral function: $\alpha^2F(E) \propto E^2$, and $n(E)$ the phonon distribution function. On the other hand, in the presence of pair-weakening T_c and Δ are reduced simultaneously, and the exponential dependence of the recombination time on T/T_c is retained. In Fig. 6.4, the density of states (upper figure) and the recombination time for quasiparticles at the minimum excitation energy ϵ_{min} (lower figure) are shown for different cases. Clearly, a density of states modified by magnetic impurities results in a recombination time which remains temperature dependent, independent of the model used. A particular model-analysis has recently been performed by Kozorezov *et al.* [18].

6.5 The role of disorder

We conclude that the recombination processes are unrelated to the bulk magnetic moment of the implanted atoms, in agreement with the observation that an enhancement can also be established by implanting nonmagnetic atoms (Figs. 6.1, 6.2 and 6.3). Instead we attribute the enhancement to an increase of the disorder caused by the implantation. Impurities might alter the electron-phonon interaction [19], τ_0 in Eq. 6.2, but no saturation would result [2].

An interesting role of disorder, in particular at the surface, has recently become apparent through phenomena controlled by unpaired magnetic surface spins. An enhancement of the critical current of nanowires has been observed [20], in agreement with theoretical predictions in which surface spins are aligned by the magnetic field [21]. In addition, recent tunneling measurements on niobium surfaces show subgap states, Fig. 6.4, signalling spins at the surface, possibly due to the native oxide [22]. Magnetic moments at surface defects have also been proposed by Koch *et al.* [23] to explain the ubiquitous presence of flux noise in SQUIDs. Sendelbach *et al.* [24] have observed in both Al and Nb SQUIDs a strong dependence of the flux on temperature, which they interpret as due to paramagnetic ordering of surface spins by local fields in the vortex cores. In our recent experiments on the frequency noise of superconducting resonators we also find a strong dependence on the surface properties [25]. In view of the other experiments, we conjecture that in our samples unpaired surface spins are present, whose density is enhanced by the ion bombardment. In order to properly address the relation to the recombination rate, Eq. 6.2 needs to be reanalyzed taking into account spin flip [26], possible spin glass formation [24] and particle-hole asymmetry [7], giving rise to quasiparticles in the ground state [27].

In conclusion, we have measured the relaxation time in Ta and Al superconducting films implanted with both magnetic and nonmagnetic impurities, using the complex conductivity. We find a clear trend of decreasing relaxation time with increasing implanted impurity concentration, independent of their magnetic moment. Our observations show that low temperature quasiparticle recombination is enhanced by disorder, most likely involving the surface.

References

[1] S. B. Kaplan, C. C. Chi, D. N. Langenberg, J. J. Chang, S. Jafarey, and D. J. Scalapino, *Quasiparticle and phonon lifetimes in superconductors*, Phys. Rev. B **14**, 4854 (1976).

[2] R. Barends, J. J. A. Baselmans, S. J. C. Yates, J. R. Gao, J. N. Hovenier, and T. M. Klapwijk, *Quasiparticle relaxation in optically excited high-Q superconducting resonators*, Phys. Rev. Lett. **100**, 257002 (2008).

[3] A. V. Timofeev, C. Pascual García, N. B. Kopnin, A. M. Savin, M. Meschke, F. Giazotto, and J. P. Pekola, *Recombination-Limited Energy Relaxation in a Bardeen-Cooper-Schrieffer* Superconductor, Phys. Rev. Lett. **102**, 017003 (2009).

[4] A. Anthore, F. Pierre, H. Pothier, and D. Esteve, *Magnetic-field-dependent quasiparticle energy relaxation in mesoscopic wires*, Phys. Rev. Lett. **90**, 076806 (2003).

[5] B. Huard, A. Anthore, N. O. Birge, H. Pothier, and D. Esteve, *Effect of magnetic impurities on energy exchange between electrons*, Phys. Rev. Lett. **95**, 036802 (2005).

[6] A. A. Abrikosov and L. P. Gorkov, *Contribution to the theory of superconducting alloys with paramagnetic impurities*, Sov. Phys. JETP **12**, 1243 (1961).

[7] A. Yazdani, B. A. Jones, C. P. Lutz, M. F. Crommie, and D. M. Eigler, *Probing the local effects of magnetic impurities on superconductivity*, Science **275**, 1767 (1997).

[8] W. Bauriedl, P. Ziemann, and W. Buckel, *Electron-Tunneling Observation of Impurity Bands in Superconducting Manganese-Implanted Lead*, Phys. Rev. Lett. **47**, 1163 (1981).

[9] L. Dumoulin, E. Guyon, and P. Nedellec, *Tunneling study of localized bands in superconductors with magnetic impurities (normal Kondo alloys in the superconducting proximity)*, Phys. Rev. B **16**, 1086 (1977).

[10] D. C. Mattis and J. Bardeen, *Theory of the anomalous skin effect in normal and superconducting metals*, Phys. Rev. **111**, 412 (1958).

[11] P. K. Day, H. G. LeDuc, B. A. Mazin, A. Vayonakis, and J. Zmuidzinas, *A broadband superconducting detector suitable for use in large arrays*, Nature **425**, 817 (2003).

[12] D. W. Face and D. E. Prober, *Nucleation of body-centered-cubic tantalum films with a thin niobium underlayer*, J. Vac. Sci. Tech. A **5**, 3408 (1987).

[13] J. F. Ziegler *et al.*, computer code SRIM-2008.01, www.srim.org, 2008.

[14] A. Roy, D. S. Buchanan, D. J. Holmgren, and D. M. Ginsberg, *Localized magnetic moments on chromium and manganese dopant atoms in niobium and vanadium*, Phys. Rev. B **31**, 3003 (1985).

[15] A. B. Kaiser, *Effect of non-magnetic localized states in superconducting alloys*, J. Phys. C **3**, 410 (1970).

[16] G. O'Neil, D. Schmidt, N. A. Miller, J. N. Ullom, A. Williams, G. B. Arnold, and S. T. Ruggiero, *Observation of Nonmagnetic Resonant Scattering Effects by Tunneling in Dilute Al-Mn Alloy Superconductors*, Phys. Rev. Lett. **100**, 056804 (2008).

[17] J. Zittartz, A. Bringer, and E. Müller-Hartmann, *Impurity bands in superconductors with magnetic impurities*, Solid State Comm. **10**, 513 (1972).

[18] A. G. Kozorezov, A. A. Golubov, J. K. Wigmore, D. Martin, P. Verhoeve, R. A. Hijmering, and I. Jerjen, *Inelastic scattering of quasiparticles in a superconductor with magnetic impurities*, Phys. Rev. B **78**, 174501 (2008).

[19] J. Rammer and A. Schmid, *Destruction of phase coherence by electron-phonon interactions in disordered conductors*, Phys. Rev. B **34**, 1352 (1986).

[20] A. Rogachev, T. C. Wei, D. Pekker, A. T. Bollinger, P. M. Goldbart, and A. Bezryadin, *Magnetic-field enhancement of superconductivity in ultranarrow wires*, Phys. Rev. Lett. **97**, 137001 (2006).

[21] M. Yu. Kharitonov and M. V. Feigel'man, *Enhancement of Superconductivity in Disordered Films by Parallel Magnetic Field*, JETP Lett. **82**, 421 (2005).

[22] T. Proslier, J. F. Zasadzinski, L. Cooley, C. Antoine, J. Moore, J. Norem, M. Pellin, and K. E. Gray, *Tunneling study of cavity grade Nb: Possible magnetic scattering at the surface*, Appl. Phys. Lett. **92**, 212505 (2008).

[23] R. H. Koch, D. P. DiVincenzo, and J. Clarke, *Model for 1/f flux noise in SQUIDs and qubits*, Phys. Rev. Lett. **98**, 267003 (2007).

[24] S. Sendelbach, D. Hover, A. Kittel, M. Mück, J. M. Martinis, and R. McDermott, *Magnetism in SQUIDs at millikelvin temperatures*, Phys. Rev. Lett. **100**, 227006 (2008).

[25] R. Barends, H. L. Hortensius, T. Zijlstra, J. J. A. Baselmans, S. J. C. Yates, J. R. Gao, and T. M. Klapwijk, *Contribution of dielectrics to frequency and noise of NbTiN superconducting resonators*, Appl. Phys. Lett. **92**, 223502 (2008).

[26] C. Grimaldi and P. Fulde, *Spin-Orbit Scattering Effects on the Phonon Emission and Absorption in Superconducting Tunneling Junctions*, Phys. Rev. Lett. **77**, 2550 (1996).

[27] M. E. Flatté and J. M. Byers, *Local electronic structure of defects in superconductors*, Phys. Rev. B **56**, 11213 (1997).

Chapter 7

Contribution of dielectrics to frequency and noise of NbTiN superconducting resonators

We study NbTiN resonators by measurements of the temperature dependent resonance frequency and frequency noise. Additionally, resonators are studied covered with SiO_x dielectric layers of various thicknesses. The resonance frequency develops a non-monotonic temperature dependence with increasing SiO_x layer thickness. The increase in the noise is independent of the SiO_x thickness, demonstrating that the noise is not dominantly related to the low temperature resonance frequency deviations.

This chapter is published as R. Barends, H. L. Hortensius, T. Zijlstra, J. J. A. Baselmans, S. J. C. Yates, J. R. Gao and T. M. Klapwijk, Appl. Phys. Lett. **92**, 223502 (2008).

7.1 NbTiN superconducting resonators for probing dielectrics

The interest in the low temperature properties of superconducting resonators for photon detection [1, 2], quantum computation [3, 4] and quasiparticle relaxation experiments [5] increases. In principle these properties are determined by the superconductor, but in practice excess noise and low temperature deviations in the resonance frequency have been observed, which are attributed to dielectrics. It is understood that two-level systems (TLS) in dielectrics in the active region of resonators contribute to limiting the quality factor and phase coherence, cause noise and affect the permittivity ϵ [6, 7, 8, 9]. In order to identify the physical mechanisms through which two-level systems in dielectrics affect the microwave properties of superconducting films, we have chosen to study NbTiN resonators with various coverages of SiO_x. We find that NbTiN follows the Mattis-Bardeen theory for the complex conductivity more closely than any of the other previously used superconductors (Nb, Ta and Al) [10]. We demonstrate that deviations from the ideal superconducting properties can be generated by covering the resonators with a thin amorphous dielectric layer. In addition, we find that this dielectric layer affects the noise and the permittivity differently.

We have made thin film NbTiN coplanar waveguide (CPW) quarter wavelength resonators. The resonator (see lower inset Fig. 7.1) is formed by a central line, 3 μm wide, and slits of 2 μm wide, with a NbTiN film thickness of 300 nm. The resonator is capacitively coupled to the feedline by placing the open end alongside it. The complex conductivity $\sigma_1 - i\sigma_2$, with σ_1 reflecting the conductivity by quasiparticles and σ_2 arising from the accelerative response of the Cooper pair condensate, leads to a kinetic inductance $L_k \propto 1/d2\pi f\sigma_2$ for thin films with thickness d [10, 11]. The resonance frequency is controlled by the kinetic inductance and permittivity, $f_0 = 1/4l\sqrt{(L_g + L_k)C(\epsilon)}$, with l the length of the central line and L_g the geometric inductance and $C \propto \epsilon$ the capacitance per unit length. The resonance frequency is therefore a direct probe for both the complex conductivity and the permittivity,

$$\frac{\delta f_0}{f_0} = \frac{\alpha}{2}\frac{\delta\sigma_2}{\sigma_2} - \frac{F}{2}\frac{\delta\epsilon}{\epsilon}, \tag{7.1}$$

with $\alpha = L_k/(L_g + L_k)$ the kinetic inductance fraction and F a factor which takes into account the active part of the resonator filled with the dielectric, as argued by Gao *et al.* [9]. Resonance frequencies lie between 3-6 GHz. Near the resonance frequency the forward transmission of the feedline S_{21} shows a dip in the magnitude when measured as a function of the microwave frequency f

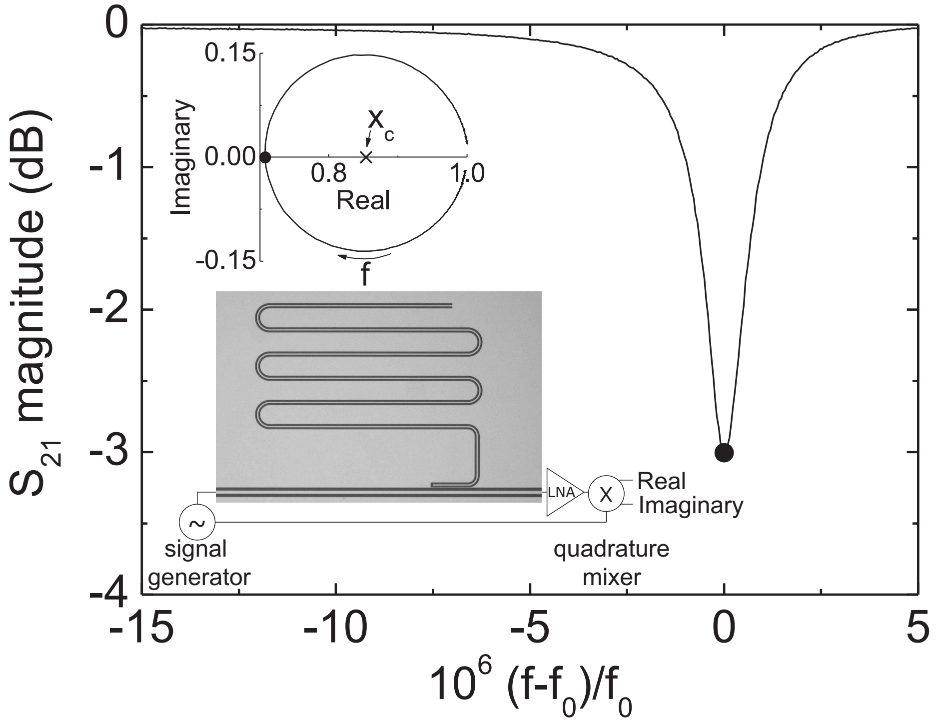

Figure 7.1: The resonance feature appears as a dip in the magnitude and circle in the complex plane (upper inset) of the feedline transmission S_{21}. The quarter wavelength resonator is capacitively coupled to a feedline, formed by the superconducting film (gray) interrupted by slits (black) (lower inset). The loaded quality factor for this NbTiN resonator is $Q_l = 630 \cdot 10^3$, its resonance frequency is $f_0 = 4.47$ GHz. The feedline transmission is measured with a signal generator, low noise amplifier (LNA) and quadrature mixer.

(Fig. 7.1) and traces a circle in the complex plane (upper inset Fig. 7.1). In our experiment we measure both the temperature dependence of f_0 as well as the noise in f_0 in both bare resonators and resonators covered with SiO_x. The combination of these measurements allows us to study the possible correlation between the noise and resonance frequency deviations.

The NbTiN film, 300 nm thick, is deposited by DC magnetron sputtering on a HF-cleaned high resistivity (>1 kΩcm) (100)-oriented silicon substrate. Patterning is done using optical lithography and reactive ion etching in a SF_6/O_2 plasma. The critical temperature is T_c=14.8 K, the low temperature resistivity is ρ=170 $\mu\Omega$cm and the residual resistance ratio is 0.94. After patterning we have covered several samples with a 10, 40 and 160 nm thick SiO_x layer, RF sputtered from a SiO_2 target and x is expected to be close to 2. Three chips are partly covered with SiO_x, i.e. each chip contains both fully covered and uncovered resonators, the latter serving as reference, and a fourth chip is kept uncovered. Measurements are done using a He-3 sorption cooler in a cryostat, with the sample space surrounded by a superconducting magnetic shield. The complex transmission S_{21} is measured by applying a signal along the feedline and amplifying and mixing it with a copy of the original signal in a quadrature mixer, whose outputs are proportional to the real and imaginary parts of S_{21} (lower inset Fig. 7.1). We find quality factors in the order of 10^6.

7.2 Contribution of dielectrics to frequency and noise

The temperature dependence of the resonance frequency is shown in Fig. 7.2 down to a temperature of 350 mK. The data shown is representative for all samples. NbTiN (squares) closely follows the theoretical expression for the complex conductivity (solid line) [10] (inset Fig. 7.2 and main figure), provided a broadening parameter of $\Gamma = 17$ μeV is included in the density of states, following the approach in Ref. [12]. We find a kinetic inductance fraction of $\alpha = 0.35$, from which we infer a magnetic penetration depth of $\lambda = 340$ nm [13]. The resonance frequency decreases monotonically with increasing bath temperature. For both 150 nm Ta on Si (open squares) ($T_c = 4.43$ K) and 100 nm thick Nb on Si (open circles) ($T_c = 9.23$ K), the resonance frequency increases with increasing temperature at low temperatures, displaying a non-monotonic temperature dependence over the full range. Bare NbTiN is in this respect different from Ta and Nb. However, the NbTiN samples covered with a 10 nm (circles), 40 nm (triangles pointing upwards) and 160 nm (triangles pointing downwards) SiO_x layer exhibit a non-monotonicity in the resonance frequency temperature dependence, an effect stronger in samples with thicker layers.

The data in Fig. 7.2 clearly demonstrate that a non-monotonic resonance frequency temperature dependence, similarly to what we find for Ta and Nb samples and for samples of Al on Si [14], and what has been reported for Nb on sapphire samples [9], can be created in NbTiN by covering the samples with SiO_x. SiO_x is an amorphous dielectric and contains a large amount of defects [15], giving rise to two-level systems having a dipole moment, which affect the high frequency properties [16, 17]. At low temperatures the resonant interaction

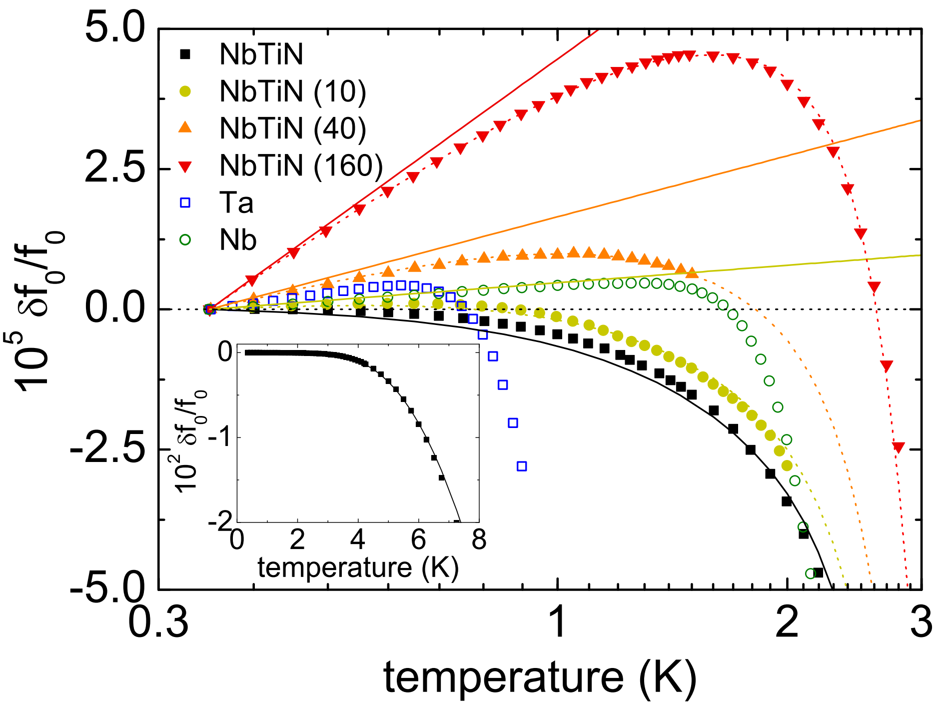

Figure 7.2: The temperature dependence of the resonance frequency of NbTiN samples with no coverage, NbTiN samples with a 10 nm, 40 nm or 160 nm thick SiO_x coverage, and samples of Ta and Nb. The solid lines are fits of the low temperature data to Eq. 7.2. The inset shows the temperature dependence of the resonance frequency of a NbTiN sample over a broader temperature range which closely follows Mattis-Bardeen theory (solid line) [10]. The superposition of the Mattis-Bardeen theory (solid line) and fits to the logarithmic temperature dependence found in data of covered samples (solid lines) yields the dotted lines (Eq. 7.1).

of the dipole two-level systems with the electric fields dominates and leads to a temperature dependent permittivity (in the limit $kT > hf$) [7],

$$\frac{\delta\epsilon}{\epsilon} = -\frac{2p^2P}{\epsilon}\ln\left(\frac{T}{T_0}\right), \tag{7.2}$$

with p the dipole moment, P the density of states and T_0 an arbitrary reference temperature (here we choose T_0 equal to the base temperature of 350 mK). At low temperatures the resonance frequency increases logarithmically with increasing temperature, indicated by the solid lines in Fig. 7.2. The slope of the logarithmic increase scales linearly with the SiO_x thickness. The superposition of

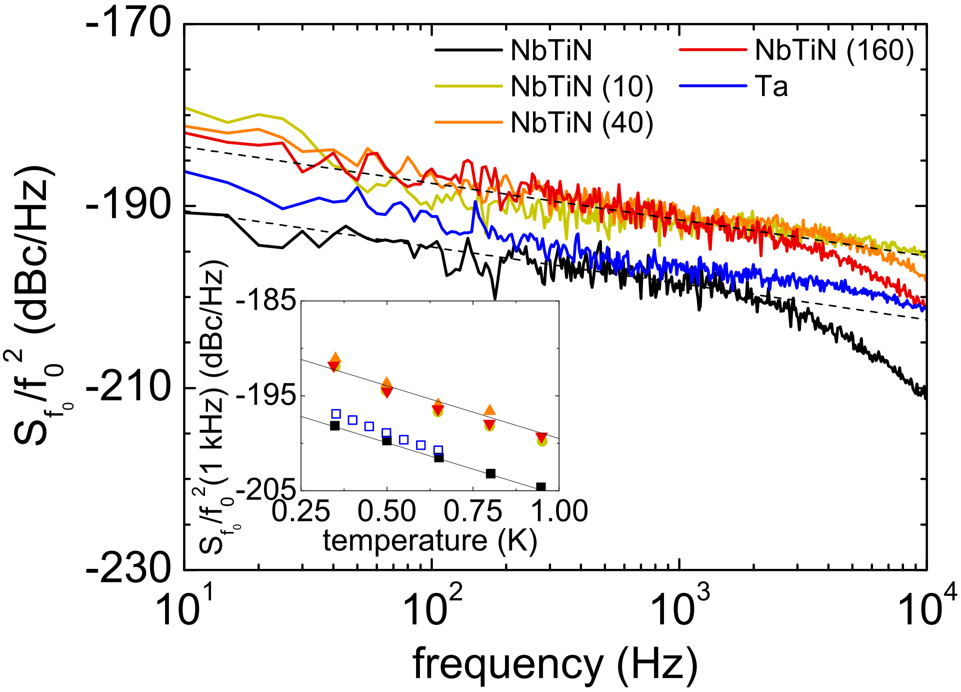

Figure 7.3: Noise spectra of the normalized frequency for NbTiN samples without and with a 10, 40 or 160 nm thick SiO$_x$ layer as well as for Ta. The bath temperature is 350 mK and the internal resonator power is $P_{int} \approx -30$ dBm (standing wave amplitude $V_{rms} \approx 14$ mV). The dashed lines are fits to the spectral shape, $S_{f_0}/f_0^2 \propto f^{-0.4}$. The inset shows the temperature dependence of the noise spectra at 1 kHz (see legend Fig. 7.2).

the complex conductivity (solid line) and the fits to the logarithmic temperature dependence (Eq. 7.2) closely describes the observed resonance frequency (Eq. 7.1, dotted lines). The logarithmic temperature dependence and the thickness scaling indicate that dipole two-level systems distributed in the volume of the SiO$_x$ affect the permittivity. At higher temperatures the complex conductivity dominates, leading to a decrease of the resonance frequency.

In the second experiment we have measured the normalized frequency noise spectra S_{f_0}/f_0^2 of bare NbTiN and Ta samples and NbTiN samples with various SiO$_x$ coverages (Fig. 7.3). The noise is measured by converting the complex transmission at the resonance frequency into a phase $\theta = \arctan[\mathrm{Im}(S_{21})/(x_c - \mathrm{Re}(S_{21}))]$ with x_c the midpoint of the resonance circle (see upper inset Fig. 7.1).

The frequency is related to the phase by: $\theta = -4Q_l \frac{\delta f_0}{f_0}$, with Q_l the resonator loaded quality factor. The power spectral density is calculated by: $S_{f_0}/f_0^2 = S_\theta/(4Q_l)^2$. The noise spectra of samples of NbTiN, and NbTiN with a 10 nm, 40 nm and 160 nm thick SiO_x layer follow $S_{f_0}/f_0^2 \propto f^{-0.4}$ (dashed) until a roll-off at a frequency in the order of 10 kHz. The roll-off is due to the resonator-specific response time and is a function of the loaded quality factor and resonance frequency. We find that the noise is significantly increased by approximately 7 dBc/Hz as soon as the samples are covered by SiO_x and that this increase is independent of the further increase in SiO_x layer thickness. This behavior persists with increasing temperature, where the noise decreases (inset Fig. 7.3), consistent with recent observations for Nb [18].

These measurements clearly show that the increase in the noise is independent of the SiO_x layer thickness, whereas the change in resonance frequency is thickness dependent. It has recently been argued, in independent work [9, 19], that the dielectric influences *both* the resonance frequency and the noise through the capacitance. In this work we have demonstrated that indeed the resonance frequency is controlled by the bulk of the dielectric. However, the observed noise enhancement appears due to the interface. The latter suggests that it is related to quasiparticle trapping and release at the interface, influencing the inductance rather than the capacitance. We find that the noise of NbTiN samples covered with SiO_x has a spectral shape and temperature dependence which is very comparable to the noise of NbTiN samples without coverage and also of Ta samples. In addition, the noise of NbTiN and Ta samples is very similar, while the temperature dependence of the resonance frequency is significantly different. This points towards an interpretation of the noise in terms of inductance fluctuations.

In summary, we conclude that the frequency noise and the low temperature deviations in the resonance frequency of planar superconducting resonators are differently dependent on two-level systems in dielectrics. Using NbTiN samples and introducing dipole two-level systems by covering the samples with various SiO_x layer thicknesses we find that the logarithmic temperature dependent increase in the resonance frequency scales with the layer thickness. The frequency noise increases strongly as soon as a SiO_x layer is present and is, in contrast to the resonance frequency results, thickness independent.

References

[1] P. K. Day, H. G. LeDuc, B. A. Mazin, A. Vayonakis, and J. Zmuidzinas, *A broadband superconducting detector suitable for use in large arrays*, Nature **425**, 817 (2003).

[2] K. W. Lehnert, K. D. Irwin, M. A. Castellanos-Beltran, J. A. B. Mates, and L. R. Vale, *Evaluation of a microwave SQUID multiplexer prototype*, IEEE Trans. Appl. Sup. **17**, 705 (2007).

[3] A. Wallraff, D. I. Schuster, A. Blais, L. Frunzio, R. S. Huang, J. Majer, S. Kumar, S. M. Girvin and R. J. Schoelkopf, *Strong coupling of a single photon to a superconducting qubit using circuit quantum electrodynamics*, Nature **431**, 162 (2004).

[4] A. Palacios-Laloy, F. Nguyen, F. Mallet, P. Bertet, D. Vion, and D. Esteve, *Tunable resonators for quantum circuits*, J. Low Temp. Phys. **151**, 1034 (2008).

[5] R. Barends, J. J. A. Baselmans, S. J. C. Yates, J. R. Gao, J. N. Hovenier, and T. M. Klapwijk, *Quasiparticle relaxation in optically excited high-Q superconducting resonators*, Phys. Rev. Lett. **100**, 257002 (2008).

[6] J. M. Martinis, K. B. Cooper, R. McDermott, M. Steffen, M. Ansmann, K. D. Osborn, K. Cicak, S. Oh, D. P. Pappas, R. W. Simmonds, and C. C. Yu, *Decoherence in Josephson Qubits from Dielectric Loss*, Phys. Rev. Lett. **95**, 210503 (2005).

[7] W. A. Phillips, *Two-level states in glasses*, Rep. Prog. Phys. **50**, 1657 (1987).

[8] J. Gao, J. Zmuidzinas, B. A. Mazin, H. G. LeDuc, and P. K. Day, *Noise properties of superconducting coplanar waveguide microwave resonators*, Appl. Phys. Lett. **90**, 102507 (2007).

[9] J. Gao, M. Daal, A. Vayonakis, S. Kumar, J. Zmuidzinas, B. Sadoulet, B. A. Mazin, P. K. Day, and H. G. LeDuc, *Experimental evidence for a surface distribution of two-level systems in superconducting lithographed microwave resonators*, Appl. Phys. Lett. **92**, 152505 (2008).

[10] D. C. Mattis and J. Bardeen, *Theory of the anomalous skin effect in normal and superconducting metals*, Phys. Rev. **111**, 412 (1958).

[11] M. Tinkham, *Introduction to Superconductivity* (McGraw-Hill, New York, 1996).

[12] R. C. Dynes, V. Narayanamurti, and J. P. Garno, *Direct Measurement of Quasiparticle-Lifetime Broadening in a Strong-Coupled Superconductor*, Phys. Rev. Lett. **41**, 1509 (1978).

[13] J. C. Booth and C. L. Holloway, *Conductor Loss in Superconducting Planar Structures: Calculations and Measurements*, IEEE Trans. Micr. Theory Tech. **47**, 769 (1999).

[14] J. J. A. Baselmans, S. J. C. Yates, R. Barends, Y. J. Y. Lankwarden, J. R. Gao, H. F. C. Hoevers, and T. M. Klapwijk, *Noise and sensitivity of aluminum kinetic inductance detectors for sub-mm astronomy*, J. Low Temp. Phys. **151**, 524 (2008).

[15] D. L. Griscom, *Defect structure of glasses - some outstanding questions in regard to vitreous silica*, J. Non-Crystalline Solids **73**, 51 (1985).

[16] B. Golding, M. von Schickfus, S. Hunklinger, and K. Dransfeld, *Intrinsic electric dipole moment of tunneling systems in silica glasses*, Phys. Rev. Lett. **43**, 1817 (1979).

[17] M. von Schickfus and S. Hunklinger, *Dielectric coupling of low-energy excitations in vitreous silica to electromagnetic waves*, J. Phys. C: Solid State Phys. **9**, L439 (1976).

[18] S. Kumar, J. Gao, J. Zmuidzinas, B. A. Mazin, H. G. LeDuc, and P. K. Day, *Temperature dependence of the frequency and noise of superconducting coplanar waveguide resonators*, Appl. Phys. Lett. **92**, 123503 (2008).

[19] J. Gao, M. Daal, J. M. Martinis, A. Vayonakis, J. Zmuidzinas, B. Sadoulet, B. A. Mazin, P. K. Day, and H. G. LeDuc, *A semiempirical model for two-level system noise in superconducting microresonators*, Appl. Phys. Lett. **92**, 212504 (2008).

Chapter 8

Noise in NbTiN, Al and Ta superconducting resonators on silicon and sapphire substrates

We present measurements of the frequency noise and resonance frequency temperature dependence in planar superconducting resonators on both silicon and sapphire substrates. We show, by covering the resonators with sputtered SiO_x layers of different thicknesses, that the temperature dependence of the resonance frequency scales linearly with thickness, whereas the observed increase in noise is independent of thickness. The frequency noise decreases when increasing the width of the coplanar waveguide in NbTiN on hydrogen passivated silicon devices, most effectively by widening the gap. We find up to an order of magnitude more noise when using sapphire instead of silicon as substrate. The complete set of data points towards the noise being strongly affected by superconductor-dielectric interfaces.

This chapter is published as R. Barends, H. L. Hortensius, T. Zijlstra, J. J. A. Baselmans, S. J. C. Yates, J. R. Gao, and T. M. Klapwijk, accepted for publication in IEEE Trans. on Appl. Supercond. (2009).

8.1 Introduction

Superconducting resonators are becoming increasingly attractive for photon detection [1] as well as for quantum computation [2]. Devices work well, showing quality factors in the order of 10^6 [3], and exhibiting quasiparticle relaxation times among the longest observed [4, 5], allowing for background limited photometry. Presently we reach an electrical noise equivalent power (NEP) as low as $6 \cdot 10^{-19}$ W/$\sqrt{\mathrm{Hz}}$ with Al resonators [6]. However, these resonators have ubiquitously been found to generate significant frequency noise, irrespective of superconducting materials or substrates [7, 8]. The frequency noise is observed to exhibit very comparable properties in all samples used: showing a $1/f^{\sim 0.4}$ spectrum (Fig. 8.1), decreasing with applied microwave power, following $1/P^{0.5}$, and decreasing with bath temperature, with $1/T^{1.1}$ [8] or $1/T^{1.7}$ [9]. The noise is a major issue for low temperature applications and determines further gains in the sensitivity of kinetic inductance photon detectors.

In independent work low temperature non-monotonic deviations in the resonance frequency temperature dependence [10] and frequency noise [11] have been observed in Nb on sapphire resonators. These results have been interpreted to arise from dipole two-level systems in dielectrics in the active region of the resonator, which couple to the electric fields; the experimental data point towards two-level systems distributed either on the surfaces of the superconducting film and/or on the surface of the exposed substrate in the gaps. In the proposed interpretation the low temperature resonance frequency deviations with temperature are coupled to the noise, supported by the width scaling of the noise and resonance frequency deviations with temperature [10, 11]. However, the various processes arising in the volume of the thin surface layer or in the interface between the superconductor and surface layer may contribute differently to the noise and/or the resonance frequency variations with temperature.

8.2 Contribution of dielectric coverage

Recently, we have measured the noise and temperature dependent resonance frequency in NbTiN superconducting resonators covered with a 10, 40 or 160 nm thick amorphous dielectric SiO_x layers [8]; the sample chips contain both fully covered, i.e. both the superconducting film and the gaps, and fully uncovered resonators. The nearby part of the feedline was covered or kept uncovered as well. We find that the noise jumps to a higher level as soon as the samples are covered with SiO_x, independent of the layer thickness, see Fig. 8.1. Additionally, the deviations in the resonance frequency grow linearly with increasing layer thickness,

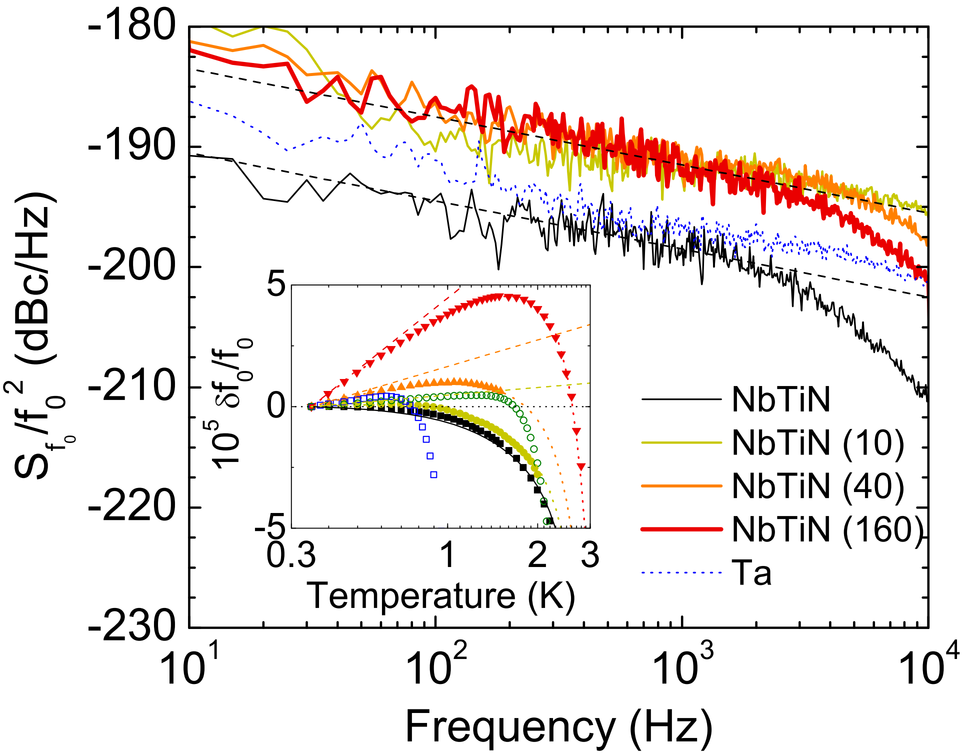

Figure 8.1: Noise spectra of the normalized frequency for NbTiN samples without and with a 10, 40 or 160 nm thick SiO$_x$ layer as well as for Ta at a bath temperature of 350 mK. The dashed lines are fits to the spectral shape, $S_{f_0}/f_0^2 \propto f^{-0.4}$. The inset shows the temperature dependence of the resonance frequency of the same NbTiN samples, uncovered (■) and covered with a 10 (●), 40 (▲) or 160 nm (▼) layer, and Ta (□) and Nb (○). The resonance frequency of the uncovered resonator closely follows the Mattis - Bardeen theory (solid line) [16]. For increasing SiO$_x$ thickness a logarithmic temperature dependence develops (dashed lines). The superposition of these two temperature dependencies (dotted lines) closely describes the data. Figure reproduced from [8].

exhibiting the expected characteristic logarithmic temperature dependence for dipole two-level systems affecting the permittivity [12], see inset Fig. 8.1. These observations show that the resonance frequency temperature deviations are due to the *volume* of the SiO$_x$, whereas the observed increase in the noise is due to the *interface*. Moreover, separately, the noise level of Ta and uncovered NbTiN is very similar, whereas the resonance frequency temperature dependence is significantly different, showing a clear non-monotonicity for Ta while for uncovered

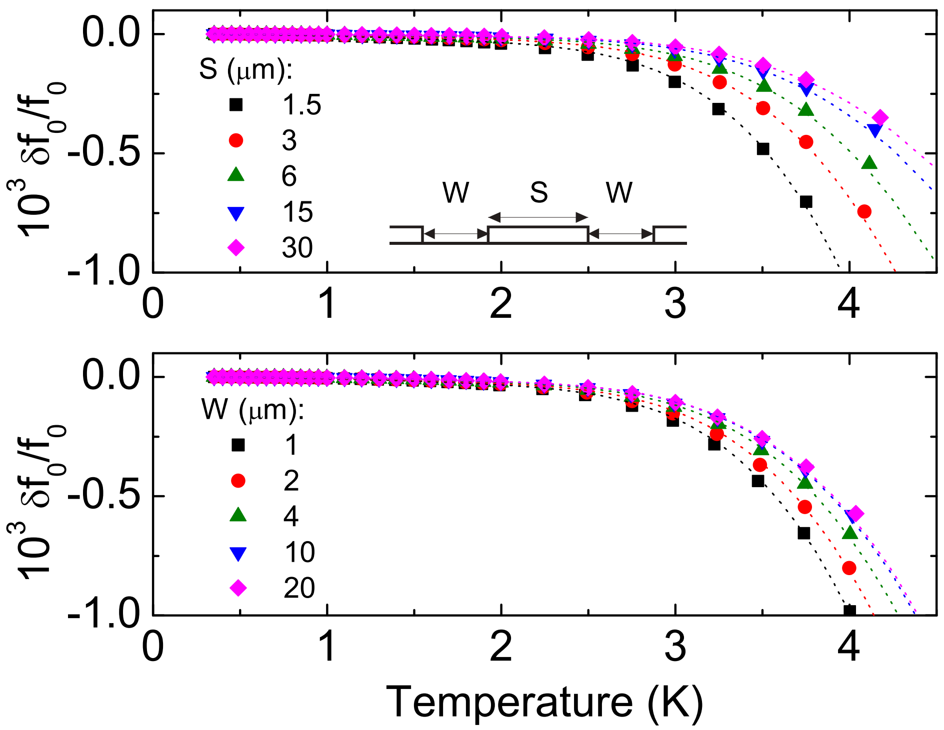

Figure 8.2: The temperature dependence of the resonance frequency of NbTiN on Si resonators for varying central strip width S while keeping $W = 2\ \mu$m (upper figure) and for varying gap width W while keeping $S = 3\ \mu$m (lower figure). The resonance frequency closely follows Mattis-Bardeen theory (dotted lines), Eq. 8.1. The crossection of the CPW geometry is shown in the inset.

NbTiN Mattis-Bardeen theory [16] is followed closely.

The data in Fig. 8.1 support the conjecture that the low temperature resonance frequency deviations are due to dipole two-level systems in the bulk of the dielectric. However, our observations indicate that the noise is differently related to the dielectric coverage. The data point towards the noise being strongly affected by the superconductor-dielectric interfaces. This is supported by measurements by Gao *et al.* [11] on the geometric scaling of the noise in Nb on sapphire resonators, placing the location of the noise source at the interfaces. This however leaves the source of the frequency noise unresolved. In order to elucidate this issue we have performed noise measurements on NbTiN resonators with varying central line widths *or* gap widths. Despite a virtually absent dielectric surface layer, we find a very similar pattern: by increasing the width the noise is reduced; most effectively by widening the gap. Additionally, we find that the noise is increased when using sapphire as substrate instead of Si, indicating that the choice of crystalline substrate affects the frequency noise.

8.3 Experiment

The NbTiN quarter wavelength superconducting resonators consist of a meandering coplanar waveguide (CPW), coupled capacitively by placing the open end alongside the feedline. The resonance frequency is given by: $f_0 = 1/4l \sqrt{(L_g + L_k)C}$, with L_g and C the geometric inductance and capacitance per unit length and l the resonator length. The kinetic inductance L_k arises from the complex conductivity $\sigma_1 - i\sigma_2$ of the superconducting film, for films with arbitrary thickness d: $L_k = \mu_0 \lambda \coth(d/\lambda)$ [13, 14], with $\lambda \propto \sqrt{1/\sigma_2}$ in the dirty limit [15]. The imaginary part σ_2 arises from the accelerative response of the superconducting condensate, while the real part σ_1 reflects conduction by the quasiparticles [16]. The resonance frequency is a probe for the change in the complex conductivity, in the dirty limit

$$\frac{\delta f_0}{f_0} = \frac{\alpha\beta}{4} \frac{\delta\sigma_2}{\sigma_2}, \tag{8.1}$$

with $\alpha = L_k/(L_g + L_k)$ the kinetic inductance fraction and $\beta = 1 + \frac{2d/\lambda}{\sinh(2d/\lambda)}$; for the bulk limit: $\beta = 1$, and for the thin film limit: $\beta = 2$. Near f_0 the feedline transmission shows a dip in the magnitude and a circle in the polar plane [1]. Resonance frequencies used lie between 3-9 GHz.

The NbTiN film, 300 nm thick, is sputter deposited on a high resistivity (>1 kΩcm) hydrogen passivated (HF-cleaned) (100)-oriented Si substrate. The film critical temperature T_c is 14.7 K, the low temperature resistivity ρ is 160 $\mu\Omega$cm and the residual resistance ratio RRR is 0.94. Alternatively, a 300 nm thick NbTiN film is deposited on A-plane sapphire (T_c = 14.8 K, ρ = 150 $\mu\Omega$cm, RRR = 0.98). Patterning is done using optical lithography and reactive ion etching in a SF_6/O_2 plasma. We use central line widths S of 1.5, 3, 6, 15 and 30 μm while keeping the gap width W at 2 μm. Additionally, gap widths W of 1, 2, 4, 10 and 20 μm are used while keeping S = 3 μm. Scanning electron microscope inspection, see inset Fig. 8.4, indicates the etched edges of the NbTiN film to be vertical as desired. In addition, we find that the values for S are approximately 0.5 μm smaller than intended for both films, adding to the values of W. An undercut of roughly 150 nm is present in the NbTiN on Si samples. The samples are placed inside a gold plated Cu sample box, mounted on a He-3 sorption cooler

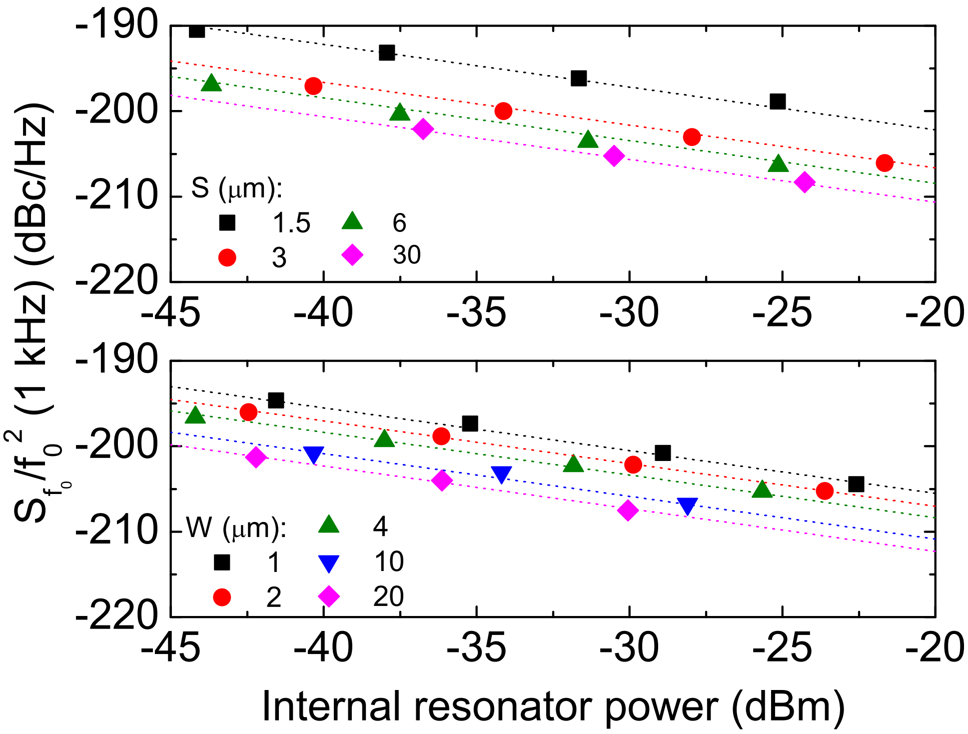

Figure 8.3: The normalized frequency noise at 1 kHz of NbTiN on Si resonators for varying central strip width (upper figure) and varying gap width (lower figure) versus internal resonator power, taking into account the changing impedance of the resonator waveguide (see text). The dotted lines are fits to the power dependence, $S_{f_0}/f_0^2 \propto P_{int}^{-0.5}$. The bath temperature is 350 mK.

inside a cryostat. The sample space is surrounded by a superconducting shield. The feedline transmission is sensed using a signal generator, low noise amplifier and quadrature mixer. The frequency noise is obtained by measuring the feedline transmission at the resonance frequency in the time domain and calculating the power spectral density (for more details see [1, 4, 8]).

8.4 Noise width dependence

The temperature dependence of the resonance frequency for resonators of NbTiN on Si is shown in Fig. 8.2 down to bath temperatures of 350 mK. For increasing temperature the resonance frequency decreases monotonically, following the

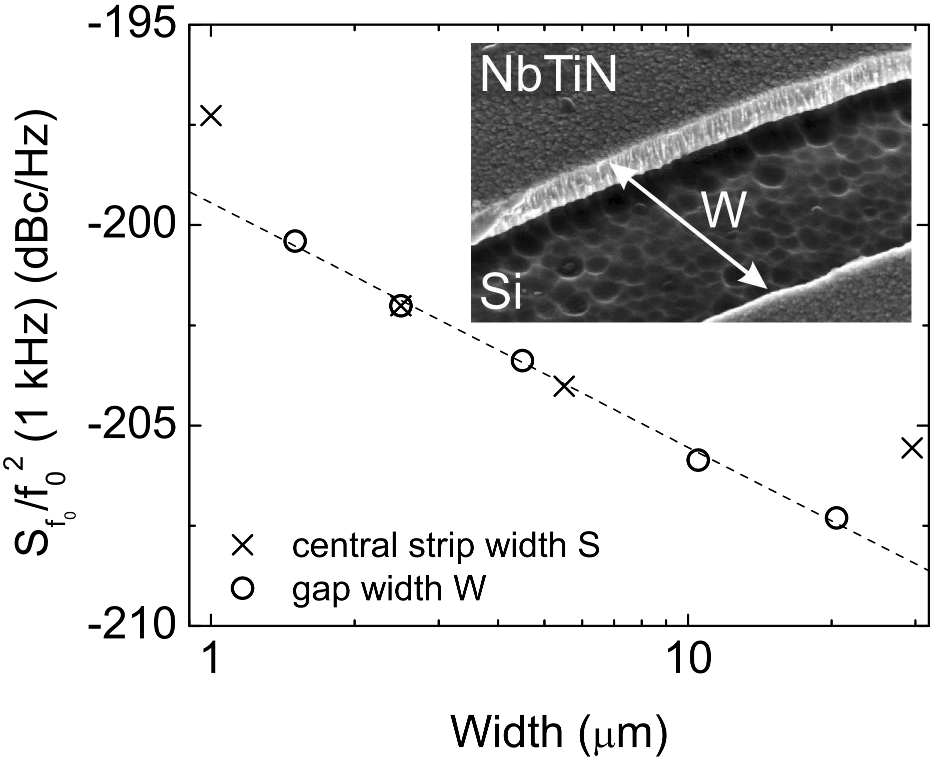

Figure 8.4: The normalized frequency noise at 1 kHz of NbTiN on Si resonators, for varying central strip width S and gap width W. The internal resonator power is $P_{int} = -30$ dBm and the bath temperature is 350 mK. Actual values for the width are determined by scanning electron microscopy. The dashed line is a fit to varying gap data: $S_{f_0}/f_0^2 \propto W^{-0.6}$. The inset is a scanning electron micrograph showing of one of the two gaps of a NbTiN on Si resonator in detail; the gap width of this resonator is close to 1.4 μm.

Mattis-Bardeen expression for the complex conductivity (dotted lines). We include a broadening parameter of $\Gamma = 17$ μeV in the density of states, analogous to [8]. When the central line (above) or the gap (below) are widened, the temperature dependence is less pronounced, indicating a decrease in the kinetic inductance fraction α, see Eq. 8.1. Using the extracted values for α, by fitting the data in Fig. 8.2 to a numerical calculation of the complex conductivity (Eq. 8.1), we find for this film a magnetic penetration depth of $\lambda(0) = 350$ nm [17].

The normalized frequency noise at 1 kHz for varying central strip and gap width is shown in Fig. 8.3 as a function of internal resonator power for samples of

NbTiN on Si. At resonance a standing wave develops inside the resonator, being composed of a forward and backward travelling wave. The internal resonator power associated with this wave is: $P_{int} = \frac{2}{\pi}[Q_l^2/Q_c][Z_{feed}/Z_{res}]P_{read}$, with P_{read} the microwave power applied along the feedline for readout, Q_l and Q_c the loaded and coupler quality factor, and Z the impedance of the feedline, fixed at 50 Ω, or the resonator waveguide. The noise is measured by converting the complex transmission into a phase θ with respect to the resonance circle. This phase reflects the variation in resonance frequency by: $\theta = -4Q_l\frac{\delta f_0}{f_0}$. The normalized frequency noise power spectral density is calculated by: $S_{f_0}/f_0^2 = S_\theta/(4Q_l)^2$, see [8] for further details. The values at 1 kHz are shown in the main figure as a function of internal resonator power. All samples follow $S_{f_0}/f_0^2 \propto P_{int}^{-0.5}$ (dotted lines), consistent with previous measurements [7]. A clear trend of decreasing noise level for increasing width is visible. When increasing the central line width S from 1 to 30 μm the noise is decreased by 8.4 dBc/Hz, whereas widening the gaps from a value of 1.5 to 20 μm decreases the noise by 6.9 dBc/Hz.

The data are summarized in Fig. 8.4, where the noise value at a power level of $P_{int} = -30$ dBm is plotted versus both central strip and gap width. We find that with increasing central strip width the noise first decreases strongly while further increases do not lead to a large reduction of the noise. With widening gap the noise decreases gradually, following the powerlaw: $S_{f_0}/f_0^2 \propto W^{-0.6}$ (dashed line).

8.5 Contribution of substrate

Apart from the influence of the dielectrics at the top surface the interface with the substrate also plays a role. In Fig. 8.5 the frequency noise power spectral density is shown for comparable NbTiN on hydrogen passivated Si and on sapphire resonators, deposited and measured under identical conditions[1]. We find a similar spectral shape for both resonators, following $1/f^{0.4}$ (dashed lines), and a clearly *increased* noise level, by 10 dBc/Hz, when using sapphire instead of Si. A similar pattern is found for Al resonators, see Fig. 8.6. The noise in Al on sapphire resonators is 9 dBc/Hz larger than for Al on HF-cleaned Si, its spectrum following $1/f^{0.45}$ (dashed lines) in both cases. Both Al films have a thickness of 100 nm and a critical temperature of 1.2 K. Interestingly, in NbTiN on sapphire a non-monotonic temperature dependence of the resonance frequency is

---

[1] Additional measurements on the noise show it to be independent of the resonance frequency: a variation of $\sim$ 1 dBc/Hz is observed for NbTiN on sapphire resonators with frequencies from 3 - 9 GHz and identical geometry.

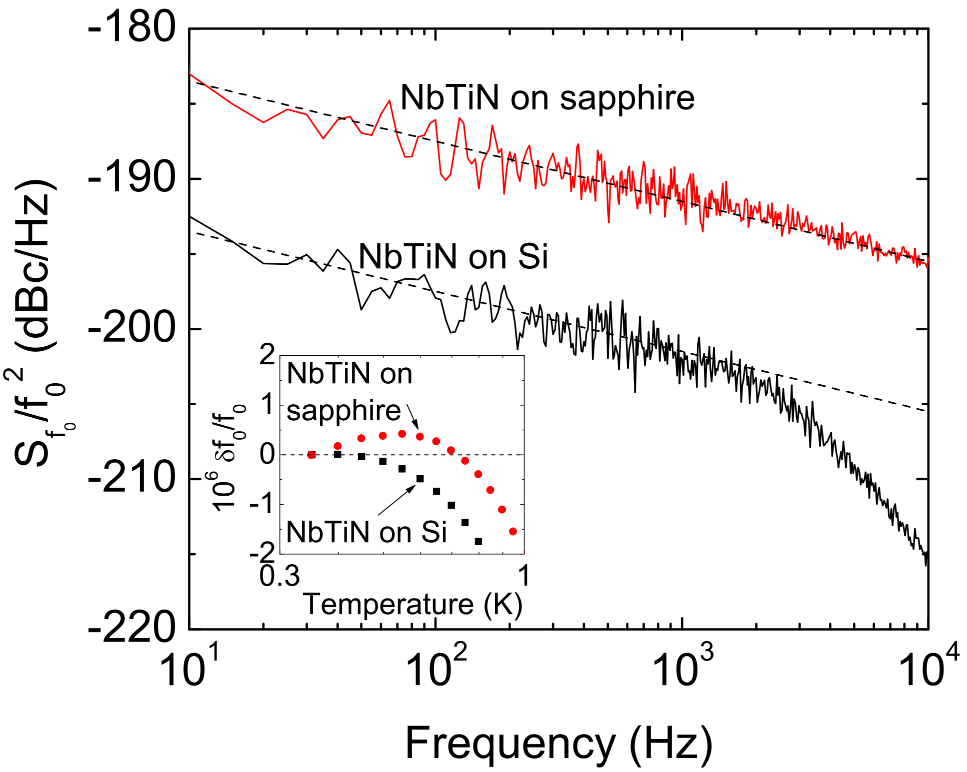

Figure 8.5: The normalized frequency noise spectra of NbTiN on Si and NbTiN on sapphire resonators having the same geometry, S=3 μm, W=2 μm, and resonance frequency, 3.70 GHz and 3.76 GHz respectively, for $P_{int} = -30$ dBm, at a bath temperature of 350 mK. The dashed lines are fits to the spectral shape $S_{f_0}/f_0^2 \propto f^{-0.4}$. The roll-off is due to the resonator-specific response time. The inset shows a monotonic temperature dependence of the resonance frequency for NbTiN on Si (squares) and a non-monotonic one for NbTiN on sapphire (dots).

re-established (inset Fig. 8.5), analogously to covering the NbTiN on Si samples with SiO$_x$ (Fig. 8.1). Moreover, for Al on sapphire resonators the non-monotonic temperature dependence of the resonance frequency is stronger than for Al on Si (inset Fig. 8.6).

These results show that the lowest noise is obtained in NbTiN on hydrogen passivated Si. The non-monotonicity of the resonance frequency indicates the presence of dipole two-level systems, in the bulk or in the interface. Additionally, using sapphire shows an interesting resemblance to covering the NbTiN on Si samples with SiO$_x$ (Fig. 8.1); suggesting by analogy that the superconductor-

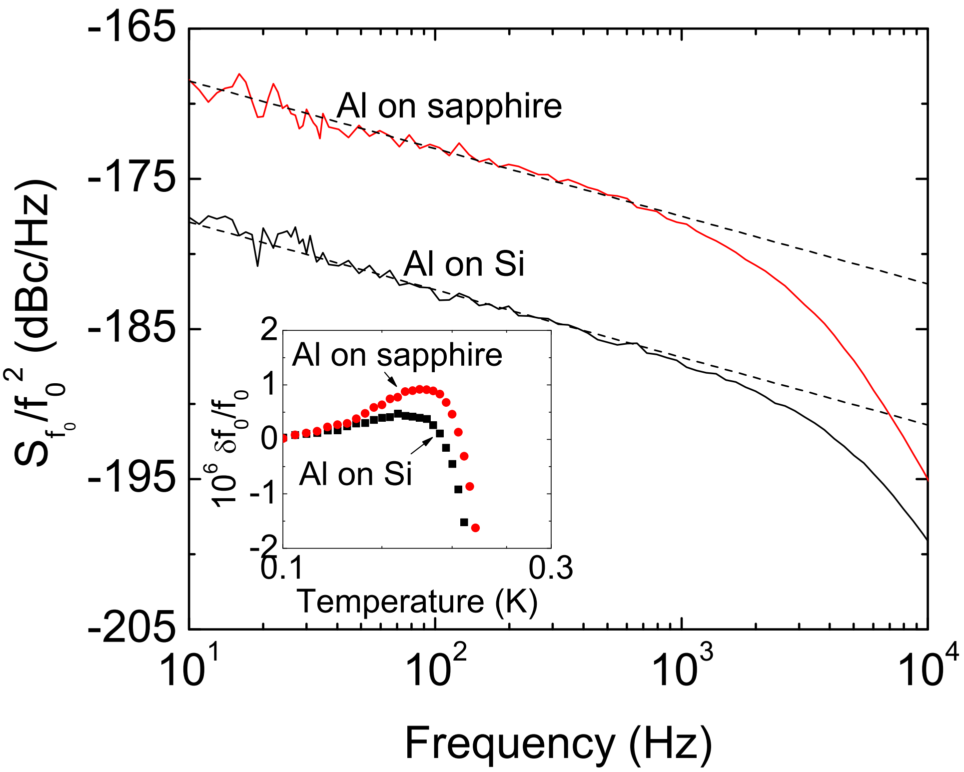

Figure 8.6: The normalized frequency noise spectra of Al on Si and Al on sapphire resonators with equal geometry (S=3 μm, W=2 μm) and similar resonance frequency, 4.22 GHz and 4.57 GHz respectively, for $P_{int} = -40$ dBm, at a bath temperature of 100 mK. The dashed lines are fits to the spectral shape $S_{f_0}/f_0^2 \propto f^{-0.45}$. The roll-off is due to the resonator-specific response time. The inset shows a more pronounced non-monotonicity in the temperature dependence of the resonance frequency for Al on sapphire (dots) compared to Al on Si (squares).

substrate interface contributes to the noise as well (in contrast to the assumption by Bialczak *et al.* [18]). Most importantly, both the effect on the noise of a dielectric layer on top in Fig. 8.1, and the change in substrate as shown in Figs. 8.5 and 8.6 strongly suggest that *superconductor-dielectric interfaces* contribute to the frequency noise.

8.6 Discussion and conclusion

The identification of the source of the frequency noise is reminiscent of experiments on the coherence for quantum information processing with superconductors. Josephson circuits exhibit a poorly understood $1/f$ flux noise. The source of this flux noise is suggested to be related to spins at the surface. The physical mechanism has been conjectured to be due to spins of electrons in interface defect states [19] or due to paramagnetic dangling bonds at interfaces [20]. In this respect the hydrogen passivation of the Si is an important step in reducing these contributions. Recently, the source of the flux noise has been suggested to arise from RKKY (Ruderman-Kittel-Kasuya-Yosida) interactions between electron spins at interfaces of metals [21], supported by measurements on the magnetic properties of SQUIDs indicating the presence of surface spins on superconducting films [22]. In our resonators such interface spins would possibly couple to the magnetic fields inside the resonator active region, appearing in the inductance. Our data appear to be compatible with such a conceptual framework. On the other hand, in recent work [23], connecting an interdigitated capacitor to a transmission line resonator results in a reduction of the noise by 10 dB, indicative of a strong contribution of a noise process located in dielectrics near the superconductor.

To conclude, we find that the frequency noise in coplanar waveguide superconducting resonators and the deviations in the temperature dependence of the resonance frequency are differently dependent on dielectrics, by measurements on NbTiN on Si resonators with various coverages of SiO_x. Additionally, the noise can be decreased by increasing the width of the waveguide. The choice of substrate is crucial for the level of noise, as we observe up to an order of magnitude more noise in resonators comprised of NbTiN and Al on sapphire compared to Si. The data indicate that the noise is strongly affected by superconductor-dielectric interfaces. The source of the frequency noise in resonators, possibly being correlated to the flux noise in Josephson circuits which is associated with recently observed surface spins, is a subject of future experimentation.

References

[1] P. K. Day, H. G. LeDuc, B. A. Mazin, A. Vayonakis and J. Zmuidzinas, *A broadband superconducting detector for use in large arrays*, Nature **425**, 817 (2003).

[2] A. Wallraff, D. I. Schuster, A. Blais, L. Frunzio, R. S. Huang, J. Majer, S. Kumar, S. M. Girvin and R. J. Schoelkopf, *Strong coupling of a single photon to*

a superconducting qubit using circuit quantum electrodynamics, Nature **431**, 162 (2004).

[3] A. Palacios-Laloy, F. Nguyen, F. Mallet, P. Bertet, D. Vion, and D. Esteve, *Tunable resonators for quantum circuits*, J. Low Temp. Phys. **151**, 1034 (2008).

[4] R. Barends, J. J. A. Baselmans, S. J. C. Yates, J. R. Gao, J. N. Hovenier, and T. M. Klapwijk, *Quasiparticle relaxation in optically excited high-Q superconducting resonators*, Phys. Rev. Lett. **100**, 257002 (2008).

[5] R. Barends, S. van Vliet, J. J. A. Baselmans, S. J. C. Yates, J. R. Gao, and T. M. Klapwijk, *Enhancement of quasiparticle recombination in Ta and Al superconductors by implantation of magnetic and nonmagnetic atoms*, Phys. Rev. B **79**, 020509 (2009).

[6] J. J. A. Baselmans, S. J. C. Yates, R. Barends, Y. J. Y. Lankwarden, J. R. Gao, H. F. C. Hoevers, and T. M. Klapwijk, *Noise and sensitivity of aluminum kinetic inductance detectors for sub-mm astronomy*, J. Low Temp. Phys. **151**, 524 (2008); and unpublished results.

[7] J. Gao, J. Zmuidzinas, B. A. Mazin, H. G. LeDuc, and P. K. Day, *Noise properties of superconducting coplanar waveguide microwave resonators*, Appl. Phys. Lett. **90**, 102507 (2007).

[8] R. Barends, H. L. Hortensius, T. Zijlstra, J. J. A. Baselmans, S. J. C. Yates, J. R. Gao, and T. M. Klapwijk, *Contribution of dielectrics to frequency and noise of NbTiN superconducting resonators*, Appl. Phys. Lett. **92**, 223502 (2008).

[9] S. Kumar, J. Gao, J. Zmuidzinas, B. A. Mazin, H. G. LeDuc, and P. K. Day, *Temperature dependence of the frequency and noise of superconducting coplanar waveguide resonators*, Appl. Phys. Lett. **92**, 123503 (2008).

[10] J. Gao, M. Daal, A. Vayonakis, S. Kumar, J. Zmuidzinas, B. Sadoulet, B. A. Mazin, P. K. Day, and H. G. LeDuc, *Experimental evidence for a surface distribution of two-level systems in superconducting lithographed microwave resonators*, Appl. Phys. Lett. **92**, 152505 (2008).

[11] J. Gao, M. Daal, J. M. Martinis, A. Vayonakis, J. Zmuidzinas, B. Sadoulet, B. A. Mazin, P. K. Day, and H. G. LeDuc, *A semiempirical model for two-level system noise in superconducting microresonators*, Appl. Phys. Lett. **92**, 212504 (2008).

[12] W. A. Phillips, *Two-level states in glasses*, Rep. Prog. Phys. **50**, 1657 (1987).

[13] R. L. Kautz, *Picosecond pulses on superconducting striplines*, J. Appl. Phys. **49**, 308 (1978).

[14] W. H. Henkels and C. J. Kircher, *Penetration depth measurements on type II superconductors*, IEEE Trans. Magn. **MAG-13**, 63 (1977).

[15] M. Tinkham, *Introduction to Superconductivity*, (McGraw-Hill, New York, 1996).

[16] D.C. Mattis and J. Bardeen, *Theory of the anomalous skin effect in normal and superconducting metals*, Phys. Rev. **111**, 412 (1958).

[17] J. C. Booth and C. L. Holloway, *Conductor loss in superconducting planar structures: calculations and measurements*, IEEE Trans. Micr. Theory Tech. **47**, 769 (1999).

[18] R. C. Bialczak, R. McDermott, M. Ansmann, M. Hofheinz, N. Katz, E. Lucero, M. Neeley, A. D. OConnell, H. Wang, A. N. Cleland, and J. M. Martinis, *1/f Flux noise in josephson phase qubits*, Phys. Rev. Lett. **99**, 187006 (2007).

[19] R. H. Koch, D. P. DiVincenzo, and J. Clarke, *Model for 1/f flux noise in SQUIDs and qubits*, Phys. Rev. Lett. **98**, 267003 (2007).

[20] R. de Sousa, *Dangling-bond spin relaxation and magnetic* $1/f$ *noise from the amorphous-semiconductor/oxide interface: theory*, Phys. Rev. B **76**, 245306 (2007).

[21] L. Faoro and L. B. Ioffe, *Microscopic origin of low-frequency flux noise in josephson circuits*, Phys. Rev. Lett. **100**, 227005 (2008).

[22] S. Sendelbach, D. Hover, A. Kittel, M. Mück, J. M. Martinis, and R. McDermott, *Magnetism in SQUIDs at millikelvin temperatures*, Phys. Rev. Lett. **100**, 227006 (2008).

[23] O. Noroozian, *New resonator designs for reduced frequency noise in microwave kinetic inductance detectors*, 2nd Workshop on the Physics and Applications of Superconducting Microresonators, SRON Utrecht, the Netherlands, 19-20 June, 2008.

Appendix A

Noise equivalent power

The noise equivalent power (NEP) is defined as the power per post-detection bandwidth *df* = 1 Hz (integration time is 0.5 s) at the detector input with a signal-to-noise ratio of one. In other words, the NEP is the *incident* power at the input that doubles the output, i.e. adds an output signal level identical to the output signal arising from the input noise.

Incident power P leads to an increase of the quasiparticle number

$$\frac{\delta N_{qp}}{\delta t} = \frac{\eta P}{\Delta} - \frac{N_{qp}}{\tau_r} \tag{A.1}$$

with η the absorption efficiency, Δ the superconducting energy gap and τ_r the recombination time. In the steady state, the above equation results in

$$N_{qp} = \frac{\eta \tau_r}{\Delta} P \tag{A.2}$$

Consequently, the response in the observable, the phase θ, is

$$< \theta >= \frac{\delta\theta}{\delta N_{qp}} < N_{qp} > \tag{A.3}$$

Now we can write three identities for $< \theta^2(f) >$

$$< \theta^2(f) > = S_\theta(f)df \tag{A.4}$$

$$= \Big(\frac{\delta\theta}{\delta N_{qp}}\Big)^2 \frac{< N_{qp}^2(f) >}{1 + (2\pi f \tau_{res})^2} = \Big(\frac{\delta\theta}{\delta N_{qp}}\Big)^2 \frac{S_{N_{qp}}(f)df}{1 + (2\pi f \tau_{res})^2} \tag{A.5}$$

$$= \Big(\frac{\delta\theta}{\delta N_{qp}}\Big)^2 \Big(\frac{\eta\tau_r}{\Delta}\Big)^2 \frac{< P^2(f) >}{[1 + (2\pi f \tau_r)^2][1 + (2\pi f \tau_{res})^2]} \tag{A.6}$$

The frequency-dependent part arises from the notion that the resonator (limited by the resonator response time τ_{res}) cannot follow fast variations in the electron system; additionally the electron system (characterised by the relaxation time τ_r)

cannot follow fast variations in the incident power. These timescales give rise to Lorentzian spectral filtering of the noise, see Eq. 2.9.

Using the above Eqs. A.4 and A.6, we can write for the noise equivalent power

$$\begin{aligned} NEP &= \sqrt{\frac{< P^2(f) >}{df}} \\ &= \sqrt{S_\theta(f)}\Big(\frac{\delta\theta}{\delta N_{qp}}\frac{\eta\tau_r}{\Delta}\Big)^{-1}\sqrt{1+(2\pi f\tau_r)^2}\sqrt{1+(2\pi f\tau_{res})^2} \end{aligned} \tag{A.7}$$

For the generation-recombination noise limited NEP, using Eqs. A.4, A.5 and A.7, and for the particle number fluctuations (Eq. 2.10)

$$S_{N_{qp}}(f) = \frac{4N_{qp}\tau_r}{1+(2\pi f\tau_r)^2} \tag{A.8}$$

we can write

$$\begin{aligned} NEP_{G-R} =& \sqrt{\left(\frac{\delta\theta}{\delta N_{qp}}\right)^2 \frac{4N_{qp}\tau_r}{[1+(2\pi f\tau_r)^2][1+(2\pi f\tau_{res})^2]}}\Big(\frac{\delta\theta}{\delta N_{qp}}\frac{\eta\tau_r}{\Delta}\Big)^{-1} \\ & \times \sqrt{1+(2\pi f\tau_r)^2}\sqrt{1+(2\pi f\tau_{res})^2} \\ =& \frac{2\Delta}{\eta}\sqrt{\frac{N_{qp}}{\tau_r}} \end{aligned} \tag{A.9}$$

Using Eqs. 2.2 and 2.6 it can be shown that the generation-recombination noise limited NEP decreases exponentially with decreasing temperature: $NEP_{G-R} \propto e^{-\Delta/kT}$.

Appendix B

Analytical expression for the complex conductivity

Here we derive the analytical expression for the complex conductivity $\sigma_1 - i\sigma_2$, valid for $hf, kT \ll 2\Delta$ (hf can be smaller or larger than kT). The imaginary part is given by [1]

$$\frac{\sigma_2}{\sigma_N} = \frac{1}{hf}\int_{\Delta-hf}^{\Delta}\left[1-2f_{FD}(E+hf)\right]\frac{E(E+hf)+\Delta^2}{\sqrt{(E+hf)^2-\Delta^2}\sqrt{\Delta^2-E^2}}dE \tag{B.1}$$

We rewrite the integral to a modified Bessel function of the first kind, with integer $n \geq 0$ and for $|\arg(z)| < \frac{1}{2}\pi$ the integral representation is [2]

$$I_n(z) = \frac{1}{\pi}\int_0^{\pi} e^{z\cos(\theta)}\cos(n\theta)d\theta \tag{B.2}$$

With $\beta\Delta \gg 1$ ($\beta = 1/kT$) we approximate the Fermi-Dirac distribution with the Maxwell-Boltzmann distribution $f_{FD}(E) \approx e^{-\beta E}$. For the temperature dependent part of the integral, using $E = \Delta + u$ and neglecting higher order terms,

$$\int_{\Delta-hf}^{\Delta} f_{FD}(E+hf)\frac{E(E+hf)+\Delta^2}{\sqrt{(E+hf)^2-\Delta^2}\sqrt{\Delta^2-E^2}}dE \tag{B.3}$$

$$= \int_{\Delta-hf/2}^{\Delta+hf/2} e^{-\beta(E+hf/2)}\frac{E^2+\Delta^2}{\sqrt{E^2+Ehf-\Delta^2}\sqrt{\Delta^2-(E^2-Ehf)}}dE \tag{B.4}$$

$$= \int_{-hf/2}^{hf/2} e^{-\beta(\Delta+u+hf/2)}\frac{2\Delta^2}{\sqrt{2\Delta u+\Delta hf}\sqrt{\Delta hf-2\Delta u}}du \tag{B.5}$$

Substituting $u = xhf/2$

$$\int_{-1}^{1} e^{-\beta(\Delta+hf/2+xhf/2)} \frac{\Delta}{\sqrt{1+x}\sqrt{1-x}} dx \tag{B.6}$$

$$= \Delta e^{-\beta\Delta} e^{-\beta hf/2} \int_{-1}^{1} \frac{e^{-\beta xhf/2}}{\sqrt{1-x^2}} dx \tag{B.7}$$

$$= \Delta e^{-\beta\Delta} e^{-\beta hf/2} \int_{0}^{\pi} e^{+\beta\cos(\theta)hf/2} d\theta \tag{B.8}$$

$$= \Delta e^{-\beta\Delta} e^{-\beta hf/2} \pi I_0 \left(\frac{\beta hf}{2}\right) \tag{B.9}$$

with the substitution $x = -\cos(\theta)$. Using the zero temperature result $\sigma_2/\sigma_N = \pi\Delta/hf$,

$$\frac{\sigma_2}{\sigma_N} = \frac{\pi\Delta}{hf}\left[1 - 2e^{-\Delta/kT} e^{-hf/2kT} I_0\left(\frac{hf}{2kT}\right)\right] \tag{B.10}$$

The real part σ_1 is given by [1]

$$\frac{\sigma_1}{\sigma_N} = \frac{2}{hf}\int_{\Delta}^{\infty} \left[f_{FD}(E) - f_{FD}(E+hf)\right] \frac{E(E+hf)+\Delta^2}{\sqrt{E^2-\Delta^2}\sqrt{(E+hf)^2-\Delta^2}} dE \tag{B.11}$$

We rewrite the integral to a modified Bessel function of the second kind, with integer $n \geq 0$ and for $|\arg(z)| < \frac{1}{2}\pi$ the integral representation is [2]

$$K_n(z) = \frac{\pi^{\frac{1}{2}}(\frac{1}{2}z)^n}{\Gamma(n+\frac{1}{2})} \int_{1}^{\infty} e^{-zt}(t^2-1)^{n-\frac{1}{2}} dt \tag{B.12}$$

For $\beta\Delta \gg 1$ the integral is, using the substitutions $E = \Delta + u$ and $u = xhf/2$

$$\int_{\Delta+hf/2}^{\infty} \left[e^{-\beta(E-hf/2)} - e^{-\beta(E+hf/2)}\right] \frac{E^2+\Delta^2}{\sqrt{E^2-Ehf-\Delta^2}\sqrt{E^2+Ehf-\Delta^2}} dE \tag{B.13}$$

$$= 2\sinh\left(\frac{\beta hf}{2}\right) \int_{\Delta+hf/2}^{\infty} e^{-\beta E} \frac{E^2+\Delta^2}{\sqrt{E^2-Ehf-\Delta^2}\sqrt{E^2+Ehf-\Delta^2}} dE \tag{B.14}$$

$$= 2\sinh\left(\frac{\beta hf}{2}\right) e^{-\beta\Delta} \int_{hf/2}^{\infty} e^{-\beta u} \frac{2\Delta^2}{\sqrt{2\Delta u-\Delta hf}\sqrt{2\Delta u+\Delta hf}} du \tag{B.15}$$

$$= 2\sinh\left(\frac{\beta hf}{2}\right) e^{-\beta\Delta} \int_{1}^{\infty} e^{-\beta xhf/2} \frac{\Delta}{\sqrt{x-1}\sqrt{x+1}} dx \tag{B.16}$$

$$= 2\sinh\left(\frac{\beta hf}{2}\right) \Delta e^{-\beta\Delta} \int_{1}^{\infty} \frac{e^{-\beta xhf/2}}{\sqrt{x^2-1}} dx \tag{B.17}$$

$$= 2\sinh\left(\frac{\beta hf}{2}\right) \Delta e^{-\beta\Delta} K_0\left(\frac{\beta hf}{2}\right) \tag{B.18}$$

Hence,

$$\frac{\sigma_1}{\sigma_N} = \frac{4\Delta}{hf} e^{-\Delta/kT} \sinh\left(\frac{hf}{2kT}\right) K_0\left(\frac{hf}{2kT}\right) \tag{B.19}$$

References

[1] D. C. Mattis and J. Bardeen, *Theory of the anomalous skin effect in normal and superconducting metals*, Phys. Rev. **111**, 412 (1958).

[2] M. Abramowitz and I. A. Segun, *Handbook of mathematical functions*, (Fifth Dover Edition, Dover Publications, New York, 1968).

Appendix C

Noise under continuous illumination

When shining light on a superconducting resonator, the resonance frequency shifts and both the phase and amplitude noise levels increase. The shift in frequency is due to the change in Cooper pair and quasiparticle density. Using Eq. A.1, the amount of excess quasiparticles created by the incident light in the low power limit (when the recombination time does not depend on the photo-excited quasiparticle density) is given by

$$N_{qp} = \frac{P\tau}{\Delta} \tag{C.1}$$

with P the absorbed power and τ the recombination time. The noise increase reflects the photon shot noise. Analogous to electron shot noise, the relative photon shot noise is given by

$$S_P = \frac{2\hbar\Omega}{P} \tag{C.2}$$

with dimension 1/Hz.

The frequency shift is proportional to the amount of excited quasiparticles, hence: $\Delta f \propto P$. Therefore, the frequency power spectral density is proportional to the noise in the power. As a result,

$$\frac{S_{f_0}}{f_0^2} = \left(\frac{\Delta f}{f_0}\right)^2 S_P \tag{C.3}$$

The frequency noise is converted to the phase noise, using Eq. 3.24: $S_\theta = (4Q_l)^2 S_{f_0}/f_0^2$.

In order to estimate the phase noise level under continuous optical illumination in the experiment described in Chapter 5 the responsivity and absorbed power need to be determined. These are extracted from the resonance frequency shift with temperature of the Ta resonator. The resonance frequency is plotted

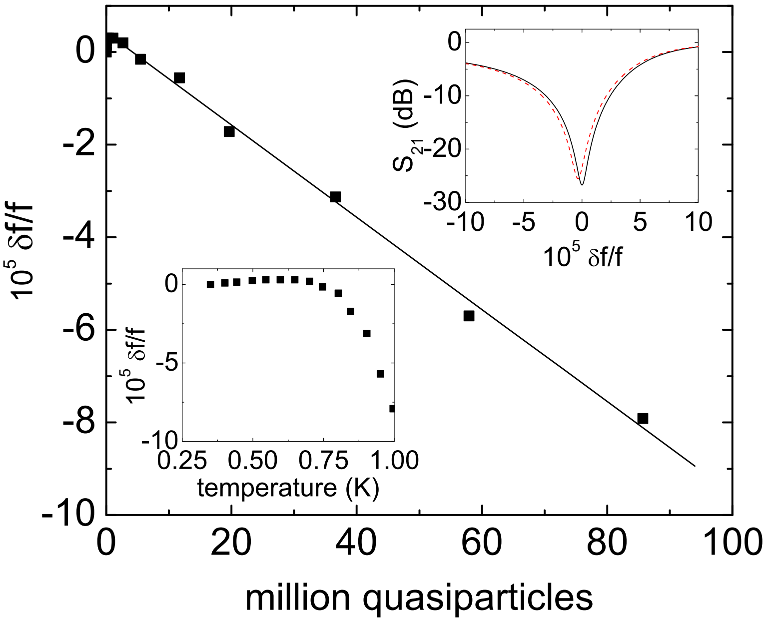

Figure C.1: The main figure shows the decrease of the resonance frequency with increasing number of thermally excited quasiparticles in the central line. The solid line is a fit to the data with $r = 9.7 \cdot 10^{-13}$. The low inset shows the resonance frequency versus bath temperature. The upper inset shows the transmission around resonance in equilibrium conditions (solid line) and under continuous illumination (dashed line). The data are from the same sample used for Fig. 5.2.

(Fig. C.1) versus number of thermally excited quasiparticles in the central line, calculated using Eq. 2.2. A linear fit to the data gives the responsivity of the frequency: $r = \delta\frac{\Delta f}{f_0}/\delta N_{qp} = 9.7 \cdot 10^{-13}$. The absorbed power is given by

$$P = \frac{\Delta}{\tau}\frac{1}{r}\frac{\Delta f}{f_0} \tag{C.4}$$

which gives $P = 17$ pW, using $\tau = 23$ μs and $\Delta = 0.67$ meV for the Ta sample used for Fig. 5.2. Additionally, due to the illumination the frequency shifts with $\Delta f = 17.3$ kHz. The resonance frequency is $f_0 = 4.96$ GHz.

With the absorbed power at $P = 17$ pW, $\hbar\Omega$=1.9 eV (bandgap of the GaAsP LED), $S_P = 3.6 \cdot 10^{-8}$ 1/Hz $= -74$ dBc/Hz. Consequently, $S_{f_0}/f_0^2 = -184$ dBc/Hz. With $Q_l = 7850$, $S_\theta = -94$ dBc/Hz. This value is very close to the measured phase noise at -96 dBc/Hz, see Fig. 5.2.

This noise level exceeds the quasiparticle generation-recombination noise. From Eq. 2.6 we expect the value of $N\tau = 1.9 \cdot 10^2$ (using $\tau_0 = 42$ ns and $2N^a(0) = 4.3 \cdot 10^{47}$ 1/Jm^3). Hence, Eq. 2.10 gives $S_N = 7.4 \cdot 10^2$ 1/Hz, leading to $S_{f_0}/f_0^2 = r^2 S_N = -210$ dBc/Hz, which is far below the frequency noise arising from the photon shot noise.

Summary

Photon-detecting superconducting resonators

One of the greatest challenges in astronomy is observing the universe in the far-infrared with large imaging arrays (100x100 pixels or more) with a sensitivity so high, that it is limited by the background emanations of the *universe itself*. Superconducting resonators are ideally suited for this task. In superconductors, the electrons are paired with a binding energy small enough for far-infrared photons to create unpaired excitations, or quasiparticles. These devices can be operated at temperatures where less than a *billionth* of the electrons are thermally excited, sensitively probing the photo-excited particles. At the same time, these resonators have quality factors reaching values on the order of a million, and are able to sense tiny variations. By giving each resonator (or pixel) a slightly different length, like the pipes in an organ, many can be read out simultaneously in the frequency domain. This frequency domain multiplexing allows for the construction of large imaging arrays.

Photon detectors work best when relaxation is slow. The steady stream of incoming photons breaks many paired electrons into quasiparticle excitations. The amount of excitations created, and consequently the detector sensitivity, is proportional to the relaxation time. The relaxation occurs by the pairing, or recombination, of these quasiparticle excitations into the paired particles, which bring about the characteristic superconducting properties such as the complex conductivity and, by extension, the kinetic inductance. As the detection mechanism essentially relies on counting paired electrons and unpaired excitations, particle number fluctuations are a fundamental noise limit. Additionally, possibly present dipoles and magnetic spins can couple to the electric and magnetic fields in the resonator, giving rise to noise.

Interestingly, the drive for sensitive detectors for observing the *universe* boils down to fundamental questions about the *microscopic* processes: “How do electrons interact and exchange energy?”, and “What fluctuates at low temperatures, causing noise?”. These questions lie at the heart of mesoscopic physics. This thesis describes a series of experiments aimed at elucidating the physical mechanisms behind these processes.

We start with our experiments by first measuring the low temperature properties of superconducting resonators. In principle these properties are controlled by the superconductor, but for Nb and Ta, we find that with decreasing temperature the quality factor increases exponentially, yet saturates at low temperatures. Additionally, a clear nonmonotonicity in temperature dependence of the resonance frequency is observed at low temperatures. These observations signal the presence of additional processes influencing resonator properties. Preliminary measurements of the noise indicate a considerable low frequency contribution coming from the resonator itself. Having tested our designs we shift our focus to quasiparticle relaxation.

Using superconducting resonators we, for the first time, directly probe the low temperature quasiparticle recombination processes using the response of the complex conductivity to photon flux. For both Ta and Al we find that at high temperatures the relaxation times increase with decreasing temperature, as expected for recombination with electron-phonon interaction. At low temperatures we find relaxation times as long as a millisecond for Al and several tens of microseconds for Ta. Moreover, we find a clear saturation of the relaxation times at low temperatures in both materials, indicating the presence of an additional recombination channel in the superconducting films. Motivated by reminiscence of the low temperature saturation to experiments in normal metals on inelastic scattering among electrons, we investigate the influence of magnetic impurities on the recombination process. We find that low temperature relaxation is strongly enhanced by the implantation of magnetic as well as nonmagnetic atoms, while the relaxation at high temperatures is only weakly affected. This indicates that the enhancement of low temperature recombination arises from an enhancement of disorder.

In the remaining part we turn to the subject of excess frequency noise and deviations in the temperature dependence of the resonance frequency, which have been widely observed at low temperatures. We have found that NbTiN, on hydrogen passivated Si, does not show a nonmonotonic temperature dependence of the resonance frequency. We show that this temperature dependence is reestablished by covering the samples with sputtered thin SiO_x layers, and that these deviations scale with the thickness. In addition, we find that the frequency noise is strongly increased as soon as a SiO_x layer is present; but is, in contrast, independent of the layer thickness. This indicates that the noise is dominantly due to processes occurring at interfaces, whereas deviations in the temperature dependence arise from processes in the volume of the dielectric. Finally, we find that we can significantly decrease the noise by widening the geometry of the resonator waveguide, and that the noise is lowest when using hydrogen passivated Si instead of sapphire as substrate.

Rami Barends
Delft, April 2009

Samenvatting

Foton-detecterende supergeleidende resonatoren

Een van de grootste uitdagingen in de astronomie is het waarnemen van het universum in het ver-infrarood met een grote camera (meer dan 100x100 beeldpunten) die een gevoeligheid heeft die zo hoog is dat de achtergrondstraling van het *universum zelf* de limiterende factor is. Supergeleidende resonatoren zijn uitermate geschikt voor deze taak. In supergeleiders zijn de elektronen gepaard met een bindingsenergie die zó klein is dat ver-infrarood fotonen paren kunnen opbreken en ongepaarde excitaties kunnen creëren, zogenaamde quasideeltjes. Deze resonatoren worden gebruikt op temperaturen waar minder dan een miljardste van de elektronen thermisch geëxciteerd zijn, derhalve kunnen deeltjes die door fotonen zijn geëxciteerd gevoelig opgemerkt worden. Anderszijds kan de kwaliteitsfactor van deze resonatoren oplopen tot wel een miljoen; hierdoor kunnen hele kleine veranderingen gevoeld worden. Door iedere resonator (of beeldpunt) een iets andere lengte te geven, net zoals bij orgelpijpen, kunnen velen tegelijkertijd uitgelezen worden in het frequentiedomein. Dit multiplexen in het frequentiedomein staat de bouw van grote camera's toe.

Fotondetectoren werken het beste wanneer relaxatie langzaam plaatsvindt. De stroom aan inkomende fotonen creëert vele ongepaarde excitaties. De hoeveelheid excitaties, en daarmee de gevoeligheid van de detector, is evenreding met de relaxatietijd. Relaxatie vindt plaats door het paren, oftewel de recombinatie, van ongepaarde quasideeltjes tot gepaarde elektronen, deze brengen de karakteristieke eigenschappen van supergeleiders voort zoals de complexe geleiding en daarmee de kinetische zelfinductie.

Interessant genoeg komt de ontwikkeling van gevoelige detectoren om het *universum* waar te nemen neer op het beantwoorden van fundamentele vragen over *microscopische* processen: “Hoe vindt de interactie tussen elektronen plaats en wordt energie uitgewisseld?”, en “Wat fluctueert op lage temperaturen en genereert ruis?”. Deze vragen liggen aan de basis van de mesoscopische fysica. Dit proefschrift beschrijft een set van experimenten opgezet om de fysische mechanismen achter deze processen te ontrafelen.

We beginnen met de experimenten door de eigenschappen van supergeleidende resonatoren op lage temperaturen te meten. In principe worden deze voortgebracht door de supergeleider, maar voor de materialen Nb en Ta zien we dat met lager wordende temperatuur de kwaliteitsfactor eerst exponentieel toeneemt en dan gek genoeg satureert op lage tempeturen. Ook is er duidelijk een niet-monotone temperatuur afhankelijkheid te zien in de resonantiefrequentie op lage temperaturen. Deze waarnemingen geven aan dat er meerdere processen zijn die de eigenschappen van resonatoren beïnvloeden. Eerste ruismetingen laten ook zien dat een behoorlijke hoeveelheid ruis uit de resonatoren zelf komt. Nu we het ontwerp van de resonatoren getest hebben concentreren we ons op de relaxatie van quasideeltjes.

Met supergeleidende resonatoren observeren we, voor het eerst, direct de recombinatie van quasideeltjes op lage temperaturen door gebruik te maken van de respons van de complexe geleiding op een fotonenstroom. Voor Ta en Al vinden we dat op hoge temperaturen de relaxatietijden omhoog gaan wanneer de temperatuur verlaagd wordt, zoals verwacht voor recombinatie met overdracht van de energie naar het kristalrooster. Op lage temperaturen vinden we relaxatietijden van bijna een milliseconde voor Al en tientallen microseconden voor Ta. Eveneens vinden we een duidelijke saturatie van de relaxatietijden op lage temperaturen in beide materialen, dit duidt op de aanwezigheid van een tweede recombinatieproces in de supergeleidende films. Deze saturatie doet denken aan experimenten aan inelastische interactietijden in normale metalen. Met dit in het achterhoofd, onderzoeken we de invloeden van magnetische verontreinigingen op het recombinatieproces. We vinden dat op lage temperaturen de relaxatie flink sterker is geworden door de implantatie van magnetische alsook niet-magnetische atomen. Dit terwijl de relaxatie op hogere temperaturen nauwelijks beïnvloed wordt. Deze resultaten geven aan dat een versterking van het recombinatieproces op lage temperaturen veroorzaakt wordt door een versterking van wanorde.

Vervolgens richten we ons op de behoorlijke hoeveelheid frequentieruis en de afwijkingen in de temperatuurafhankelijkheid van de resonantiefrequentie, deze zijn op grote schaal gesignaleerd op lage temperaturen. We vinden dat NbTiN op Si, dat gepassiveerd is met waterstof, geen niet-monotone temperatuurafhankelijkheid van de resonantiefrequentie vertoont. We laten zien dat deze temperatuurafhankelijkheid terugkomt als we de resonatoren bedekken met een dunne diëlektrische laag SiO_x, en dat deze afwijkingen schalen met de dikte van de laag. Daarentegen springt de frequentieruis omhoog zodra een SiO_x laag aanwezig is, maar stijgt niet verder met dikkere lagen. Dit laat zien dat de ruis voornamelijk komt door processen aan oppervlakken, terwijl afwijkingen in de temperatuurafhankelijkheid van de resonantiefrequentie voortkomen uit processen in het volume van de diëlektrische laag. Tenslotte vinden we dat we de ruis significant kunnen verminderen door een bredere geometrie voor de transmissielijn van de resonator te kiezen en dat de ruis het laagst is wanneer met waterstof gepassiveerd Si wordt gebruikt als substraat.

Rami Barends
Delft, april 2009

Curriculum Vitae

Rami Barends

6 May 1981	Born in Delft, The Netherlands.
1993-1999	Grammar school Grotius College, Delft
1999-2004	M. Sc. in Applied Physics (*cum laude*) Delft University of Technology Graduate research in the group of prof. dr. ir. T. M. Klapwijk Subject: *Analysing Superconducting THz Detectors: Non-equilibrium Double Barrier Junctions and Hot Electron Bolometer Mixers* Received scholarship "Sterbeurs" for highly promising first year students (1999) Received "Study Prize Applied Physics" for outstanding graduation research (2004)
2004-2009	Ph. D. research at Delft University of Technology Subject: *Photon-detecting superconducting resonators* Promotor: Prof. dr. ir. T. M. Klapwijk Copromotor: Dr. J. R. Gao

List of publications

1. R. Barends, H. L. Hortensius, T. Zijlstra, J. J. A. Baselmans, S. J. C. Yates, J. R. Gao, and T. M. Klapwijk
   Noise in NbTiN, Al and Ta superconducting resonators on silicon and sapphire substrates
   accepted for publication in IEEE Transactions on Applied Superconductivity (2009).

2. R. Barends, S. van Vliet, J. J. A. Baselmans, S. J. C. Yates, J. R. Gao, and T. M. Klapwijk
   Quasiparticle relaxation in high Q superconducting resonators
   Journal of Physics: Conference Series **150**, 052016 (2009).

3. R. Barends, S. van Vliet, J. J. A. Baselmans, S. J. C. Yates, J. R. Gao, and T. M. Klapwijk
   Enhancement of quasiparticle recombination in Ta and Al superconductors by implantation of magnetic and nonmagnetic atoms
   Physical Review B **79**, 020509(R) (2009).

4. R. Barends, J. J. A. Baselmans, S. J. C. Yates, J. R. Gao, J. N. Hovenier, and T. M. Klapwijk
   Quasiparticle relaxation in optically excited high-Q superconducting resonators
   Physical Review Letters **100**, 257002 (2008).

5. R. Barends, H. L. Hortensius, T. Zijlstra, J. J. A. Baselmans, S. J. C. Yates, J. R. Gao, and T. M. Klapwijk
   Contribution of dielectrics to frequency and noise of NbTiN superconducting resonators
   Applied Physics Letters **92**, 223502 (2008).

6. R. Barends, J. J. A. Baselmans, S. J. C. Yates, J. N. Hovenier, J. R. Gao, and T. M. Klapwijk
   Quasiparticle lifetime and noise in tantalum high Q resonators for kinetic inductance detectors
   Journal of Low Temperature Physics **151**, 518 (2008).

7. J. J. A. Baselmans, S. J. C. Yates, R. Barends, J. J. Lankwarden, J. R. Gao, H. Hoevers, and T. M. Klapwijk
   Noise and sensitivity of aluminum kinetic inductance detectors for sub-mm astronomy
   Journal of Low Temperature Physics **151**, 524 (2008).

8. J. J. A. Baselmans, S. J. C. Yates, P. de Korte, H. F. C. Hoevers, R. Barends, J. N. Hovenier, J. R. Gao, and T. M. Klapwijk
   Development of high-Q superconducting resonators for use as kinetic inductance detectors
   Advances in Space Research **40**, 708 (2007).

9. J. R. Gao, M. Hajenius, Z. Q. Yang, J. J. A. Baselmans, P. Khosropanah, R. Barends, and T. M. Klapwijk
   Terahertz Superconducting Hot Electron Bolometer Heterodyne Receivers
   IEEE Transactions on Applied Superconductivity **17**, 252 (2007).

10. R. Barends, J. J. A. Baselmans, J. N. Hovenier, J. R. Gao, S. J. C. Yates, T. M. Klapwijk, and H. F. C. Hoevers
    Niobium and tantalum high Q resonators for photon detectors
    IEEE Transactions on Applied Superconductivity **17**, 263 (2007).

11. D. Loudkov, R. Barends, M. Hajenius, J. R. Gao, and T. M. Klapwijk
    Resistivity of Ultrathin Superconducting NbN Films for Bolometer Mixers
    IEEE Transactions on Applied Superconductivity **17**, 387 (2007).

12. R. Barends, J. N. Hovenier, J. R. Gao, T. M. Klapwijk, J. J. A. Baselmans, S. J. C. Yates, Y. J. Y. Lankwarden, and H. F. C. Hoevers
    Quasiparticle lifetime in tantalum kinetic inductance detectors
    Proceedings of the 18th International Symposium on Space Terahertz Technology, Caltech, Pasadena, USA, p. 180, 21-23 March 2007.

13. J. J. A. Baselmans, R. Barends, J. N. Hovenier, J. R. Gao, H. F. C. Hoevers, and T. M. Klapwijk
    Development of high-Q superconducting resonators for use as kinetic inductance sensing elements
    Nuclear Instruments and Methods in Physics Research Section A **559**, 567 (2006).

14. R. Barends, M. Hajenius, J. R. Gao, and T. M. Klapwijk
    Current-induced vortex unbinding in bolometer mixers
    Applied Physics Letters **87**, 263506 (2005).

15. M. Hajenius, R. Barends, J. R. Gao, T. M. Klapwijk, J. J. A. Baselmans, A. Baryshev, B. Voronov, and G. Gol'tsman
    Local resistivity and the current-voltage characteristics of hot electron bolometer

mixers
IEEE Transactions on Applied Superconductivity **15**, 495 (2005).

16. R. Barends, M. Hajenius, J. R. Gao and T. M. Klapwijk
Direct correspondence between HEB current-voltage characteristics and the current-dependent resistive transition, Proceedings of the 16th International Symposium on Space Terahertz Technology, Göteborg, Sweden, p. 416, 2-4 May 2005.

17. T. M. Klapwijk, R. Barends, J. R. Gao, M. Hajenius, and J. J. A. Baselmans
Improved superconducting hot-electron bolometer devices for the THz range
Proceedings of the Society of Photo-optical Instrumentation Engineers (SPIE) **5498**, 129 (2004).

18. R. Barends, J. R. Gao and T. M. Klapwijk
Hot Electron Superconducting Detector using a Double Barrier Junction
Proceedings of the 6th International Workshop on Low Temperature Electronics (WOLTE-6), ESTEC Noordwijk, p. 25, 23-25 June 2004.

The thought had crossed my mind

“The thought had crossed my mind” was the cryptic answer Teun got when he asked me whether I already thought of doing a PhD in his group. At the time I was halfway through the final year, yet nearly finished with the subject of nonequilibrium double barrier junctions; I was however not convinced my master’s, guided by Gao, was complete. Therefore we turned to hot electron bolometers for the remainder, which resulted in a publication in Applied Physics Letters later on. My master’s awoke the appetite for understanding physical processes, for identifying their role in measurable quantities and for contributing to the beautiful symbiosis between physics occurring at the nanoscale and astronomical instrumentation for observing the universe.

After my internship in Cologne, where I was introduced to high frequency measurements, I was ready to take on a new challenge with photon-detecting superconducting resonators, in close collaboration with Jochem in Utrecht. This was not only a highly promising concept, but also a new direction for detection, a new way of probing physics at low temperatures as well as an experimentally challenging subject: at the start there was not a single SMA connector in our lab. The ramifications of the thought that crossed my mind culminated in the thesis you now hold in your hands.

Though obtaining a PhD degree is an individual achievement, the path towards it is nonetheless a team effort. Teun, it has been a pleasure to work, a learning experience to write articles, and a privilege to have so many enthusiastic discussions with you. You would always make the time to critically discuss any kind of issue. Your ability to quickly switch topics and address the physics beneath is inspiring. In addition, your ‘Teunisms’ and witty remarks have enriched my vocabulary! Gao, thanks for all the sharp advices, your keenness and all the support you gave, especially at the start. Your way of thinking and testing ideas, whether designs or proposed series of samples, is praiseworthy. Also your company on so many conferences, workshops and visits was very pleasurable. Jochem, the enthusiastic discussions, the help, the critical thinking and the cunning insight have all been so helpful. While we were a city apart, we really work well together, whether on recombination experiments, samples, or quadrature mixers, as if there is no distance. The phoning and mailing on a daily basis evidence that there is a *very* close collaboration; which also became the running joke during the KID workshop. I think we showed that you can do fundamental physics and work towards directly improving the sensitivity of detectors at the same time and that real improvements are obtained when these go hand-in-hand! Steve, you really strengthened the KID team, being thoroughly involved in the discussions and experiments. Thanks also for the occasional lessons in upper-class British English!

Yet experiments cannot be carried out so successfully without the technicians. Niels, thanks for all the help with building the setup and with the experiments. You really taught me a lot about RF, especially about mismatches! In addition to cooling cryostats with liquid nitrogen and helium when needed, you also took care we did not dry up, whether it was with alcohol or tea: you exposed us to all to a whole brave new world of tea, especially the chrysanthemum tea which turned out to be non-vegetarian! Tony, thanks for all the samples you made and for keeping a down-to-earth approach to sample fabrication, your calmness is something to envy! Mascha, you've been a very supportive Bond-girl! Additionally, a big thanks goes out to Aad for doing a lot of machining for the cryostat, to Raymond for lending so many items and to all the guys at the instrumentendienst for helping out with the cryostat wiring.

But wait, the ramifications don't stop here! Merlijn, you've been one of the most interesting people I've met, encouraging me already during my bachelor project all the way to the 'knetterdetetters'. You keep to amaze me, whether it is with food ranging from peanut butter to cryogenic apples, to near-misses in the cleanroom with exploding dragonflies, or hilarious moments like boating trips in Sweden (did you find a decent restaurant after you missed the boat?). About the cleanroom, you should 'hang' you-know-who with the blue headgear on a prominent place! Moreover, we have shared all the ups and downs, the hotspots and cryo-leaks, concluding during one of the many evening dinners that we work with *cry*ostats. And yes, I might feel a little resentment over freezing your hair, but only a tiny bit. Thanks for everything!

Of course, roommates are an intricate part to PhD. Chris, thanks for being my roommate for so long and for all the conference visits we did together. Whether it was the trip to Sweden, getting lost in Seattle, venturing into the desert in California or taking it easy in Chicago, we always turned it into a little holiday. I feel privileged for being your "rock in the burning", whether in our room or during that famous 'Picnic'-moment on the German motorway. Let's keep these good memories, also from Oktoberfest (luckily we've got the pictures)! By the way, are you already developing an appetite for Knoedels? Gabri, thanks for being my roommate, for the lunch-applause and for keeping the focus on “klemmen!”. In the too short time you were with us we really took over each other’s best traits. Akira, apart from becoming my roommate you will also now further ‘father’ the KIDs. Good luck to you, and it is great to see you pick up so quickly.

In addition, I had the honour of supervising many students. Rik, it has been a pleasure to work with you and see you grow. You have become happy with the bonding machine and lots of experimental work and measurements (‘houtje-touwtje-knutsel-avontuurtje’), culminating in you being co-author of a publication. Obviously I didn’t scare you enough as you are now doing a PhD in our group. And now you live with the credo “*see* the data, *feel* the data, *be* the data”! I have confidence that you grow both financially as well as intellectually, so we can rightfully call you “Rikkefeller”. Jeroen, we kept it cool when things were over or under pressure. Simon, you have been a great help. I sometimes forgot it was only a bachelor’s project, yet you really contributed towards a publication! Do you still dream of bonding? Pieter, thanks for all the help and it is great to see you came back for more! Werner, you are becoming more practical everyday, and thanks for the conversations about finance (Middelkoop!).

I would also like to thank the guys at SRON for discussions, samples and nice dinners during conferences: Henk Hoevers, Jan-Joost Lankwarden (thanks for all the fabrication!), Andrey Baryshev, Pourya Khosropanah (“I’ll find me a beggar”, holding a bag with chicken after Gao got more than he bargained for) and Piet de Korte.

I would like to thank Yuli Nazarov, Yaroslav Blanter and Tero Heikkilä for the scientific discussions. In addition, the discussions with the ESTEC group - Richard Hijmering, Peter Verhoeve, Alexander Kozorezov and Alexander Golubov - were really helpful. Pleasurable and constructive interactions during the many visits and conferences were also with the group at Caltech/JPL - Jonas Zmuidzinas, Peter Day, Ben Mazin, Jiansong Gao, Megan Eckart and Shwetank Kumar - as well as with the Cardiff group - Phil Mauskopf and Simon Doyle.

I also want to thank all the others which are or have been part of our group. Nathan, thanks for the social events and many conversations, for helping to redefine the anatomy of man (can you already reach your kikularis?), and for slowly picking up the hard *g*. Gratefully, you are becoming encouragingly more dutchable. Mr. Alibey, thanks for the many hilarious discussions in English (remember: the tree is outside) and the social events, one during which you exclaimed “I went to the shop, but the shop wasn’t there”. I hope your navigational skills (“Alibey, Alibey, Alibey, always the wrong way”) improve over time. Moreover, I had a great time with Tarun (we might still get you that drinking licence!), Saverio (you still owe me the recipe for lasagna in the Nordiko), tovarishch Dennis, Ruurd (how's your stomach?), Frank (roommie!), Alberto (I miss the discussions on Italian politics), Shaojiang, Yuan, Remco (if all else fails, we could start the 'Pleurop' company!), Matthias, Omid (thanks for existential discussions on bananas), Elfi (any more candy?), Tim, Amar and all the BSc students. Outside of our group, I had an enjoyable interaction with Pol (thanks for the Spanish), Thomas, Anna, Monica, Benoit, Christian, Jeroen, and a special thanks goes to my 'zwarte pieten' Edgar and Menno. Also we had frequent guests: Franzie (cleaning ist spaß!), Kate ("no beer, only vodka"). Moreover, Ari and Pasi from Finland were a great help in the cleanroom during their very fruitful 'holiday' month with us. Do you guys already have a huge yacht, and Ari, do you need some more Delft Blue? And of course a big thanks goes out to the secretaries Maria, Monique and Irma, not only for their assistance but also for keeping the spirits high at the coffee table and for enforcing a tight dish washing schedule.

Most importantly, I would like to thank my parents, brother and sister for their unconditional support.

All this did not cross my mind more than four years ago, but it was a starting point for a great experience. *What a thought.*

Rami Barends
Delft, April 2009